Iowa Research Online
The University of Iowa's Institutional Repository

University of Iowa
Iowa Research Online

Theses and Dissertations

Spring 2015

A numerical study of periciliary liquid depth in MDCT-based human airway models

Dan Wu
University of Iowa

Copyright 2015 Dan Wu

This dissertation is available at Iowa Research Online: http://ir.uiowa.edu/etd/1804

Recommended Citation
Wu, Dan. "A numerical study of periciliary liquid depth in MDCT-based human airway models." PhD (Doctor of Philosophy) thesis, University of Iowa, 2015.
http://ir.uiowa.edu/etd/1804.

Follow this and additional works at: http://ir.uiowa.edu/etd


Part of the Mechanical Engineering Commons

A NUMERICAL STUDY OF PERICILIARY LIQUID DEPTH IN MDCT-BASED HUMAN AIRWAY MODELS

by

Dan Wu

A thesis submitted in partial fulfillment
of the requirements for the Doctor of
Philosophy degree in Mechanical Engineering
in the Graduate College of
The University of Iowa

May 2015

Thesis Supervisor: Professor Ching-Long Lin

Graduate College
The University of Iowa
Iowa City, Iowa

CERTIFICATE OF APPROVAL

_____

PH.D. THESIS

_____

This is to certify that the Ph.D. thesis of

Dan Wu

has been approved by the Examining Committee
for the thesis requirement for the Doctor of Philosophy
degree in Mechanical Engineering at the May 2015 graduation.

Thesis Committee: _____
Ching-Long Lin, Thesis Supervisor

_____
Jia Lu

_____
James H.J. Buchholz

_____
Eric A. Hoffman

_____
Merryn H. Tawhai

_____
David A. Stoltz

To my family

ACKNOWLEDGMENTS

I would like to express my deepest gratitude to my advisor, Professor Ching-Long Lin, who I could not respect more for his knowledge, experience, and dedication for scientific research. I am extremely grateful for his patience and support throughout the up-and-downs of my Ph. D. research, and for his time, inspirational advice and critique, which stimulates my potential and makes me a competent researcher. I could not imagine completing this work without his guidance and persistent help. I would also like to thank my committee members for their time and help, Professors Merryn H. Tawhai, Eric A. Hoffman, David A. Stoltz, Jia Lu and James H.J. Buchholz. Especially to Prof. Tawhai, many of my work were inspired by her research and to Prof. Hoffman for revising my papers.

I would like to acknowledge the help and constructive discussion from Dr. Jiwoong Choi, Dr. Shinjiro Miyawaki, Dr. Sanghun Choi, Dr. Youbing Yin and Maged Awadalla. Another thank-you goes to my Lab fellows.

I am grateful to have my husband Yuwei to accompany me, who makes me smile every day. I am indebted to my parents for their love and support for everything I do.

This research was supported in part by NIH grants R01-HL094315, U01-HL114494 and S10-RR022421. I also thank the Texas Advanced Computing Center, San Diego Supercomputer Center, and the XSEDE sponsored by National Science Foundation for the computational resource and time.

ABSTRACT

Periciliary liquid (PCL) is a critical component of the respiratory system for maintaining mucus clearance. As PCL homeostasis is affected by evaporation and mechanical forces, which are in turn affected by various breathing conditions, lung morphology and ventilation distribution, the complex process of PCL depth regulation *in vivo* is not fully understood. We propose an integrative approach to couple a thermo-fluid computational fluid dynamics (CFD) model with an epithelial cell model to study the dynamics of PCL depth using subject-specific human airway models based on multi-detector row computed-tomography (MDCT) volumetric lung images.

The thermo-fluid CFD model solves three-dimensional (3D) incompressible Navier-Stokes and transport equations for temperature and water vapor concentration with a realistic energy flux based boundary condition imposed at airway wall. A corresponding one-dimensional (1D) thermo-fluid CFD model is also developed to provide necessary information to the 3D model. Both 1D and 3D models are validated with experimental measurements, and the temperature and humidity distributions in the airways are investigated. Correlations for the dimensionless parameters of Nusselt number and Sherwood number are proposed for characterizing heat and mass transfer in the airways. As one of the key applications of the thermo-fluid CFD model, the water loss rates in the both 1D and 3D airway models are studied. It is found that the secondary flows formed at the bifurcations elevate the regional heat and mass transfer during inspiration and hence the water loss rate, which can only be observed in the 3D models. Among the three human airway models studied in both 1D and 3D, little inter-subject variability is observed for the distributions of temperature and humidity. However, the inter-subject variability could be dramatic for the distribution of water loss rate, as it is greatly affected by airway diameter and regional ventilation.

A method is proposed to construct an ion-channel conductance model for both normal and cystic fibrosis (CF) epithelial cells, which couples an existing fluid secretion model with an existing nucleotide and nucleoside metabolism model (collectively named epithelial cell model). The epithelial cell models for both normal and CF are capable of predicting PCL depth based on mechanical stresses and evaporation, and are validated with a wide range of experimental data.

With these two models separately validated and tested, the integrated model of the thermo-fluid CFD model and epithelial cell model is applied to MDCT-based human airway models of three CF subjects and three normal subjects to study and compare PCL depth regulation under regular breathing conditions. It is found that evaporative water loss is the dominant factor in PCL homeostasis. Between three types of mechanical forces, cyclic shear stress is the primary factor that triggers ATP release and increases PCL depth. In addition, it is found that that greater diameters of the airways in the 4^{th}-7^{th} generations in CF subjects decrease evaporative water loss, resulting in similar PCL depth as normal subjects. Under regular breathing conditions, the average PCL depths of normal and CF is around 6 to 7 μm, with mechanical forces play a greater role in regulating CF PCL depth. Comparing to 7.68 μm normal base level (considered as optimum PCL depth), this average PCL depth is about 8 to 21% lower. This might suggest that mechanical forces alone cannot entirely balance evaporative water loss, and other mechanisms might be involved.

TABLE OF CONTENTS

LIST OF TABLES

Table

LIST OF FIGURES

Figure

CHAPTER 1

INTRODUCTION

1.1 Overview

Airway surface liquid (ASL) is a liquid layer lining above the epithelium in the conducting airway. ASL layer includes two major layers: mucus and periciliary liquid (PCL). The cilia extended from epithelium move back and forth in the PCL layer (see Figure 1.1 (a) and (c)). The mucus clearance involves trapping foreign particles and bacteria in the mucus and propelling them to the glottis through cilia movement, constituting the primary innate defense mechanism for human airway (Knowles and Boucher 2002). The PCL serves as lubricate for cilia beating and facilitates mucus transport. Maintaining proper periciliary liquid depth is critical to respiratory health, as severe airway surface dehydration causes cilia collapse on to the epithelial surface, and thus impairs mucus clearance (see Figure 1.1 (b) and (d)) (Button et al. 2012). The resulting mucus build-up is prone to cause infection and inflammation. For example, in Cystic Fibrosis (CF) patients, who have a genetic disorder with a dysfunction of Cystic fibrosis transmembrane conductance regulator (CFTR), fail to maintain proper PCL depth and suffer from frequent infections and inflammations (R. C Boucher 2002). Although many research have been conducted to study PCL depth regulation of epithelial cells *in vitro* for normal (NL) and CF (Button, Picher, and Boucher 2007; Button et al. 2013; Tarran et al. 2006; Tarran et al. 2005). However, PCL depth for cells *in vivo* are affected by evaporation, mechanical forces, which are in turn affected by various breathing condition, lung morphology and ventilation distribution, with all these factors interact together, the effect of which is difficult to directly observe or measure, if not possible.

In this research, we propose an integrative approach that combines a thermo-fluid computational fluid dynamic (CFD) solver and an epithelial cell model with employment of human airway geometric model generated from multi-detector row computed-

tomography (MDCT) image. The thermo-fluid model is able to accurately predict evaporation and mechanical forces from the airflow, while the epithelial cell model is able accurately predict the PCL depth based on these two inputs. The coupling of the two models provides the most realistic way to quantify PCL depth regulation in human airway, and assess the effect of each factor. It might help to understand the physiology and pathology involving the thermodynamic in human airway and PCL depth regulation, such as exercise-induced asthma and cystic fibrosis.

Thus, in this study, a thermodynamic model is developed to couple with a CFD solver. As a key application of thermo-fluid CFD model, the water loss from the evaporation is studied. An ion-channel conductance model is developed to connect previously developed fluid secretion model and nucleotide and nucleoside metabolism model (ATP model), with the capability of predicting PCL depth based on mechanical forces and evaporation. With both models validated with experimental data, they are integrated and applied to study PCL depth regulation in three MDCT-based normal subjects and three MDCT-based CF subjects. The roles of mechanical forces and evaporation in PCL depth regulation are assessed and compared between normal and CF subjects.

1.2 Literature Review of Thermodynamic Models

Thermodynamics is one of the fundamental processes in pulmonary physiology. The basic process has long been understood at the macroscopic level. During inspiration, air is heated and humidified by the airway wall until it reaches body core temperature and 100% relative humidity (RH). The location where air reaches this condition is called the isothermic saturation boundary (ISB). During expiration, the process reverses so that the exhaled saturated air cools and loses water. This partly compensates for the heat and water loss from the airway surface liquid (ASL) during inspiration. The bulk of normal air conditioning occurs in the nasal airway, but it also involves intrathoracic airways: the ISB

has been reported to sit around 5 cm distal to the carina during resting breathing (MacIntyre 2011), and during hyperventilation the ISB can move much further distally along the airway tree (McFadden et al. 1985; Martonen, Rosati, and Isaacs 2013). At the microscopic level the heat and humidity can impact on the ciliated epithelial cells that line the airway wall (for example through evaporation of the ASL and entanglement of cilia within mucus) or can cause airway smooth muscle contraction via changes in the extracellular osmolarity of the epithelium (Weiler et al. 2010).

Computational models for temperature and water vapor concentration have previously been developed to study thermodynamic characteristics in the human lungs. One-dimensional (1D) and two-dimensional (2D) models are the most popular methods due to their simplicity and efficiency, where temperature and water vapor concentration are obtained by solving 1D or 2D scalar transport equations (Daviskas, Gonda, and Anderson 1990; Ferron, Haider, and Kreyling 1988; Tawhai and Hunter 2004; Warren, Crampin, and Tawhai 2010) or by solving energy balance equations based on control volume analysis (Hanna and Scherer 1986; Ingenito et al. 1986; Tsu et al. 1988). In general, temperature distributions along the airway axial direction that are predicted by 1D and 2D models agree with measurement data. However, assumptions and simplifications must be made to reduce three-dimensional (3D) governing equations and airway geometric models to 1D or 2D. The difference between 1D and 2D models is that 1D models assume radial profiles of scalars, while 2D models solve them. Because both models assume axisymmetric radial profiles of scalars, they cannot capture local variations of temperature and water vapor concentration whose local gradients are important in predicting local energy flux and water loss. Although 3D models are computationally more demanding than 1D and 2D models, they provide detailed distributions of velocities, temperature and water vapor concentration. For example, with a 3D RANS $k-\varepsilon$ model, Zhang and Kleinstreuer (2003) showed asymmetric and skewed distributions of temperature and "Jet Propellant 8 fuel" vapor concentration in an idealized symmetric cylinder-based airway model.

For simulation of temperature and water vapor concentration in the human airways, an appropriate model for the wall boundary condition is crucial. The simplest approach is to assume that the airway wall remains at constant body temperature (e.g. Zhang and Kleinstreuer (2003)), however this cannot represent the airway wall cooling that occurs during inspiration due to evaporation and heat transfer, nor reheating of the airway wall and condensation that occurs during expiration (Daviskas, Gonda, and Anderson 1990; McFadden et al. 1985; Martonen, Rosati, and Isaacs 2013). To represent the temperature change from the mouth to the deep lung, some studies have prescribed the airway wall temperature (Daviskas, Gonda, and Anderson 1990; Ferron, Haider, and Kreyling 1988; Zhang and Kleinstreuer 2003) (or the outermost tissue layer temperature if tissue layers are considered (Hanna and Scherer 1986; Ingenito et al. 1986; Tsu et al. 1988)), as a function of distance from the mouth. However, these distance-based models cannot predict temperature and humidity under different breathing conditions. Tawhai and Hunter (2004) and Warren, Crampin, and Tawhai (2010) used a physics-based approach to solve heat conduction equations through the airway wall while enforcing an energy balance at the interface between the lumen and the ASL, such that the interface temperature was determined by local energy flux (the rate of energy transfer per area). This approach allowed for a prediction of dynamic changes to the airway wall temperature during breathing, but was limited to a 1D model. The physics-based approach has not yet been used within a 3D thermo-fluid dynamics system.

Airway geometric models also influence local flow and thermodynamic variables, such as velocities, temperature and water vapor concentration. The importance and advantage of using subject-specific geometry and boundary conditions in simulation of pulmonary air flow have been discussed extensively in previous studies (Lin et al. 2009; Lin, Tawhai, and Hoffman 2013; Lin et al. 2007; Yin et al. 2010), however the impact of 3D airway geometry on airway thermodynamics has not yet been studied.

The dimensionless Nusselt (Nu) and Sherwood (Sh) numbers provide one means of characterizing the bulk heat and mass transfer in the human airways. For example, based on estimates from the first four generations of an idealized airway model, Zhang and Kleinstreuer (2003) proposed that $Nu = 0.66(RePr)^{0.5}$, and $Sh = 1.727(ReSc)^{0.328}, Sc \approx 3$, where Pr is the Prandtl number and Sc is the Schmidt number of air. Improving the correlations of these parameters would allow better characterization of bulk heat and mass fluxes under various breathing conditions, for better design of physical and numerical experiments in studies of lung physiology and pathophysiology.

1.3 Literature Review of Water Loss Prediction

The major cause of water loss from the airway surface liquid (ASL) that lines the respiratory airways is evaporation into the inspired air. Although some water is recovered via condensation during expiration, there is a net water loss, the rate of which depends on the inhaled air temperature, humidity and minute ventilation. Dehydration of the ASL can cause dysfunction of the mucociliary transport system. This dysfunction is apparent in cystic fibrosis (Richard C Boucher 2007). Dehydration of the ASL is also implicated in exercise-induced bronchoconstriction (Weiler et al. 2010). Although the total lung water loss is well established (Daviskas, Gonda, and Anderson 1991; Freund and Young 1995; Hasan 2010; Tabka, Jebria, and Guénard 1987), the water loss rate at the bronchial segment level is not well studied. Thus, an evaluation of subject-specific regional water loss is of interest to determine whether there may be geometry-based regional vulnerability to dehydration. Such an investigation requires evaluating the roles of key variables on the dehydration of the airways, including airway diameter, regional ventilation, minute ventilation, and the inhalation conditions. By coupling a model of airway surface water loss to an epithelial cell model for airway surface liquid regulation (Lin, Tawhai, and Hoffman 2013), such a composite model may provide new insights between airway fluid dynamics and regional cellular functions.

Most recent studies of 3D temperature and humidity in the respiratory tract have focused on an understanding of dynamic growth and deposition of hygroscopic aerosols/droplets (Feng, Kleinstreuer, and Rostami 2015; Kim, Xi, and Si 2013). Only a few previous studies have focused specifically on the airway water loss distribution with respiration. In experimental studies, inhaled and exhaled air humidities at the mouth or nose are measured and the overall water loss under various breathing conditions are calculated (Daviskas, Gonda, and Anderson 1991; Freund and Young 1995; Tabka, Jebria, and Guénard 1987). In numerical simulations, the temperature and humidity in the airways are computed, the instantaneous evaporative fluxes are estimated by Fick's Law (Daviskas, Gonda, and Anderson 1991; Ferron, Haider, and Kreyling 1988; Warren, Crampin, and Tawhai 2010). And then the amounts of water loss are estimated by integrating the evaporative fluxes over time. The key to numerical estimation of evaporative flux is to accurately capture the local water vapor concentration gradients, however previous studies evaluating airway surface water loss have largely been based on one-dimensional (1D) (Daviskas, Gonda, and Anderson 1991; Warren, Crampin, and Tawhai 2010) or two-dimensional (2D) (Ferron, Haider, and Kreyling 1988) models which have several limitations. First, they make simplifying assumptions to reduce a complex 3D flow to 1D or 2D systems. One such assumption is axisymmetric air velocity, temperature, and humidity profiles in the airway radial direction, whereas previous studies have shown non-axisymmetric distributions especially near bifurcations (Wu et al. 2014). Second, 1D and 2D geometric models lack many 3D geometric features, such as variation in cross-sectional area along an airway, curvature, and non-circular cross-sectional profiles. Moreover, most previous studies (Daviskas, Gonda, and Anderson 1991; Ferron, Haider, and Kreyling 1988) have been limited to Weibel's symmetric airway model (Weibel 1963), and do not account for inter-subject variability.

1.4 Literature Review of Epithelial Cell Model

Maintaining PCL depth is critical to airway defense system. Cystic Fibrosis (CF) cells suffer from dysfunction of Cystic fibrosis transmembrane conductance regulator (CFTR), which is not able to maintain regular PCL depth and is extremely vulnerable to infections. A numerical study of PCL depth regulation in an *in vivo* environment is helpful to study pathology of CF.

Besides gland secretions, PCL depth is primarily governed by osmosis through ion channels embedded on the apical membrane. Multiple experiments demonstrate that these channels could be regulated by mechanical forces through Adenosine triphosphate (ATP) release (Button et al. 2013; Button, Picher, and Boucher 2007; Tarran et al. 2005), which can be summarized in the following two points. First, three different types of forces can trigger ATP release: cyclic shear stress, cyclic compressive pressure and cilia strain. Second, three channels respond to the ATP release: Calcium-activated chloride channel (CaCC), Epithelial sodium channel (ENaC) and CFTR. These experiments constitute the frame work of PCL depth regulation by mechanical forces. However, PCL depth homeostasis in an *in vivo* environment, viz. the interactions between epithelia cells, mechanical forces and thermodynamics, cannot be observed easily by experiment, if not impossible.

As a high-fidelity CFD solver can accurately predict mechanical forces and water evaporative fluxes in the human airways, it could be further coupled with a cell model to predict PCL depth. Warren, Crampin, and Tawhai (2010) developed a cell model to predict PCL depth by osmosis. They included the intracellular calcium component to model the activation of CaCC. However, they did not include other pathways that might be involved in PCL depth regulation. Zuo et al. (2008) developed an ATP metabolism model that couples with an ion/water transport model by the sodium and chloride permeability to study the ASL regulation. However, the combined ATP-ion/water transport model was not extensively validated against experimental data (Zuo 2007). Herschlag et al. (2013)

developed a cell model that can predict PCL depth based on mechanical forces, but the model lumped all the interactions into three variables: [ATP], ion concentration, and ASL with limited capability.

We proposed an ion-channel conductance model that couples the previously developed fluid secretion model with an ATP metabolism model to reproduce known steady state cellular responses found in experiments. By further integrating it with a thermo-fluid CFD lung mechanics model, it enables the prediction of PCL depth by accounting for CFD-predicted local evaporative fluxes and cellular responses to CFD-predicted local mechanical forces in a subject-specific manner.

1.5 Literature Review of PCL prediction

As maintaining PCL depth is critical in mucus clearance, a study of PCL regulation under various factors in *in vivo* environments helps better understand the underlying mechanism of PCL homeostasis. In particular, a comparison of PCL regulation under NL conditions with that of CF conditions can provide valuable insights on the regulation mechanism, because CF has a defected CFTR channel that fails to regulate PCL depth. However, this can hardly be achieved by experimental studies, if not possible, as it is hard to replicate the *in vivo* airway environments. Even if it were achieved, it is hard to isolate and study the effects of individual factors or even perform control tests. With numerical studies, it is possible to translate the findings in experiments into a simulated *in vivo* environment to interrogate the response of PCL depth to some selected factors.

Previous studies suggested that besides the evaporative water loss, cyclic shear stress (CSS), cyclic compressive pressure (CCP), or cilia strain (CS) are contributing factors in PCL depth regulation (Button et al. 2013). The evaporative water loss and CSS and CCP at the airway lumen and ASL interface can be accurately predicted by the thermo-fluid CFD model, and the CS in NL and CF are reported in Button et al. (2013). Evaporative flux and (three) mechanical forces are passed on to the epithelia cell model that gives PCL

depth change. The integrated model provides a better picture of PCL depth regulation in both normal and CF patients.

1.6 Objectives

The ultimate goal is to integrate the thermodynamic model with a model of epithelial cell fluid transport (Warren, Crampin, and Tawhai 2010) for the study of periciliary liquid water homeostasis (Lin, Tawhai, and Hoffman 2013). The specific objectives are listed as follows:

1. Developing a thermodynamic model coupled to the existing CFD solver to predict the temperature and humidity distribution (collectively named thermo-fluid CFD model).
    - A 3D thermo-fluid CFD lung model with a realistic wall boundary condition in a subject-specific airway geometric model is developed.
    - The effect of asymmetric flow characteristics and the inter-subject variability of scalar transport are investigated.
    - The dimensionless parameters of *Nu* and *Sh* for the airways up to six generations are computed and their correlations with airway branch diameter and local *Re* are derived.
2. Investigating the water loss in MDCT-based human airway models.
    - Both 1D and 3D models are applied to study the characteristics of regional water loss and water loss rate in response to humidity and temperature distribution patterns in the human airways. We expand these investigations to study the effect of secondary flows, which only exist in 3D. As 1D models are more commonly used than 3D, the comparison of 1D and 3D results helps better understand the limitations in accuracy and validity of 1D models.
    - The inter-subject variability of water loss due to subject-specific airway structure and regional ventilation is examined.

- A correlation between local shear stress and a convective mass transfer coefficient is established to better understand ASL homeostasis.

3. Developing an ion-channel conductance model to connect the existing fluid secretion model and ATP model (collectively named epithelial cell model) to predict the PCL depth based on the evaporation and mechanical forces from thermo-fluid CFD results.
    - An ion-channel conductance model is constructed.
    - The epithelial cell model is extensively tested and validated with a wide range of experimental data.
    - The responses of normal and CF cell models to evaporative flux and mechanical forces are investigated.
4. Integrating the thermo-fluid CFD model with the epithelial cell model to study the PCL depth regulation on three CF and three normal human airway models.
    - The affecting factors of evaporative water loss, CSS and CCP are quantified in three NL and three CF subjects.
    - PCL depths based on various combinations of evaporative water loss and mechanical forces are predicted in both NL and CF to assess the roles of each factor in PCL regulation.
    - Controlled tests are conducted to evaluate the influences of structural differences in PCL regulation, in which a CF subject is simulated as a NL subject, while a NL subject is simulated as a CF subject.

The results from objective 1 and 2 have been published in Wu et al. (2014b) and Wu et al. (2015), respectively.

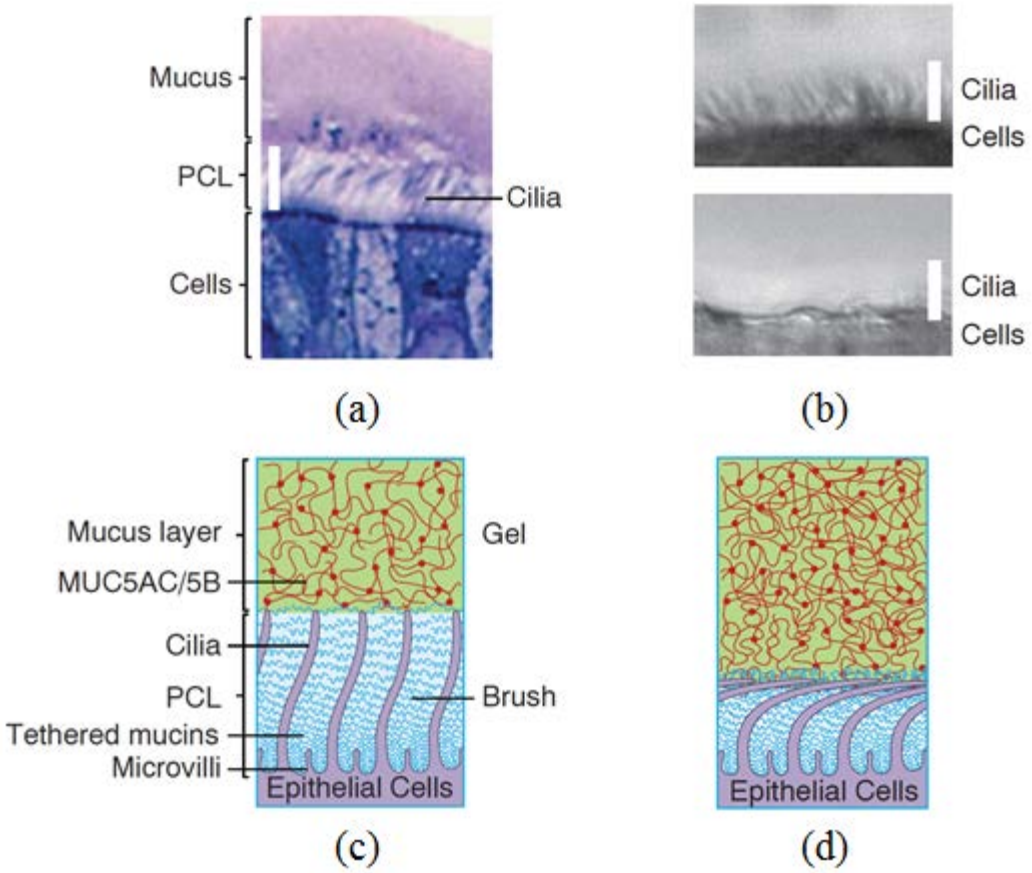

Figure 1.1 (a) The light microscopy view of the airway surface layer. (b) Representative bright-field microscopy images showing the fully extended cilia (upper) vs. the collapsed cilia (lower). The white bar corresponds to the length of fully extended cilia (~7 μm). (c) The schematic view of ASL with mucus layer, PCL layer and fully extended cilia corresponds to a normal state. (d) The schematic view of ASL at a dehydrated state. (Button et al. 2012)

CHAPTER 2

THERMODYNAMIC MODEL

In this chapter, 3D thermodynamic model for human airways are developed. The corresponding 1D thermodynamic model, which is used to provide necessary boundary condition and initial condition to 3D, is also implemented. In the *Result* section, both 1D and 3D models are first validated, and then the temperature and humidity distributions predicted by both models are compared. The dimensionless parameters for heat and mass transfer in human airways are studied.

2.1 Methods

2.1.1 MDCT images and geometry modeling

Geometric models of the airways were reconstructed from volumetric multi-detector row computed-tomography (MDCT) imaging. Three healthy non-smoking subjects (see Table 2.1) that were recruited and imaged under previous studies (NIH grants HL064368 and EB005823) were used here. CT imaging was approved by the University of Iowa Institutional Review Board and Radiation Safety Committee. Subjects gave informed consent for the imaging study and subsequent use of their data for computational studies. Subjects were scanned using a Siemens Sensation 64-slice MDCT scanner (Forchheim, Germany) with scan parameters: 120 kV, 75-100 mAs, 0.75-0.13 mm slice thickness, 0.5-0.6 mm slice spacing, 1.00-1.25 pitch, and B35 reconstruction kernel. Subjects were imaged while supine during a breath-hold at near total lung capacity.

3D geometric models were reconstructed from MDCT using the ‘Apollo’ software (VIDA Diagnostics, Coralville, Iowa); this resolved up to six or seven generations of airways. At the ending segments of the MDCT-resolved central airways, anatomically-consistent 1D trees that extended as far as the terminal bronchioles (about 23 generations) were generated using the volume filling algorithm of Tawhai et al. (2004), subject to the

MDCT-resolved airways and lobar boundaries. For each subject, both 3D geometric models and their corresponding 1D skeletons are shown in Figure 2.1 (a)-(c). The 1D airway models start from the top of the trachea, while the 3D models include the upper airways that start from the oral cavity.

2.1.2 Governing equations

1D models

The radial profiles of temperature $T(r)$, water vapor concentration $C(r)$ and velocity $u(r)$ were modeled using the power-law function of radial coordinate r as in Tawhai and Hunter (2004) as follows:

$$T(r) = T_R + (T_0 - T_R)\left(1 - \left(\frac{r}{R}\right)^{\theta}\right) \tag{2.1}$$

$$C(r) = C_R + (C_0 - C_R)\left(1 - \left(\frac{r}{R}\right)^{\theta}\right) \tag{2.2}$$

$$u(r) = u_0\left(1 - \left(\frac{r}{R}\right)^{\theta}\right) \tag{2.3}$$

where T_0, C_0, and u_0 are the values at the center of the circular lumen, and T_R and C_R are the values at the interface between airway lumen and wall. θ is the parameter used to control the radial profiles, and is assumed as a function of Re only, with $\theta = Re/50$ for $Re > 100$, and $\theta = 2$ for $Re \leq 100$.

For solutions in the axial direction x, the 1D CFD model solved the following 1D transport equations for temperature T and water vapor concentration C.

$$c_P\rho\frac{\partial T}{\partial t} + c_P\rho u\frac{\partial T}{\partial x} = k\left(\frac{1}{r}\frac{\partial}{\partial r}\left(r\frac{\partial T}{\partial r}\right) + \frac{\partial^2 T}{\partial x^2}\right) \tag{2.4}$$

$$\frac{\partial C}{\partial t} + u\frac{\partial C}{\partial x} = D\left(\frac{1}{r}\frac{\partial}{\partial r}\left(r\frac{\partial C}{\partial r}\right) + \frac{\partial^2 C}{\partial x^2}\right) \tag{2.5}$$

Equations (2.1)-(2.3) are substituted into equations (2.4) and (2.5), which are then integrated over the cross-section of the airway to obtain the transport equations of $T_0(x,t)$ and $C_0(x,t)$ (Tawhai and Hunter 2004). Note that T_R and C_R are also unknown variables in

the final form of the equations and they were solved as described in the *Boundary condition* section, prior to solving the transport equations. A finite element method (FEM) was applied to solve equations (2.4) and (2.5). All other parameters are defined in Table 2.3.

3D models

The 3D CFD model solved the incompressible Navier-Stokes equations. Large-eddy simulation was adopted for modeling turbulent flow (Lin et al. 2009; Lin, Tawhai, and Hoffman 2013; Lin et al. 2007; Yin et al. 2010). The continuity and momentum equations read:

$$\frac{\partial u_i}{\partial x_i} = 0 \tag{2.6}$$

$$\frac{\partial u_i}{\partial t} + u_j \frac{\partial u_i}{\partial x_j} = -\frac{1}{\rho}\frac{\partial p}{\partial x_i} + g_i^{'} + (\nu + \nu_T)\frac{\partial^2 u_i}{\partial x_j \partial x_j} \tag{2.7}$$

Here Einstein summation notation is invoked. u_i is the filtered velocity component in the i-direction (i = 1, 2, 3 or x, y, z), p is the pressure, and ν_T is the Vreman's subgrid-scale eddy viscosity (Vreman 2004), which reduces to zero if the flow is laminar. The buoyancy force is computed with Boussinesq approximation of constant density ρ, and $g_i' = -\beta T_v' g_i$, where $g_i = (0,0,-g)$, g is the gravitational acceleration and β is the coefficient of volumetric expansion of air. T_v' is the virtual temperature that dry air must be to have the same density as moist air at the same pressure, $T_v' = T'(1 + 0.61\gamma)$. $T' = T - T_a$, where T_a is the atmospheric temperature. γ is the mixing ratio m_v/m_d, where m_v is the water vapor mass and m_d is the dry air mass. The pressure-Poisson equation that is derived by taking the divergence of Eq. (2.7) was solved to satisfy the continuity of Eq. (2.6).

The transport equations for temperature (T) and water vapor concentration (C) read:

$$C_P \rho \frac{\partial T}{\partial t} + C_P \rho u_i \frac{\partial T}{\partial x_i} = (k + k_T)\frac{\partial^2 T}{\partial x_i \partial x_i} \tag{2.8}$$

$$\frac{\partial C}{\partial t} + u_i \frac{\partial C}{\partial x_i} = (D + D_T)\frac{\partial^2 C}{\partial x_i \partial x_i} \tag{2.9}$$

where C_p is the thermal capacity of moist air and k_T is the turbulent conductivity, $k_T/(C_P\rho) = \nu_T/Pr$. D_T is the turbulent diffusivity of water vapor in air, $D_T = \nu_T/Sc$. Pr_t (Sc_t) is turbulent Prandtl (Schmidt) number of water vapor in air; both Pr_t and Sc_t are taken as 0.9 (Zhang and Kleinstreuer 2003). The characteristic Galerkin finite element method was used to discretize the above equations, and the fractional four step method was used to solve them. The validation of the solver can be found in a previous study (Lin et al. 2005).

2.1.3 Inlet and outlet boundary conditions

An image registration-based subject-specific flow boundary condition (Yin et al. 2010) was adopted. Two MDCT image datasets at different lung volumes from the same scanning session were matched using a mass-preserving image registration method to estimate the ventilation rate at the end of each terminal bronchiole of the 1D tree (Yin et al. 2010). These ventilation rates were then used to derive flow conditions at the distal end of the terminal central airways for 3D CFD simulations. Parabolic profiles for velocity were prescribed at both inlets and outlets. A sinusoidal breathing waveform was used. The maximum flow rate was only a function of minute ventilation (*MV*, L/min) as $\dot{V}_{max} = \pi \times tidal\ volume/t_T = MV\ \times \pi \times 10^{-3}/60$, in which t_T is the breathing period.

For temperature and water vapor concentration, the boundary conditions follow:

$$\begin{cases} \Phi_o = \Phi_I \\ \frac{\partial \Phi_L}{\partial n} = 0 \end{cases} \text{(Inspiration)}; \begin{cases} \frac{\partial \Phi_o}{\partial n} = 0 \\ \Phi_L = \Phi_E \end{cases} \text{(Expiration)} \qquad (2.10)$$

where $\Phi = T\ or\ C$. The subscript *o* denotes the mouth cavity for the 3D model, or the top of the trachea for the 1D model, and *L* denotes the ending faces at the terminal airways in the 3D model or the 1D model. At the flow inlets, the air conditions were prescribed, where the subscript *I* represents inspired *T* or *C* at the mouth entrance for the 3D model, or the top of the trachea for the 1D model. The subscript *E* represents expired *T* or *C* at the ending

faces of the terminal airways in 3D or 1D. Gradient-free conditions were prescribed at the flow outlets.

2.1.4 Airway wall boundary condition

For the momentum equation (2.7), the no-slip condition was imposed at the airway wall. For the *T* transport equation (2.8), energy balance was enforced across the wall boundary so that the energy exchange between the lumen and the ASL equals the heat conducted through the airway wall. For the *C* transport equation (2.9), 100% RH was assumed at the interface of the lumen and the ASL.

To provide the wall boundary conditions for *T* and *C*, a heat conduction equation through the airway wall tissues and the ASL (see Figure 2.1 (e-g)) was solved. Two parameters need to be determined: 1. the thermodynamic properties of the airway wall tissues, and 2. the distance (or thickness) from the airway wall to a location that remains at body temperature during ventilation. Most of the tissues in the airway wall contain a high amount of water and their thermodynamic properties are close to those of water (Hamilton 1998). Thus, a tissue of uniform water properties was assumed, which is the same as the ASL. In order to determine the thickness, the behavior of the 1D heat conduction equation was examined with boundary conditions of fixed temperature on one side and oscillating energy flux on the other side (see Figure 2.1 (f)). We found that after reaching quasi-steady state, only a small portion of the tissue undergoes temperature fluctuations, and the temperature of the other portion of the tissue remains unchanged. Therefore, a two-layer wall model was adopted with one layer capturing the transient response and the other layer representing the steady portion. The heat conduction equation for the two-layer wall model reads:

$$\frac{\partial T_i}{\partial t} = \alpha_i \left[\frac{1}{r}\frac{\partial}{\partial r}\left(r\frac{\partial T_i}{\partial r}\right)\right] \tag{2.11}$$

where the subscript *i*=1 (or 2) denotes the transient layer (or the steady layer). $\alpha_i = k_i/(C_{pi}\rho_i)$ is the thermal diffusivity of layer *i*. For the transient layer, which includes the

ASL, the temperature fluctuation is caused by the oscillating energy flux during respiration. Its thickness is dependent upon the breathing period (estimated at 0.4 mm via the 1D model for 2 s breathing period). For the steady layer, the temperature profile depends on the net energy flux during respiration. The temperature at its interface with the transient layer is denoted as T_m. With known net energy flux, T_m can be determined by the thermal resistance per area. The thermal resistance is given by $R_{resist} = l_2/k_2$, where l_2 and k_2 are the thickness and the thermal conductivity of the steady layer, respectively. Because k_2 appears in Eq. (2.11) as $\alpha_2 = k_2/(C_{p2}\rho_2)$, the parameter $R' = l_2/\alpha_2$ was calibrated using the 1D model against McFadden et al.'s data (McFadden et al. 1985) at 15 and 30 L/min with room air (27.6 ºC, 34.7% RH) and frigid air (-18.5 ºC, 5% RH).

Two boundary conditions are needed to solve Eq. (2.11). At the outer wall of the steady layer, body temperature was prescribed. At the ASL-lumen interface, the energy balance equation was enforced as in Tawhai and Hunter (2004), where the energy flux by conduction at the ASL side of the interface equals the energy flux by conduction plus the latent heat of phase change at the lumen side.

$$k_{asl}\frac{\partial T}{\partial r}|_{R^+} = (k + k_T)\frac{\partial T}{\partial r}|_{R^-} + (D + D_T)\Delta H\frac{\partial C}{\partial r}|_{R^-} \quad (2.12)$$

where k_{asl} is the thermal conductivity of the ASL. k (k_T) is molecular (turbulent) conductivity for moist air. D (D_T) is molecular (turbulent) diffusivity of water vapor in air. R^+ denotes the ASL side of the interface, while R^- denotes the lumen side. The finite element method was used to discretize Eqs. (2.11) and (2.12).

The water vapor concentration at the interface was assumed to be at 100% RH, and the saturated water vapor concentration was solely a function of temperature:

$$C_R = \frac{2.166\times10^{-3}}{T_R}\exp\left(\lambda_1 + \frac{\lambda_2}{T_R} + \lambda_3\, ln(T_R) + \lambda_4 T_R^2\right) \quad (2.13)$$

where $\lambda_1 = 73.649$, $\lambda_2 = -7258.2$, $\lambda_3 = -7.3037$ and $\lambda_4 = 4.165\times10^{-6}$ (Tawhai and Hunter 2004). By solving Eqs.(2.10)-(2.13), the interfacial temperature and water vapor concentration were obtained, providing essential boundary conditions for the

transport equations. Iteration was performed between the conduction equation and the scalar transport equations to yield a converged solution at any time step. Figure 2.2 shows the procedures of performing the 3D CFD thermodynamics simulation in the MDCT-based human airway model.

2.1.5 Simulation set-up and mesh sensitivity test

Three cases for each of three subjects with the room air condition of 27.6 ºC and 34.7% RH (thus a total of nine cases) were simulated (Table 2.2). Minute ventilations for Cases 2 and 3 were chosen so that they could be validated against the measurement data of McFadden et al. (1985) while minute ventilation of Case 1 corresponds to a resting breathing case. For each minute ventilation the breathing period may vary, but this has little influence on the final solution of temperature (Tawhai and Hunter 2004).

Since the airway geometry starts from the top of the trachea in the 1D model, on inspiration T_I (see Eq. (2.10)) is taken from the measurement data of McFadden et al. (1985) and C_I is calculated from Eq. (8) with 95% RH taken from the 3D CFD simulations. For the 3D model, the conditions of 27.6 ºC and 34.7% RH reported in McFadden et al. were used at the mouth inlet. On expiration, at the ending branches of the 1D airway tree, body temperature of 36.5 ºC and 100% RH were used (Tawhai and Hunter 2004). Since the 3D model only has up to six or seven generations and the ISB can be located downstream of these branches, the 1D results on expiration at the corresponding 3D model distal branch locations were specified as time-varying boundary conditions. For the 1D model, the tissue temperature was uniformly initialized to body temperature, and after 200 breaths the tissue temperature reached a quasi-steady state. The 1D quasi-steady state tissue temperature at end expiration was then used as the initial condition for tissue temperature in the 3D model. The 3D upper airway was included to capture the laryngeal jet (Lin et al. 2007), and the wall temperature and humidity of 33.5 ºC and 100% RH were adopted for the airway above the glottis (Tsu et al. 1988).

Tetrahedral meshes were used for 3D CFD simulations (see Table 2.1). First, a mesh sensitivity test was performed on subject A at 15 L/min using three meshes with densities of 21.4, 37.3 and 73.6 $\times 1000/cm^3$, and with average y+ (a non-dimensional distance of the first grid point from the wall) = 5.6, 6.9 and 8.2, respectively, in the trachea at peak inspiration. Energy flux (Eq. (2.12)) was computed for assessment because of its dependence on the wall temperature gradient. As compared with the fine-mesh result, the differences of the overall energy flux integrated over the entire CT-resolved central airway during inspiration (expiration) were 4.17% (9.78%) for the coarse mesh and 2.77% (4.19%) for the medium mesh. The differences by generation for the medium mesh were (3.43, 3.35, 3.03, 3.32, 1.40, 2.16, 0.95) % on inspiration and (1.83, 6.84, 4.85, 3.90, 6.14, 6.27, 6.50) % on expiration for generations (0, 1, 2, 3, 4, 5, 6). The errors are greater at the inlets than the exits for both inspiration and expiration, which may be due to relatively large evaporative flux at generation 6 on inspiration and large condensation flux at generation 0 (trachea) on expiration. Then, the sensitivity test was performed on the same subject at 30 L/min on the medium and fine meshes to quantify the maximum error. The error was 6.44%, as compared with 6.61% for the coarse mesh and 3.16% for the medium mesh at peak inspiration of 15 L/min.

For the ASL and the tissue layer, the 1D mesh was generated at each node on the airway wall along the wall-outward normal direction. As shown in Figure 2.1 (g), the 1D mesh consists of seven nodes: nodes N1 and N2 (with a spacing of 10 μm (Widdicombe 2002)) are for the ASL, nodes N2, N3, N4, N5 and N6 (with a uniform spacing of 0.1 mm) are for the transient tissue layer, and nodes N6 and N7 (with a spacing of 0.1 mm) are for the steady tissue layer. As the ASL is much thinner than the overall transient layer, the change of ASL depth is negligible. The temperature at node N1 is referred to as the interface temperature T_R, and the temperature at N6 is denoted as T_m, while the average lumen temperature is denoted as T_0. Table 2.3 summarizes all of the model parameters.

2.2 Results

2.2.1 Validation of computational models

1D model

The 1D scalar equation was validated through the analytical solutions of pipe flows with constant wall temperature and constant heat flux. For the 1D solver, with the radial profile given as equations (2.1) to (2.3), the average heat transfer coefficient is taken as $\bar{h} = 2(\theta + 1)D_h/k$, where θ = *Re*/50, D_h is the hydraulic diameter. For the constant heat flux case, the analytical solution for the average lumen temperature is $T_0 = T_R - (T_R - T_{in})\exp(-per\bar{h}x/(mc))$, where T_{in} is the entrance temperature, *per* is the perimeter, $\dot{m}$ is the mass flow rate and *c* is the heat capacity. For the constant wall temperature case, the analytical solution is $T_0 = T_R - q^{"}/\bar{h} = T_{R0} + perq^{"}x/(\dot{m}c) - q^{"}/\bar{h}$. Figure 2.3 (a) compares two cases against analytic solutions. The test case was a 10 m long pipe with 0.04 m diameter, and air flow of 2.0 m·s^{-1}. The first case was for constant heat flux (with $q^{"}$ = 28.512 W·m^{-2}, T_{R0} = 31 ºC) and the second case had constant wall temperature (T_R =37 ºC and T_{in} =30 ºC). The comparison between the model and analytic solutions shows good agreement for both cases.

3D model

The 3D scalar equation was validated through the case of a fully developed laminar flow through a round pipe of diameter *d*, with a heat flux $q^{"}$ at the wall boundary. The analytical solution to the temperature of the flow is

$$T = \frac{8q^{"}}{\alpha\rho c_p d}\left[\frac{r^2}{4} - \frac{r^4}{4d^2}\right] + T_R - \frac{3q^{"}d}{8\alpha\rho c_p} \tag{2.14}$$

where ρ is the fluid density, C_p is thermal capacity of the fluid for temperature transport. T_R is the surface temperature with $T_R = T_{R0} + 4q^{"}/(d\rho u_m c)x$, where u_m is the mean velocity and T_{R0} is the wall temperature at the entrance. For fully developed turbulent pipe

flow, the empirical equation has been given by Gnielinski (Nellis and Klein 2009) to estimate the *Nu*, which is a ratio between convective and conductive heat transfer across the pipe wall boundary:

$$Nu = \frac{(\frac{f_{fd}}{8})(Re-1000)Pr}{1+12.7(Pr^{\frac{2}{3}}-1)\sqrt{\frac{f_{fd}}{8}}}, 0.5 < Pr < 2000 \; and \; 2300 < Re < 5 \times 10^6 \qquad (2.15)$$

where f_{fd} is the fully developed friction factor, and $f_{fd} = \frac{1}{[0.79\ln(Re)-1.64]^2}, 3000 < Re < 5 \times 10^6$ for a smooth surface.

For validation of laminar pipe flow, a fully developed flow of moist air (α = 2.06×10^{-5} m^2·s^{-1}, ρ=1.2 kg·m^{-3}, C_p=1080 J·kg^{-1}·K^{-1}) was passed through a pipe that was 100 mm long and 2 mm in diameter, with flow 2.35×10^{-05} m^3·s^{-1}. The *Re* for this case was 880, and the entrance wall temperature was T_{R0}=33 ºC. A constant heat flux of 500 W·m^{-2} was applied at the wall boundary. The radius profiles were extracted at x = 1, 10, 20, 30,..., 90 and 99 mm on the plane passing through the center axis as shown in Figure 2.3 (b). The CFD results match well with the analytical solutions. The flux term calculation was verified by comparing CFD prediction of the flux through the pipe wall $\frac{\partial T}{\partial r}\Big|_R$ with its theoretical value $-\frac{q''}{\alpha\rho c}$. For the validation case, $\frac{\partial T}{\partial r}\Big|_R = -\frac{q''}{\alpha\rho c} = 18{,}728$, and the CFD predicted 19,304, thus the error was 3.0%.

For the turbulent case, air was assumed to pass through a pipe of 1 m long and 0.02 m in diameter with flow 1.57×10^{-3} m^3/s. A constant heat flux of 500 W·m^{-2} was applied at the wall. The *Re* for this case was 5,879. The *Nu* for the fully developed turbulent flow predicted by Equation (2.15) was 20.6. The flow becomes fully developed after about 0.8 m. Taking a cross-section at 0.85 m from the CFD results, the average lumen temperature

$T_0 = \rho/\dot{m} \int_0^R uT \cdot 2\pi r \cdot dr = 237\ K$ and the average surface temperature $T_R = 257\ K$. From the heat flux balance across the boundary, $\bar{h} = q^{"}/(T_s - T_0) = 25.4\ W \cdot m^{-2} \cdot K^{-1}$. Finally, $Nu = hD_h/k = 18.9$. The error of this estimation from the empirical estimation was about 3.4%. Moreover, both the velocity and temperature boundary layer were consistent with the log law of turbulence. Therefore, the 3D solver was validated in both the laminar regime and turbulence regime. The evaporation calculation was also validated through calculating the flux term.

Airway wall boundary model

The 1D airway wall conduction equation was validated with two cases using different boundary conditions. The thermal diffusivity for both cases was 1.43×10^{-07} $m^2 \cdot s^{-1}$, the thermal conductivity was 0.6 $W \cdot m^{-1} \cdot K^{-1}$, and the thickness of the wall was 5 mm. Case 1 used essential boundary condition (EBC) on both sides, with fixed temperature of 37 ºC on one end and 32 ºC on the other. As shown by the solid lines in Figure 2.3 (c), the temperature decreased from the initial temperature of 37 ºC to a linear distribution between two boundaries for the steady state solution. In Case 2 one EBC was replaced by a natural boundary condition (NBC), which is the same boundary condition as in the airway cases. The steady state solution is again a linear function, and the temperature difference between the two sides $\Delta T = q^{"} \cdot (L/k)$. Thus, with $q^{"}$=600 $W \cdot m^{-2}$, the final solution of the NBC side was 32 ºC. As shown by the dashed line in Figure 2.3 (c), the free end decreased to the final solution of 32 ºC, which is consistent with the analytical solution.

2.2.2 Temperature and humidity distributions

The predicted 1D and 3D temperature distributions in the airway were validated against the measurement data of McFadden et al. (1985). In this previous study the authors inserted a probe with seven consecutive sensors, from the nasal cavity through the trachea

and along the path marked by the landmarks in Figure 2.1 (d) into the right lower lobe (RLL). The spacing between sensors was about 4.3 cm, and the first sensor was placed about 2 cm below the glottis. Because the last sensor was placed beyond the most distal airways in two of our 3D models, and the fourth sensor malfunctioned, we compared the 1D and 3D CFD data along the same path using only the data measured from the first five normal sensor locations. Figure 2.4 (a)-(d) display the average values of temperature based on the three subjects. Both 1D and 3D data are generally consistent with the measurement data. A slight discrepancy was found between the most distal measurement point and the 3D data at end expiration for 30 L/min; the model predicted a temperature about 1 degree lower than the experiment. The 1D data shows very little difference between the three subjects before entering the AS (see Figure 2.1 (d)), and the 3D data shows that the difference between these subjects is generally within 0.3 ºC. The average discrepancies between the 1D model and the measurements are 0.28 ºC for 15 L/min and 0.26 ºC for 30 L/min. The average discrepancies between the 3D model and measurements are 0.24 ºC for 15 L/min and 0.27 ºC for 30 L/min. Besides the measurement data of McFadden et al. (1985), Martonen, Rosati, and Isaacs (2013) reported other measurement data that the temperature in the trachea mostly varies between 31.2 and 34.5 ºC during inspiration, and between 32.6 and 37 ºC during expiration, and the temperature after the carina mostly varies between 32.2 and 34. 6 ºC during inspiration, and between 33.7 and 36.0 ºC during expiration. For our 3D CFD data, the temperature in the trachea varies between 31.4 and 34 ºC during inspiration, and 32.8 and 35.0 ºC during expiration, and the temperature after the carina varies between 32.1 and 34.4 ºC during inspiration and between 33.5 and 35.8 ºC during expiration. Thus, our CFD data agree with these measurement data as well.

Figure 2.4 (e)-(h) show the distributions of absolute humidity (water vapor concentration) and relative humidity along the same path as in (a)-(d). As both water vapor concentration and temperature are passive scalars, their distributions and characteristics are quite similar, only differing by the diffusion rate (2.2×10^{-5} for T and 2.7×10^{-5} for C).

However, relative humidity is quite different. During inspiration, the relative humidity is generally above 95% from the glottis, and quickly increases to 100%. The 1D model predicted saturation (100% RH) immediately after the carina, whereas the 3D model predicted that 100% RH was reached slightly beyond the ORL as marked in Figure 2.1 (d), suggesting that unsaturated air penetrates deeper in the 3D airway model. During expiration, the relative humidity remained at ~100% in both 1D and 3D model data. As relative humidity is determined by local temperature, absolute humidity decreased on exhalation due to condensation of water on the ASL. For the same reason, even if both the interface and the lumen air were at 100% RH, evaporation or condensation may continue to occur because of local temperature and absolute humidity differences. Since absolute humidity and temperature exhibit similar distributions, only the temperature data are presented in later sections.

2.2.3 Lumen temperature in 1D trees and 3D central airways

The lumen temperature varies during ventilation. To illustrate this, the spatial distributions of 1D and 3D lumen temperatures of subject A for 15 L/min are shown in Figure 2.4 and Figure 2.6, respectively, at four time points: peak inspiration, end inspiration, peak expiration and end expiration. For the 1D model, the lumen temperature gradually increased until reaching the ISBs, which varied in location during ventilation. The ISB was located at approximately the 8^{th}-9^{th} generation in the upper lobes. As the lower lobes have higher ventilation rates, the ISBs in the lower lobes penetrated as far as the 10^{th}-12^{th} generations on peak inspiration.

For the 3D model, the iso-surfaces of 32 ºC and 32.5 ºC on inspiration and those of 34.5 ºC and 35 ºC on expiration are shown in Figure 2.6. On peak inspiration or expiration, the temperature gradient at the ASL-lumen interface is much greater than that on end inspiration or expiration, since the airway wall has little time to warm or cool the air. The

radial profile of temperature in 3D is not axisymmetric as assumed in 1D. The cold air tends to penetrate further into the lower lobes, particularly on peak inspiration, which may be attributed to the formation of secondary flows after the inspired air passes over the carina. All other cases exhibited similar lumen temperature distributions at the four time points.

2.2.4 Energy transfer at bifurcations

To inspect the features of secondary flows during inspiration, Figure 2.7 (a) shows six streamlines near three bifurcations marked as B_1, B_2 and B_3 in the RLL. The streamline passing over B_1 is warmed by the inner surface of the bifurcation. The air pressing against B_1 then moves downstream toward the center of the lumen, impacts on bifurcations B_2 and B_3, and then flows along the surfaces of the respective daughter branches. Figure 2.7 (b) shows another example with three bifurcations marked as B_4, B_5 and B_6 in the left upper lobe (LUL) with several branches oriented upwards. Similar characteristics as in Figure 2.7 (a) are still observed. In fact, the same flow pattern begins at the carina where the cold high-speed air stream near the lumen center is split at the bifurcation to form secondary flows with its cold regions biased toward the inner wall. The cold air flowing along the wall is being warmed up much faster than the air in the lumen center. Unlike the 1D model that relies solely on diffusion in the radial direction of an axisymmetric profile to warm the central cold air, the repeated splitting and warming of cold air streams acts as an efficient mechanism of enhancing energy transfer in the 3D airway branching structure.

2.2.5 Airway wall boundary model

Figure 2.8 (a) shows the time histories of the 1D ASL-lumen interface temperatures (T_R) at six selected locations along the path defined in Figure 2.1 (d). T_R was initially set at body core temperature. The oscillations correspond to respiratory cycles. The phase-averaged T_R decreases with time until the net energy flux into the lumen is balanced by the energy flux through the tissue, when lumen temperature, energy flux and tissue temperature

all reach quasi-steady states. T_R at a proximal location exhibits greater fluctuations than at a distal location. Figure 2.8 (b) shows the time histories of 1D instantaneous energy fluxes at three selected locations along the same path as before. The net energy flux at quasi-steady state decreases with increasing distance from the top of the trachea, with a net energy loss of 190, 112 and 34 J/m^2 per cycle at x= 4.3, 17.1 and 27.0 cm, respectively. The higher net energy flux (or the net energy loss per cycle) results in lower T_R as shown in Figure 2.8 (a). Figure 2.8 (c) and (d) show that the 1D and 3D average lumen temperatures, T_0, and their corresponding interface temperatures, T_R, oscillate with flow rate during respiration, agreeing with the measurement of Primiano et al. (1988). Figure 2.8 (e) and (f) show that the end inspiration (expiration) T_R is higher (lower) than the corresponding T_0 over the entire airways for both 1D and 3D models. The reverse in magnitude of these two temperatures ($T_R>T_0$ on inspiration vs. $T_R<T_0$ on expiration) is an important feature of air conditioning in the airways.

2.2.6. Dimensionless parameters

The *Nu* is the ratio of convective to diffusive heat transfer, and the *Sh* is its counterpart for mass transfer. Figure 2.9 (a) and (b) show the distributions of local *Nu*, *Sh* and *Re*(*D*/*D*$_t$) along with the proposed correlations: $Nu = 3.504(ReD_a/D_t)^{0.277}, R = 0.841$ and $Sh = 3.652(ReD_a/D_t)^{0.268}, R = 0.825$, during peak inspiration for the three subjects at three levels of minute ventilation. D_a is the local equivalent diameter computed as $D_a = (4A_L/\pi)^{1/2}$, where A_L=local cross-sectional area, D_t is the equivalent diameter of trachea, and $Re = 4flr/\pi\nu D_a$, where *flr* is the local flow rate at peak inspiration. The correlation proposed by Zhang and Kleinstreuer (2003) is also displayed for comparison with $R = 0.641$ for *Nu* and $R = 0.624$ for *Sh.* Figure 2.9 (c) and (e) show that the *Nu* and *Sh* values predicted by the proposed correlations are overall more consistent with the 3D CFD computed values than those predicted by Zhang et al. in Figure 2.9 (d) and (f).

2.3 Discussion

2.3.1 1D vs. 3D

The main objective of this study was to develop a subject-specific 3D model for study of heat and mass transfer in the human airways. The corresponding 1D model was utilized to provide necessary initial and boundary conditions for the 3D model. Mathematically, the 1D model includes convection and diffusion in the axial direction, but it only includes diffusion in the radial direction with assumed radial velocity and scalar profiles. These profiles take the axisymmetric form of $\Phi(r) = \Phi_R + (\Phi_0 - \Phi_R)\left(1 - \left(\frac{r}{R}\right)^{\theta}\right), \Phi = T, C, or\ U$, where θ is empirically determined to fit measurement data. As the average lumen temperature strongly depends on the ASL-lumen interface temperature, with an interface temperature profile that lies between the temperature profiles at end inspiration and end expiration as shown in Figure 2.8 (e) and (f), both 1D and 3D models can reasonably predict scalar transport along the axial direction as shown in Figure 2.4. Nonetheless, the 3D model reveals local non-axisymmetric distributions of temperature and water vapor concentration due to secondary flows in a complex airway geometry, which are essential in accurate estimation of local energy flux and water loss rate. In particular, the 3D model creates relatively large gradients of temperature and water vapor concentration at bifurcations that enhance heat and mass flux. Therefore, as inspired air traverses down the airways it is heated and humidified at a faster rate than is represented by the 1D model, not only because airway surface area increases, but also because the central cold air streams are repeatedly split and effectively warmed up by the surface at the bifurcations. The above 3D mechanism is important in predicting water loss from the epithelial cells in different regions, which contributes to the overall energy loss as latent heat. This cannot be modeled using a standard 1D approach. For example, consider the water loss rate (defined as the net water loss per area per min) in the CT-resolved airways at 15 L/min. For the three 3D cases, the average water loss rates at generation (1, 2, 3, 4,

5, 6) show an increase of (17.7, 25.0, 40.4, 33.4, 39.7, 40.9) % with respect to the rate at the trachea, due to the above mechanism. In contrast, for the three 1D cases the average water loss rates at generation (1, 2, 3, 4, 5, 6) show a decrease of (51.6, 60.0, 66.8, 71.1, 73.4) % with respect to the rate at the trachea. Note that the trachea is still responsible for most of the air conditioning compared with any other generation in both the 1D and 3D models due to its greater surface area, but the thermal input (or the net water loss) into local individual cells are much higher in the 2^{nd} to 6^{th} generations of the 3D model because of secondary flows. Without capturing this 3D phenomenon, the 1D model predicts the opposite trend. Moreover, as shown in Figure 2.6 (a) and (b), the secondary flow at the carina also results in distributing a greater portion of cold air into the lower lobes. As a result, the lower lobes may condition more cold air in the 3D model than the 1D model.

2.3.2 Inter-subject variability

The subject-specific ventilation distribution influences the temperature and humidity distributions. The higher the local ventilation, the more air that needs to be conditioned in a given amount of time. As shown in Figure 2.5 for the 1D results, the ISBs in the lower lobes are located more distally than in the upper lobes because of the higher local ventilation in the lower lobes. The 3D results show similar trends, as the lumen temperature in the upper lobes increases faster than in the lower lobes (see Figure 2.6). However, as all three subjects have relatively large air ventilation to the lower lobes, the inter-subject differences in average temperature and humidity at end inspiration and expiration along the path are only ~0.3 ºC and 1.5 g/m^3. It is worth noting that even though the subject-specific geometry and boundary conditions might not have a significant influence on the bulk temperature and humidity distributions considered here, its importance is reflected in the local gradient terms found in the calculation of heat and mass fluxes. For example, considering the water loss rate of the three 15 L/min cases, the inter-subject variability in each generation (up to the 6^{th} generation) is around 10% to 20% for

the 3D model and 5% to 10% for the 1D model. Thus, the distributions of average temperature and humidity are more sensitive to the interface temperature distribution than other factors, such as the specific mathematical model, ventilation distribution, or airway geometries. However, heat and mass fluxes across the interface are very sensitivity to the local gradients of temperature and humidity, even for regions with only 0.3 ºC of average temperature difference at roughly 100% RH (e.g. 5th generation in RLL): the standard deviation in the water loss rate between the three subjects at 15 L/min is about 15% of the average value.

2.3.3 Dimensionless Correlations

We proposed new correlations for *Nu* and *Sh* with $Re(D_a/D_t)$, allowing estimation of bulk heat and humidity by airway generation under various breathing conditions. These correlations may be useful for understanding the role of heat and humidity in airway pathophysiology (e.g. as a trigger of asthmatic bronchoconstriction) and potentially for improving design of medical devices (e.g. humidification in mechanical ventilation). As compared with Zhang et al.'s study (Zhang and Kleinstreuer 2003), the proposed correlations were fitted to data from airways up to the 6th generation in three different subjects for three different flow rates, while Zhang et al.'s correlation was based on an idealized cylinder-based geometry with data points from the trachea to the 3rd generation. As subject-specific geometries and breathing conditions are used, the proposed correlations take into consideration the effects of both *Re* and local airway diameter, indicating that local flow rate is most likely to determine the *Nu* and *Sh* in the airways. Thus, this supports the importance of using subject-specific ventilation distribution. This also implies that if the local flow rate remains constant during airway constriction, both convective and diffusive heat and mass transfer may increase at constricted areas. Alternatively, if the local flow rate drops due to constriction, the *Nu* and *Sh* would decrease, resulting in more diffusive heat and mass transfer. When applying these correlations to asthmatics (Venegas

et al. 2005), the *Nu* and *Sh* could increase (decrease) in association with expanded (constricted) branches and altered ventilation, altering local heat and mass transfer. However, there are some data points that deviated from the correlations at the low *Re* region, with higher *Sh* or *Nu*, i.e. having high convective heat or mass transfer at even lower flow rate. These data points are usually found near the bifurcations. Thus, the proposed correlations could under-predict heat and mass transfer near the airway bifurcations.

2.3.4 Wall boundary conditions

The wall boundary condition is crucial in modeling airway thermodynamics. The ASL-lumen interface temperature is non-uniformly distributed in the airway and is not a simple function of the distance from the mouth. Moreover, the interface temperature must be able to oscillate with flow during ventilation. Because of these requirements, a two-layer wall model was adopted, in which one layer represents transient energy flux and the other represents net energy flux. The transient layer must allow fluctuation of the interface temperature in response to the oscillating energy flux for the model to agree with measurements (Primiano et al. 1988), and to avoid over-prediction of instantaneous energy flux. The interface temperature has a smaller fluctuation than the lumen temperature, ensuring that it is always higher (lower) than the lumen temperature during inspiration (expiration) to warm up (cool down) the air. As shown in Figure 2.8 (e) and (f), the inspiratory and expiratory interface temperatures increase with distance into the airways, but they always stay between the inspiratory and expiratory lumen temperatures.

The important variable in the steady layer is the temperature T_m at the interface between the transient layer and the steady layer because the ASL-lumen interface temperature T_R usually fluctuates around a value close to the magnitude of T_m. The equilibrium value of T_m is determined by the net energy flux and the thermal resistance of the steady layer. As shown in Figure 2.5, the upper lobes saturate at a shorter distance from the trachea than the lower lobes because of smaller energy flux in the upper lobes. Thus,

T_m must be adjusted dynamically to increase more rapidly with distance in the upper lobes, which can only be achieved via simulating energy flux using the two-layer energy balance-based boundary condition rather than prescribing temperature (Daviskas, Gonda, and Anderson 1990; Ferron, Haider, and Kreyling 1988; Hanna and Scherer 1986; Ingenito et al. 1986; Tsu et al. 1988; Zhang and Kleinstreuer 2003).

2.3.5 Conclusions and limitations

In summary, the 3D model can provide detailed local temperature and humidity data, and the proposed correlations from the current model can be used to estimate local convective heat and mass fluxes. One potential source of error in the current model is that, when solving the water vapor concentration transport equation, it is possible for some small regions to exceed 100% RH. In these regions water vapor should condense into water droplets, however this is a complex phenomenon that was not considered in the model. In the current results, the liquid to vapor ratio was generally less than 0.05%, therefore the formation of droplets was neglected. Specifically, at the regions where RH exceeded 100% the water vapor concentration was set to 100% RH, meaning that only the vapor portion at these regions was considered. A further potential source of error is, the assumption of 100% RH at the ASL-lumen interface. Based on the human water activity coefficient S = 0.995 (Warren H. Finlay 2001), the RH at the interface could be 99.5%. A test case using subject C at 6 L/min gave differences of overall energy fluxes in the central airways of only 2.96% and 4.12% on inspiration and expiration, respectively, for 100% and 99.5% RH.

The current model could readily be coupled with particle tracking to study the deposition of hydroscopic aerosols whose sizes vary with humidity (W. H. Finlay and Stapleton 1995), and/or the predicted evaporative flux from the ASL could be coupled with an epithelial cell model (Warren, Crampin, and Tawhai 2010) to predict the hydration state of the periciliary liquid (Lin, Tawhai, and Hoffman 2013). While the 3D model could immediately be used for these applications, it has several limitations that limit its

application to very generalized studies. First, the non-linear deformation of the airway (Jahani et al. 2014; Yin et al. 2013) and the change of regional ventilation distribution (Venegas et al. 2005) during respiration were not considered. Second, the tissue properties and the tissue and ASL thicknesses were assumed to be uniform over the entire lung, and only 1D heat conduction in the wall normal direction was considered in the tissue layer for simplicity and computational efficiency. Third, the study only considered air-water vapor, therefore the proposed correlations did not include *Pr* for use of different gases (Javaheri et al. 2013) and could under-predict heat and mass transfer near bifurcations.

Table 2.1 Subject Information

	Age/Gender /Race	BMI	Total Volume(L) /Mesh Size (Million)	% Vital Capacity	Ventilation Distribution*	
Subject A	32/ Male/ White non-Hispanic	21.6	0.215/ 9.76	85	LUL	0.148
					LLL	0.348
					RUL	0.126
					RML	0.060
					RLL	0.319
Subject B	20.0/ Male/ White non-Hispanic	22.33	0.128/ 5.71	78	LUL	0.208
					LLL	0.279
					RUL	0.186
					RML	0.064
					RLL	0.264
Subject C	69.0/ Female/ White non-Hispanic	26.63	0.170/ 7.76	98	LUL	0.185
					LLL	0.281
					RUL	0.123
					RML	0.056
					RLL	0.355

* LUL, left upper lobe; LLL, left lower lobe; RUL, right upper lobe; RML, right middle lobe; RLL, right lower lobe.

Table 2.2 Cases Set Up

	Minute Ventilation (L/min)	Period (s)	Tidal Volume (L)	Maximum Flow Rate (L/s)	Maximum Re in Trachea
Case 1	6	5	0.5	0.314	1180~1380
Case 2	15	2	0.5	0.785	2960~3450
Case 3	30	2	1	1.57	5910~6890

Table 2.3 Summary of Parameters

Parameter	Description	Value	Unit	Ref.
k	Molecular conductivity of moist air	2.68e-02	$J\ m^{-1}s^{-1}K^{-1}$	Tawhai and Hunter (2004)
D	Molecular diffusivity of water vapor in air	2.7e-05	$m^2\ s^{-1}$	Tawhai and Hunter (2004)
C_p	Thermal capacity of moist air	1080	$J\ kg^{-1}K^{-1}$	Tawhai and Hunter (2004)
ρ	Density of moist air	1.12	$kg\ m^{-3}$	Tawhai and Hunter (2004)
α_1	Thermal diffusivity of layer 1 (water properties)	1.43e-07	$m^2\ s^{-1}$	Tawhai and Hunter (2004)
k_{asl}	Conductivity of ASL (water properties)	0.6	$J\ m^{-1}s^{-1}K^{-1}$	Tawhai and Hunter (2004)
ΔH	Latent heat of vaporization	2.41e06	$J\ kg^{-1}$	Tawhai and Hunter (2004)
ν	Kinematic viscosity of moist air	1.65e-05	$m^2\ s^{-1}$	Morvay and Gvozdenac (2008)
β	Coefficient of volumetric expansion of air	3.22e-03	K^{-1}	Nellis and Klein (2009)
R'	Steady layer thermal property	1.67e05	$s\ m^{-1}$	-

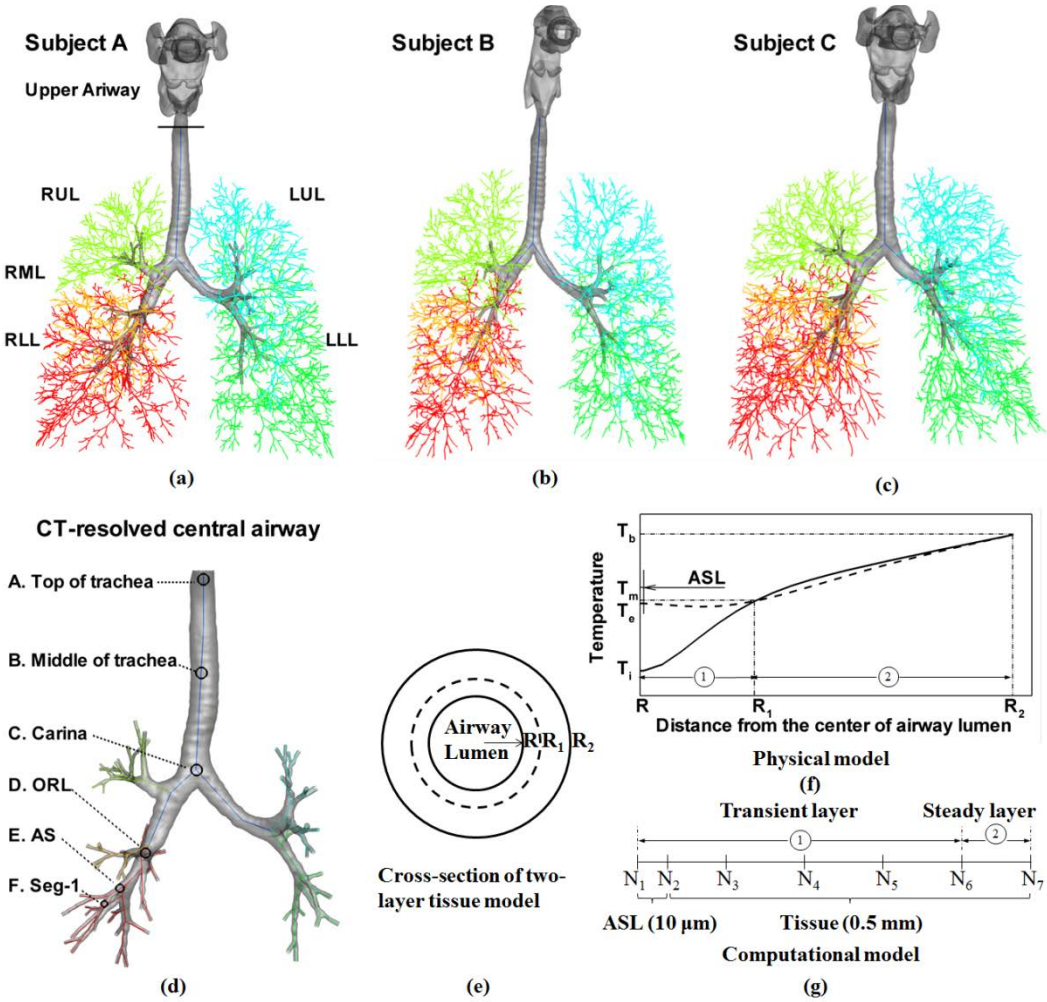

Figure 2.1 3D CT-based airway geometric models overlapped with 1D airway models (up to the 5th Horsfield order) of: (a) subject A, (b) subject B and (c) subject C. (a) LUL, left upper lobe (blue); LLL, left lower lobe (green); RUL, right upper lobe (yellowish-green); RML, right middle lobe (yellow); RLL, right lower lobe (red). (d) Anatomical landmarks according to McFadden et al. (1985): ORL, orifice of RLL; AS, anterior segmental bronchus; Seg-1, sub-segmental bronchus. The temperature data measured by McFadden et al. (1985) along the path following these landmarks are compared with the both 1D and 3D CFD predictions. (e) Schematic of the cross section of the two-layer tissue model. (f) Schematic of the tissue temperature distribution. In the physical model, the radius of the interface is R. The radius of the transient layer is R1, where tissue temperature stays at Tm after reaching quasi-steady state. The radius of the steady layer is R2, where temperature is fixed at body temperature Tb. Solid line represents the tissue temperature profile at the end of inspiration where the interface temperature equals Ti, while dashed line represents the tissue temperature profile at the end of expiration where the interface temperature equals Te. (g) Schematic of the 1D mesh for the tissue model. There are a total of seven nodes, denoted by Ni, where i=1,2,3,4,5,6,7.

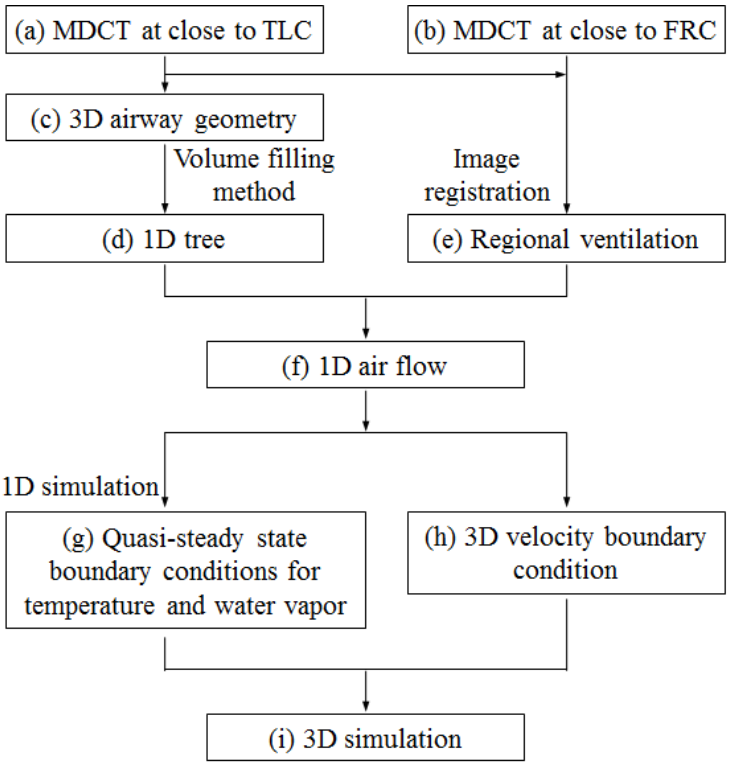

Figure 2.2 The flow chart illustrating the procedures to perform the 3D CFD thermodynamic simulation using a MDCT-based human airway model. Two MDCT scans were required at (a) close to the total lung capacity (TLC), and (b) close to the functional residual capacity (FRC). (c) 3D airway geometry was generated from the CT image at TLC by 'Apollo' software. (d) 1D tree was generated from 3D geometry by the volume filling method.(Tawhai and Hunter 2004) (e) The two images were used to generation regional ventilation by image registration.(Yin et al. 2010) (f) With the regional ventilation and 1D tree, the flow rate distribution of 1D airway can be computed. (g) 1D CFD was run to determine the quasi-steady state boundary conditions for temperature and water vapor. (h) 3D flow rate distribution at the outlets can be determined from the 1D airflow obtained from (f). (i) With all the inputs, 3D CFD simulation can be conducted.

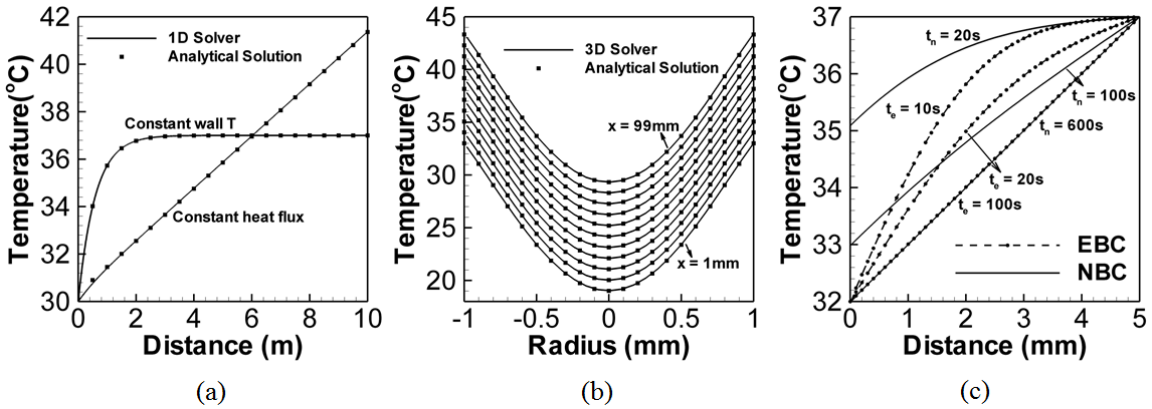

(a) (b) (c)

Figure 2.3 (a) The validation of 1D solver on the pipe-flow cases of constant wall temperature and constant heat flux. The distributions of lumen temperature in the axial direction are compared with the analytical solutions. (b) The validation of 3D solver. The points are extracted from the diameters of the cross-sections of the cylinder where the axial distances from the inlet x are x=1, 10, 20,…, 80, 90, and 99 mm. (c) The validation of 1D conduction equation with essential and natural boundary conditions (EBC and NBC). The tissue temperature profiles at t_e =10 s, 20 s, 100 s, of EBC case are shown. The tissue temperature profiles at t_n =20 s, 100 s, 600 s, of NBC case are shown. The steady states of both cases exhibit linear profiles.

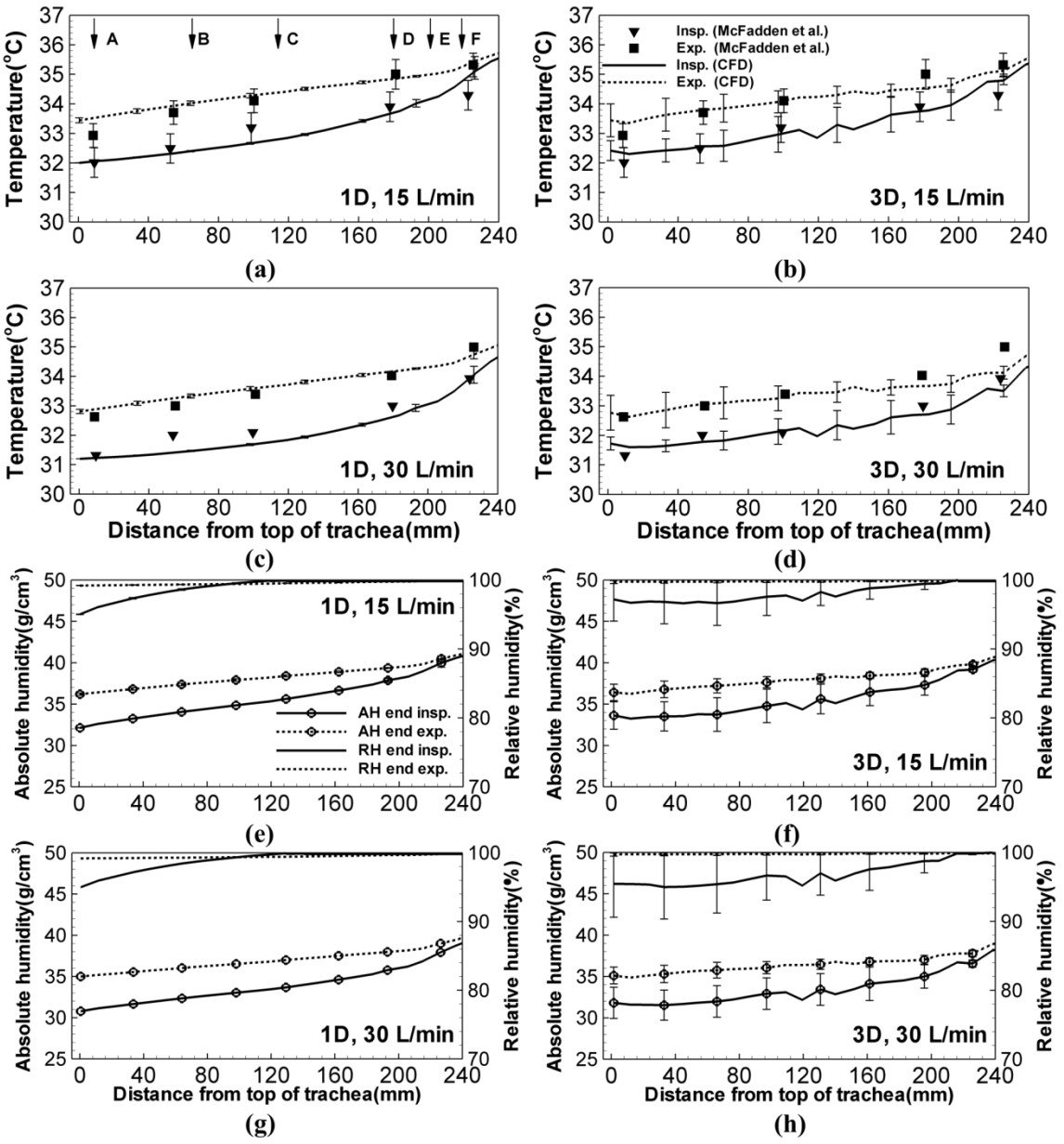

Figure 2.4 Validation of temperature distributions predicted by (a) and (c) 1D model, and (b) and (d) 3D model at 15 L/min and 30 L/min. Distributions of absolute humidity and relative humidity of (e) and (g) 1D model, and (f) and (h) 3D model at 15 L/min and 30 L/min. Experimental temperature data were taken from McFadden et al. (1985) along the path depicted in Figure 2.1 (d). For the 1D CFD data, the error bars present the standard deviation between three subjects. For the 3D CFD data, the error bars present the standard deviation within the three spheres extracted from three subjects at the locations with same distances from the top of the trachea.

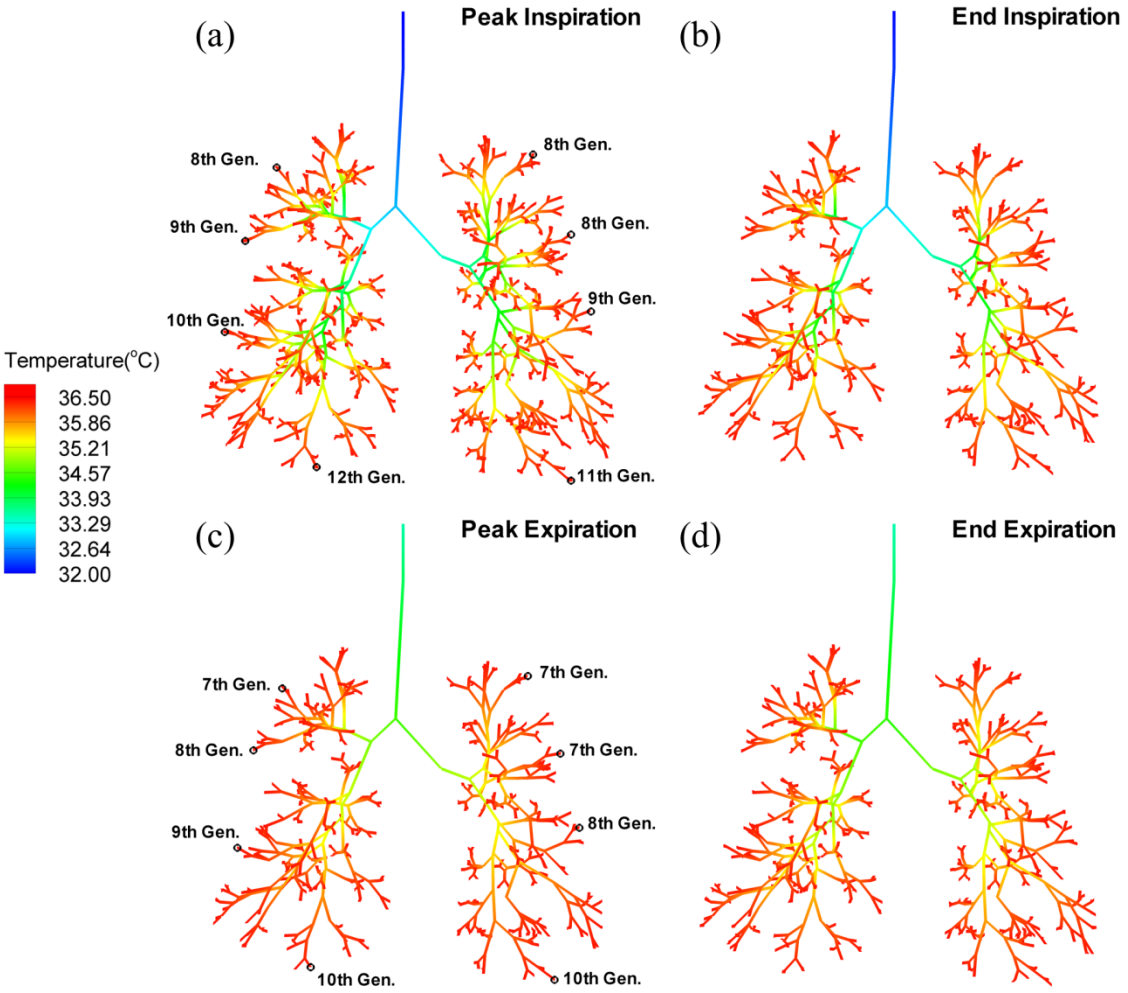

Figure 2.5 Distributions of the 1D lumen temperature of subject A with 15 L/min at four time points: (a) peak inspiration, (b) end inspiration, (c) peak expiration, and (d) end expiration. Airway branches after ISB are blanked.

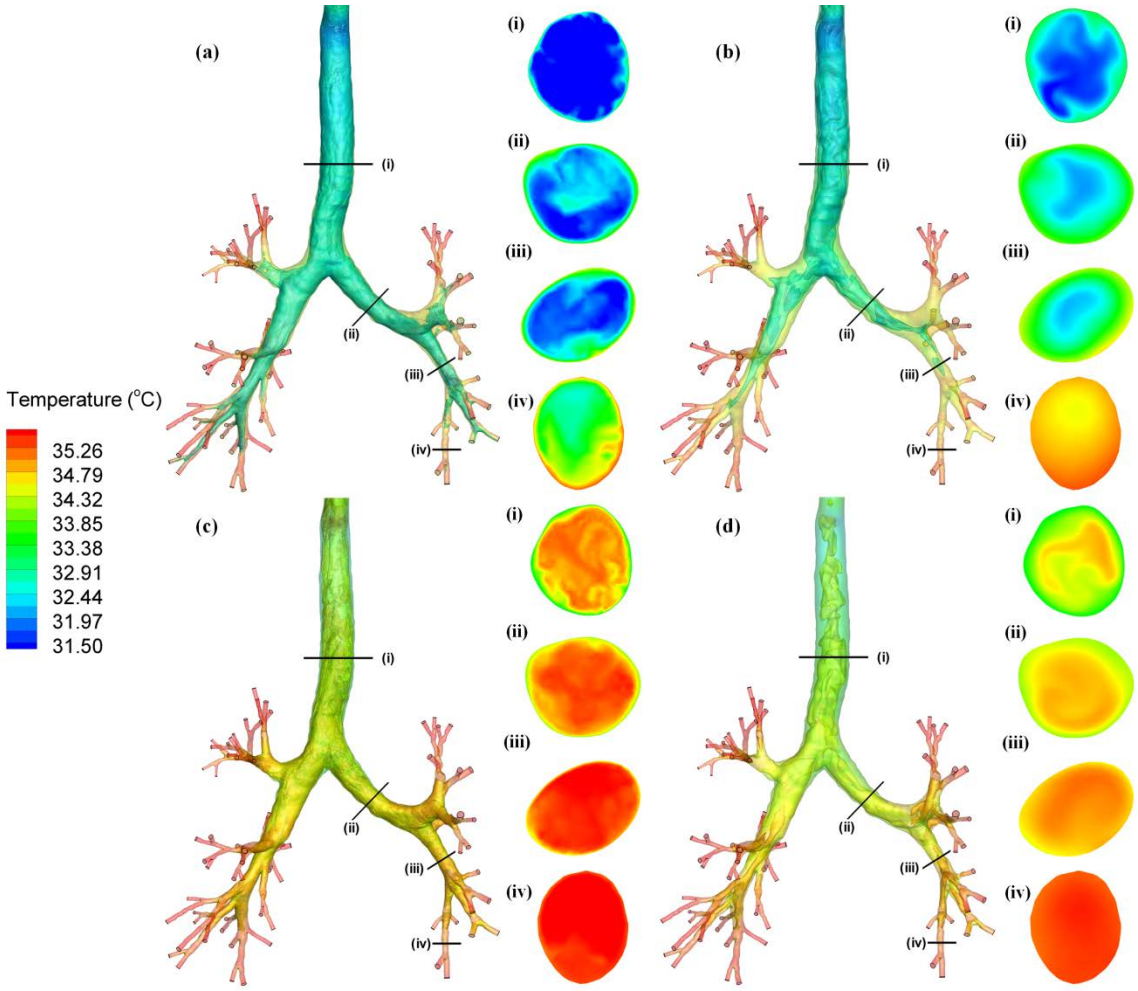

Figure 2.6 Distributions of the 3D airway lumen and wall temperatures of subject A with 15 L/min at four time points: (a) peak inspiration, (b) end inspiration, (c) peak expiration, and (d) end expiration. The iso-surfaces of the lumen temperatures of 32 ºC and 32.5 ºC are plotted in (a) and (b). The iso-surfaces of the lumen temperatures of 34.5 ºC and 35 ºC are plotted in (c) and (d). Cross-sectional temperature contours are displayed at four locations at each time point.

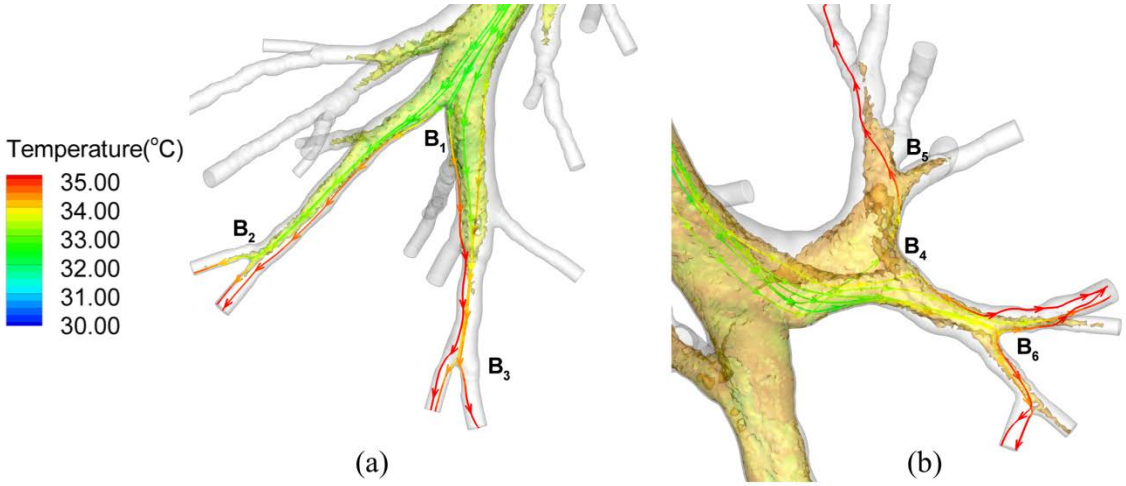

Figure 2.7 Cold air streams marked with streamlines color-coded with temperature at 6 L/min of subject A in: (a) RLL (the region with temperature above 34 ºC is blanked); (b) LUL (the region with temperature above 34.5 ºC is blanked).

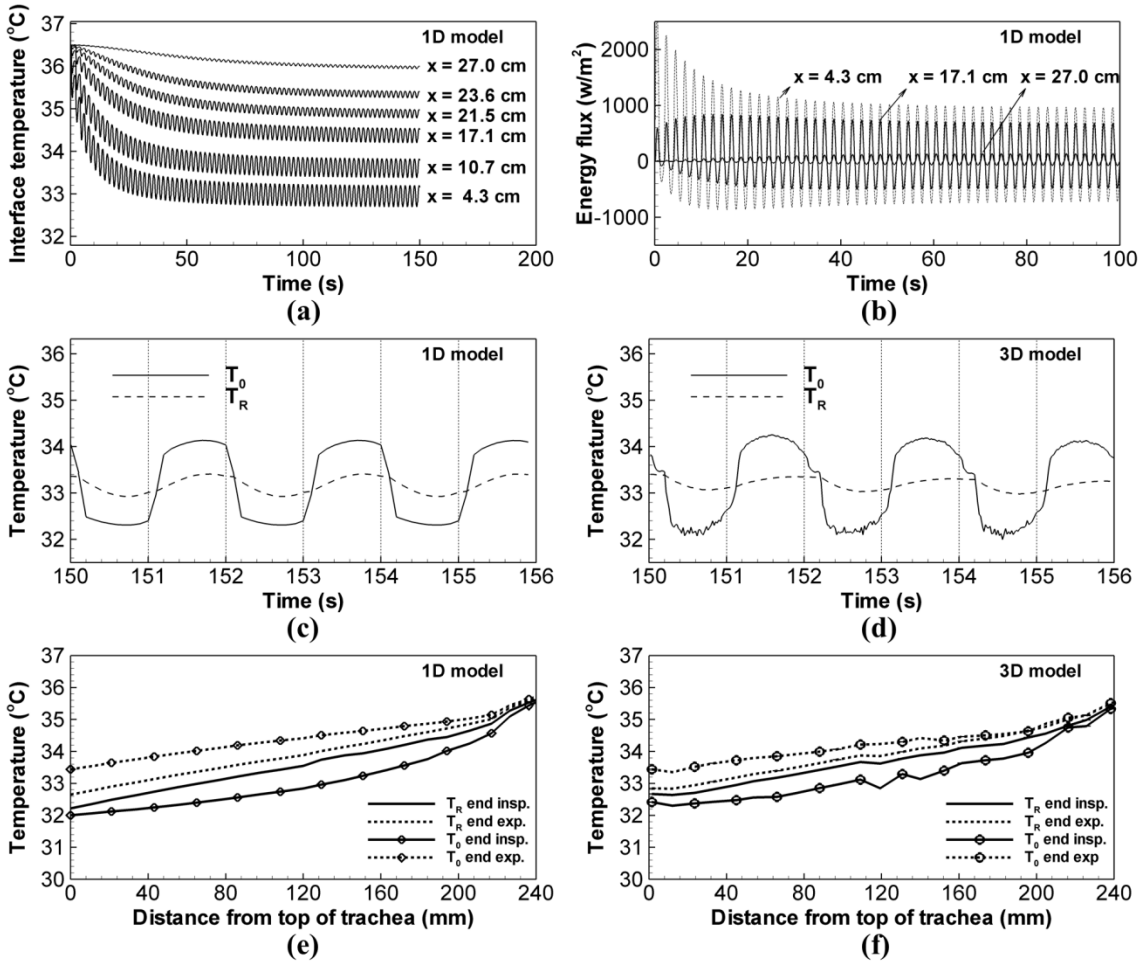

Figure 2.8 (a) Time histories of the ASL-lumen interface temperatures T_R at six locations in the 1D model along the path defined in Figure 2.1(d); (b) Time histories of energy fluxes across the ASL-lumen interface at three locations along the path as in Figure 2.1 (d). The distance x of each location from the top of the trachea is labeled. The time histories of 1D (c) and 3D (d) interface temperatures T_R and average lumen temperature T_0 at the middle of trachea of subject C at 15 L/min. The interface temperature T_R and the average lumen temperature T_0 at end inspiration and end expiration of 1D (e) and 3D (f) as a function of distance along the path as in Figure 2.1 (d).

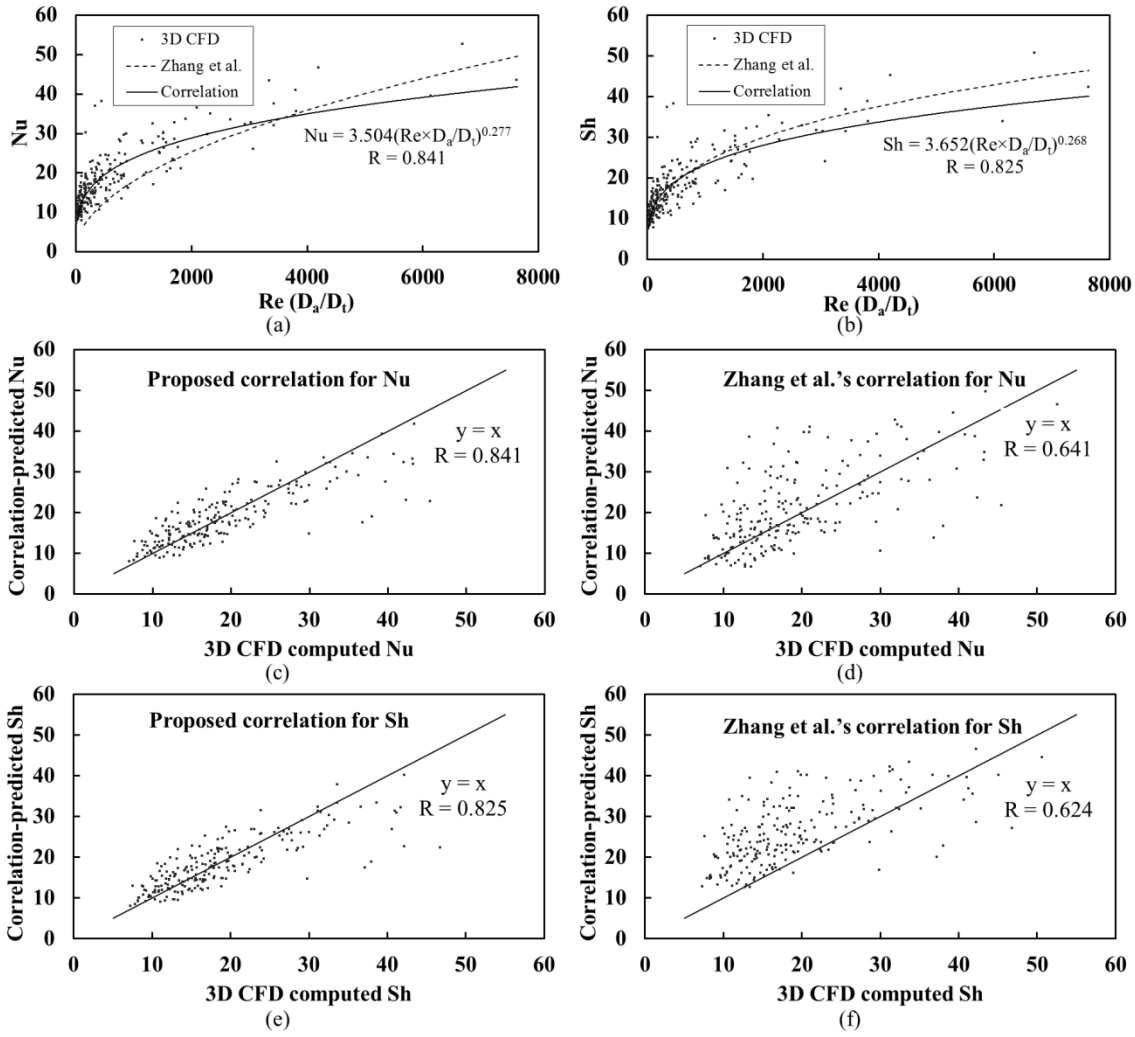

Figure 2.9 The correlation between: (a) *Nu* and *Re* (D_a/D_t), (b) *Sh* and *Re* (D_a/D_t). The correlation proposed by Zhang and Kleinstreuer (2003) is also plotted for comparison with D_a/D_t =1 because their correlation does not depend on D_a; (c) Nu predicted by the 3D CFD results are plotted against the values predicted by the proposed correlations for *Nu* (c) and *Sh* (e) and by Zhang et al.'s correlation for *Nu* (d) and *Sh* (f). The identity solid lines are plotted for comparison.

CHAPTER 3

WATER LOSS PREDICTION

To understand water loss in the ASL at the segmental level, we have previously developed and validated both 1D and 3D thermo-fluid CFD models with realistic wall boundary conditions for temperature and humidity, and have applied these models to characterize temperature and humidity distributions in human airways. In this chapter, the 3D and 1D models are applied to study the regional distributions of water loss rate in MDCT-based human airways. A 6-path model with airways up to the 22^{nd} generation is further used to assess the characteristics of water loss in airways beyond CT-image. The comparison of 3D and 1D CFD data serves to highlight the role played by secondary flows in regional water loss rate of ASL.

3.1 Methods

Volumetric multi-detector-row computed tomography (MDCT) lung images from three human subjects, acquired under separate studies (NIH grants HL064368 & EB005823) with the University of Iowa IRB and radiation safety committee approval, were used in this study. The three subjects were the same subjects used in a previous computational study (Wu et al. 2014). All subjects were normal non-smokers: subject A was a 32 year-old male with BMI of 21.6; subject B was a 20 year-old male with BMI of 22.33; subject C was a 32 year-old female with BMI of 26.63. Imaging was acquired with the subjects placed in the supine body posture and coached to breath-hold near total lung capacity. Scanning was performed using a Siemens Sensation 64-slice MDCT scanner (Forchheim, Germany; scan parameters: 120 kV, 75-100 mAs, 0.75-0.13 mm slice thickness, 0.5-0.6 mm slice spacing, 1.00-1.25 pitch, and B35 reconstruction kernel).

The 3D CT-based airway models are reconstructed from segmentations of the MDCT images and consist of the upper (viz. extra-thoracic) airways and the central airways that resolve the surfaces of up to six or seven airway generations (Wu et al. 2014).

For example, the 3D CT-based upper (or central) airways for subject A corresponds to the portion of the 3D CT-based airway model above (or below) the horizontal line marked with "Top of trachea" in Figure 3.1(a). The 1D CT-based central airway models are composed of the skeletons and segmental diameters of the corresponding 3D CT-based central airways models. At the most distal CT-resolved segments, the 1D airway model is supplemented using a volume-filling (VF) algorithm (Tawhai et al. 2004) which generates an anatomically-consistent subject-specific 1D VF airway tree that extends to the terminal bronchioles. Figure 3.1 displays the 3D CT-based airway models overlaying with their corresponding 1D CT-based central airway tree and 1D VF tree. Hereafter, the '1D tree' means the conducting airway tree that consists of the 1D CT-based central airway tree and the VF airway tree, and the '3D CT-based model' consists of the upper and central airways unless "upper" or "central" is used.

In addition to the above airway models, a 'six path' 3D model was created for subject A (hereafter referred to as the '6-path model') as shown in Figure 3.1(b), for assessment of water loss beyond the 3D CT-based airway. The 6-path model consists of the vocal cords above the trachea, the 3D CT-based central airways and - beyond CT resolution - 6 paths of 3D peripheral airways that extend up to the 22^{nd} generation (Shinjiro Miyawaki et al. 2014). The six paths comprise the airway segments in the 1D VF tree that go through the LB1, LB4, LB10, RB1, RB4 and RB10 segmental bronchi, respectively. These segments are modeled as 3D cylinders using the diameters, orientations and lengths in the 1D VF tree as discussed by Lin, Tawhai, and Hoffman (2013) and Lin et al. (2009). The six paths used here are the same paths selected by the Severe Asthma Research Program (SARP), to study alterations of airway tree structure in asthmatic patients (Castro et al. 2011). The mesh of the 6-path model consists of 9.88 million tetrahedral elements with a non-dimensional distance of the first grid point from the wall of $y+ = 4.8$ in the trachea at 15 L/min. This mesh is comparable to that of the CT-based model for subject A

with 9.76 million tetrahedral elements and y+ = 4.4 in the trachea at 15 L/min. For a mesh sensitivity test, please refer to Chapter 2 and Wu et al. (2014).

The 3D thermo-fluid CFD approach solves the incompressible Navier-Stokes equations along with the transport equations for temperature and water vapor concentration using a large-eddy simulation technique (C.-L. Lin, Tawhai, and Hoffman 2013; C.-L. Lin et al. 2007; Wu et al. 2014). The 1D model only solves the 1D transport equations for temperature and water vapor concentration, using the 1D flow rate distribution derived from image registration (Yin et al. 2010), and the velocity radial profile given by Eq.(3.2) (Wu et al. 2014). At the airway wall, a heat conduction equation is solved, and energy balance is enforced at the interface between the airway lumen and the ASL for both 1D and 3D models.

After solving 3D temperature and water-vapor-concentration transport equations, the evaporative flux J_{evap} (μm/s) at the airway wall is calculated by Fick's law using

$$J_{evap} = \frac{1}{\rho}(D + D_T)\frac{\partial C}{\partial r}\Big|_{R^-} \tag{3.1}$$

where C denotes the water vapor concentration. ρ = 1.0e03 kg m^{-3} is the density of water in the ASL, D (2.7e-05 m^2 s^{-1}) and $D_T(= \nu_T/St)$, are the molecular and turbulent diffusivities, respectively, of water vapor in air. St is the turbulent Schmidt number of water vapor in air (assumed to be equal to turbulent Prandtl number taken as 0.9 (Kays and Crawford 1993)) and ν_T is Vreman's subgrid-scale eddy viscosity (Vreman (2004) which reduces to zero for laminar flow. D_T is set to zero for the 1D model and the effect of turbulence is lumped into θ in Eq. (2). In this case the assumed radial profiles of velocity, temperature and water vapor concentration take the form of:

$$\varphi(r) = \varphi_R + (\varphi_0 - \varphi_R)\left(1 - \left(\frac{r}{R}\right)^{\theta}\right) \tag{3.2}$$

where φ represents velocity, temperature, or water vapor concentration. φ_0 is the value at the center of the circular lumen, and φ_R is the value at the interface of airway lumen and

wall. θ is assumed to depend on the Reynolds number (Tawhai and Hunter 2004; Wu et al. 2014). Substitution of Eq. (3.2) with $\varphi = C$ into Eq. (3.1) yields $J_{evap} = D\theta(C_R - C_0)/(\rho D_a/2)$, where D_a is the local equivalent diameter computed as $D_a = (4A_L/\pi)^{1/2}$ with A_L=local cross-sectional area. To improve the 1D solver prediction on the evaporative flux, instead of using $\theta = Re/50$ as in Wu et al. (2014), θ is reformulated as described in the following two steps.

First, a mass flux balance equation is enforced at the interface between the airway lumen and the ASL, where the mass flux convected away from the airway wall equals the mass flux diffused from the ASL to the airway lumen:

$$\frac{1}{\rho}h_0(\overline{C_R} - \overline{C_m}) = \frac{1}{\rho}\overline{(D + D_T)\frac{\partial C}{\partial r}\Big|_{R^-}} \tag{3.3}$$

where h_0 is the mass transfer coefficient, $\overline{C_R}$ is the local water vapor concentration at the interface of ASL and lumen. $\overline{C_m}$ is the lumen water vapor concentration weight-averaged by the local mass flow rate, viz. $\overline{C_m} = 1/\dot{m}\int \rho u C \cdot dA_L$, where $\dot{m}$ is the mass flow rate, and u and C are the velocity and the water vapor concentration, respectively, expressed by Eq. (3.2). The overhead bar denotes the averaged value over a distance of D_a along a segment. R^- denotes the gradient at the lumen side of the interface. Equations (3.2) and (3.3) give $Sh = 2(\theta + 1)$, where Sh is the Sherwood number.

Second, Sh was found to be correlated with ReD_a/D_t in Wu et al. (2014), where Re is the branch Reynolds number, and D_t is the equivalent diameter of the trachea. By fitting Sh computed from 3D CFD data in the airways of the three subjects under investigation at three minute ventilations at both peak inspiration and peak expiration using the method of least squares, one obtains:

$$Sh = 3.521(Re\frac{D_a}{D_t})^{0.281}, R = 0.856 \tag{3.4}$$

Thus, for $ReD_a/D_t > 6.68$, which corresponds to transitional and turbulent flows,

$$\theta = 1.7605\left(Re\frac{D_a}{D_t}\right)^{0.281} - 1 \tag{3.5}$$

whereas for $ReD_a/D_t \leq 6.68$, $\theta = 2$ (Tawhai and Hunter 2004), which is derived from the parabolic velocity profile in fully developed laminar pipe flow.

All cases (listed in Table 3.1) use the room air condition of 27.6 °C and 34.7% RH as in the experimental study of McFadden et al. (1985) A sinusoidal waveform is used, with the periods and tidal volumes of 5 s and 0.5 L, 2 s and 0.5 L, 2 s and 1 L, for the simulations of 6, 15, and 30 L/min, respectively (Wu et al. 2014). The image-registration-based subject-specific flow boundary condition (Yin et al. 2010) is adopted to obtain lobar ventilation distributions as shown in Table 3.2. For each case, the 1D model (as in Wu et al. (2014)) was first solved for 200 breaths to allow the temperature and humidity to reach quasi-steady state. The 1D solutions were then provided to the 3D models (including the three CT-based models and one 6-path model) to initialize the conditions at the 3D airway wall, and to act as boundary conditions at the most distal 3D airway openings during expiration. For the 1D cases, the temperature and humidity inlet conditions at the top of the trachea were taken from the corresponding 3D cases (see Table 3.1) at the top of the trachea (see Figure 3.1). For more details, please refer to the Chapter 2 and Wu et al. (2014)

3.2 Results

3.2.1 Water loss validation

Water loss is defined as the volume of water lost due to evaporation over a minute over a region. In order to compare with existing measurement data of the overall water loss in the entire respiratory tract, column (e) (or (f)) in Table 3.3 shows the overall water loss estimated by the sum of the water loss in the 3D upper airways, the 3D (or 1D) CT-based central airways and the 1D VF airways. Please refer to the supplementary material for the unit conventions used for various quantities discussed here. The average overall water losses are 0.156, 0.359, and 0.662 mL/min at respective 6, 15, and 30 L/min based on the 3D CT-based central airways, while they are 0.157, 0.369, and 0.675 mL/min based on the 1D CT-based central airways. The differences are less than 3%. The upper airways are

responsible for about 77, 73, and 67 % of the overall water loss at (respectively) 6, 15, and 30 L/min, agreeing with the reported 71% and 59 % of water loss in the upper airways for breathing from nose and mouth, respectively (Hasan 2010). The VF airways are responsible for about 3, 10, and 18 % of the overall water loss at 6, 15, and 30 L/min, respectively. The increased percentage in the VF airways is because increased ventilation draws a greater proportion of unsaturated inspiratory air deeper into the lung.

3.2.2 Time history of evaporative flux

The time histories of the 1D and 3D overall evaporative fluxes from the ASL within the CT-based central airways are shown in Figure 3.2 for three breathing cycles, where positive (or negative) flux is taken as evaporation (or condensation). During inspiration (or expiration), the lumen humidity is lower (or higher) than the values at the interface between airway lumen and ASL. The humidity gradient between the lumen and the interface drives the water vapor to evaporate (or condense) from (or to) the ASL. However, the overall condensation during expiration is only 32% of the overall evaporation during inspiration, indicating that the ASL experiences a net water loss during breathing. Overall, both 1D and 3D transient evaporative fluxes agree well.

3.2.3 Water loss rate distribution

The water loss rate is defined as the net loss of water by evaporation during respiration per area per min and has the unit of $\mu L \cdot cm^{-2} \cdot min^{-1}$. The water loss rate is considered so that water loss from epithelial cells per unit area at any specific region of interest can be quantified. Figure 3.3 shows the contours of the 3D water loss rate in the central airways. The general trends in the three subjects show good consistency. Specifically, the water loss rate is elevated at the bifurcation and then decreases along its inner wall. The water loss rate at the outer wall of the bifurcation is usually the lowest. There may exist some regions with negative water loss rate, meaning that there is more water condensation than evaporation from the surface, for example, at the outer wall of

carina where swirls and recirculations are usually formed. The upper lobes experience less water loss than the lower lobes. In the case of 6 L/min, the water loss rate becomes quite small in the small distal branches, whereas in the cases of 15 L/min and 30 L/min more unsaturated air penetrates deeper into the small airways and the water loss rate remains high even at the small distal branches. In contrast, Figures 3.4 (a), (b) and (c) show that the distribution of 1D water loss rate regardless of ventilation exhibits a generally monotonic feature that does not sensitively capture local variations. As the 1D distributions for the three subjects exhibit similar features, only subject A is shown. Figures 3.4 (b), (d) and (e) compare the distributions of water loss rate predicted by the 1D model, the 3D CT-based model and the 3D 6-path model of subject A at 15 L/min, respectively. The two 3D models yield almost the same distribution of water loss rate. The 6-path model also shows that the water loss rate drops to zero quickly after passing the 3D CT-based central airways. While the current study is focused on the intra-thoracic airways, for the sake of completeness, Figure 3.4 (f) shows the water loss rate distributions in the upper airways obtained from the 3D CT-based airway model of subject A. The results show that the water loss rate tends to be higher near the constricted and/or curved regions where high flow-induced shear stress may occur as shown in locations marked as (i)-(iii). Moreover, it increases with increasing ventilation (not shown).

To further quantify the above observations, the water loss rate is presented by lobe as well as by generation for both 1D and 3D data. Figure 3.5 shows the average water loss rate by lobe with (Lobe 0, LUL, LLL, RUL, RML, RLL, Overall)=(trachea + primary bronchi, left upper lobe, left lower lobe, right upper lobe, right middle lobe, right lower lobe, CT-based central airways). The results show that the water loss rate increases almost proportionally to increasing flow rate. Both models predict an increase of about 0.02 $\mu L \cdot cm^{-2} \cdot min^{-1}$ in the average water loss rate in the CT-based airways per liter increase in minute ventilation. However, the trends predicted by both models are quite different. The 1D water loss rate is the highest in Lobe 0, whereas the 3D water loss rate is the highest in

the lower lobes. Furthermore, the differences between upper lobes and lower lobes are much greater in 3D than in 1D. The ratio of RUL to RLL water loss rate in 1D and the ratio of RUL to RLL water loss rate in 3D are statistically different.

To further investigate the differences between lobar water loss rates predicted by 1D and 3D models, we performed the 3D experimental case using subject A at 15 L/min, but with a uniform ventilation distribution in the upper and lower lobes as shown in Table 2. The 1D and 3D lobar distributions of the normalized water loss rate (=lobar water loss rate / average water loss rate in five lobes; it is used for fair comparisons between 1D and 3D, minimizing the absolute value differences for clarity.) in Figure 3.6 6 (a) and (b) for the control and experimental cases resemble those of the lobar ventilation in the inserts on the upper left corner. However, when comparing the ratios of the water loss rates in the upper lobes to those of the lower lobes in 1D and 3D, the 3D results always have lower ratios than those of 1D regardless of ventilation distribution. For example, in the control case, the ratio of LUL to LLL water loss rate and the ratio of RUL to RLL water loss rate in 1D are 0.85 and 1.01, respectively, while they are 0.80 and 0.66 in 3D. In the experimental case, the ratio of LUL to LLL water loss rate and the ratio of RUL to RLL water loss rate in 1D are 1.16 and 1.61, respectively, while they are 0.97 and 1.01 in 3D. That is, regardless of the ventilation distribution, the 1D model tends to accommodate higher percentage of cold dry air in the upper lobes than the 3D model. The underlying reasons will be explained in the Discussion section.

Figure 3.7 (a) shows that both 1D and 3D models predict a decrease of the water loss with increasing generation number except from the 2^{nd} to 3^{rd} generation. Comparing with the water loss in the entire 1D tree, Figure 3.7 (b) reveals that the peak water loss after the 0^{th} generation (trachea) roughly occurs between the 4^{th} and 6^{th} generations and then decreases monotonically. To eliminate the effect of the total surface area of the airway wall, the water loss rates by generation in the 1D and 3D CT-based central airway models are displayed in Figure 3.7 (c), where both models predict completely different trends. That

is, the 3D model predicts an increase of the water loss rate with increasing generation, while the 1D model predicts the highest water loss rate in the trachea and a monotonic decrease with generation. Figure 3.7 (d) compares the water loss rates in the entire 1D tree, the 3D 6-path model, and the 3D CT-based model of subject A and the average values of three CT-based models. The 6-path model predicts almost the same trend with the CT-based model in the first 5 generations. The water loss rates from the 6^{th} to 9^{th} generation predicted by the two 3D models still exhibit the similar trend, but are quantitatively different because the 6-path model has more branches than the CT-based model in these generations. The 6-path data starts to decrease at the 8^{th} generation and reduces to zero at about the 14^{th} generation. In contrast, the 1D data shows a monotonic decrease beginning from the trachea. Hence, the 3D-predicted water loss rate first increases and then decreases. The enhanced water loss rate in 3D may be caused by the secondary flows formed at bifurcations that are prohibited in 1D, as will be discussed later.

3.2.4 Shear stress vs. evaporative flux

As both wall shear stress and evaporation are important factors in regulating ASL (Tarran et al. 2005; Warren, Crampin, and Tawhai 2010), the relationship of these two quantities is examined. Theoretically, shear stress is related to evaporative flux because local velocity gradients affect local gradients of temperature and water vapor concentration. As shown in Figure 3.3-Figure 3.5 and Figure 3.7, with increasing flow rate the water loss rate increases almost proportionally. Figure 3.8 (a) and (b) show that the distribution of overall evaporation along line *AB* in an airway segment residing in the LLL of subject A in Figure 3.3 (b) is similar to the distribution of average shear stress during inspiration, having a correlation coefficient of 0.967. Furthermore, the distribution of overall condensation is similar to the average shear stress during expiration, having a correlation coefficient of 0.978. In contrast, the 1D predicted values at the same location exhibit almost constant values mainly because of missing local geometric features. Figure

3.8 (c) shows that the time histories of evaporative flux and shear stress at a sample point *c* along line *AB* follow the imposed sinusoidal breathing waveform. Thus, the results in Figures 3.8 (a), (b) and (c) suggest that local shear stress is strongly correlated with local evaporative flux in both time and space. Figure 8 (d) further shows that dimensionless wall shear stress $\tau^* = \tau/(\nu^2\rho_a/{D_a}^2) = (u^*D_a/\nu)^2 = (Re^*)^2$, where $Re^* = u^*D_a/\nu$ with $u^* = \sqrt{\tau/\rho_a}$ and dimensionless mass transfer coefficient ${h_0}^* = h_0D_a/D$ can be correlated as ${h_0}^* = 1.15\,{\tau^*}^{0.272}(R = 0.842)$, where $\nu = 1.65e-05$ m^2 s^{-1} is the kinematic viscosity of moist air, and $\rho_a = 1.12$ kg m^{-3} is the density of moist air.(Morvay and Gvozdenac 2008) More than half of the data points, especially at low minute ventilation, have their dimensionless shear stresses varying within the range of [0, 50] ×1000. In this range, ${h_0}^*$ increases rapidly with τ^*. The remaining data points in the range of [50, 300] ×1000 exhibit a moderate increase of ${h_0}^*$ with τ^*.

3.3 Discussion

3.3.1 Water loss distribution

Both 1D and 3D overall water losses in the entire respiratory tract are in good agreement with existing *in vivo* measurements. Specifically, Freund and Young (1995) reported that the respiratory water losses under room air conditions of RH = 65%; T_I = 25 °C are about 0.167 mL/min for resting conditions, 0.5 mL/min for light to moderate exercise conditions, and 1 mL/min for moderate to heavy exercise conditions. Tabka, Jebria, and Guénard (1987) reported an overall water loss of 0.275±0.049 mL/min after 5 min at rest breathing wet warm air (RH = 31%; T_I = 30 °C), and of 0.592±0.093 mL/min after 5 min of exercise in slightly heated ambient air (RH = 18%; T_I = 28 °C). In comparison, with the condition of RH = 34.7%; T_I = 27.6 °C in McFadden et al. (1985), the current 3D CFD model predicted 0.156, 0.359 and 0.662 mL/min at respective 6, 15, and 30 L/min, and the 1D model predicted 0.157, 0.369, and 0.675 mL/min. 6 L/min is comparable to a resting minute ventilation, and 30 L/min is comparable to moderate

exercise. To further validate the water loss predictions, additional benchmark cases with conditions in Tabka, Jebria, and Guénard (1987) (RH = 31%; T_I = 30 °C) and in Freund and Young (1995) (RH = 65%; T_I = 25 °C) were simulated. It is noted that these studies only indicated that the data were measured at resting conditions, but did not report actual minute ventilation values. The CT-based model of subject C was considered because the water loss of this subject is close to the average value of the three subjects (see Table 3). The reported range of ventilation at rest varies from 6 L/min to 10 L/min (Bell et al. 1996; Burki 1984), thus we performed simulations at 6 L/min and 10 L/min. The predicated water-loss values of 0.150 (at 6L/min) to 0.244 mL/min (at 10 L/min) are comparable to Tabak et al's. measurements of 0.275 ± 0.049 mL/min when using the condition of Tabak et al. and the predicted values of 0.123 (at 6L/min) to 0.195 mL/min (at 10 L/min) are comparable with the 0.167 mL/min observed by Freund et al. when using the Freund et al. conditions. From these results, it appears that minute ventilation and inspired humidity are more important factors than inspired temperature in affecting water loss. With the same inlet conditions, the water loss is nearly proportional to minute ventilation. Additionally, with the same minute ventilation, Freund et al.'s inspired condition of 25 °C and 65% RH (absolute humidity (AH) = 0.015 $kg \cdot m^{-3}$) comparing to Tabka et al.'s inspired condition of 30 °C and 31% RH (AH = 0.009 $kg \cdot m^{-3}$), the predicted water loss is lower in the Freund et al.'s case. This is because Freund et al.'s inspired absolute humidity is higher despite the lower inspired temperature. Therefore, both 3D and 1D models give reasonable predictions of the overall water loss.

The overall water loss is a function of both airway wall surface area and local water loss rate. Figure 3.7 (a) shows the distributions of both 1D and 3D water losses in the CT-based central airway tree by generation. The 1D model predicted higher water loss in the trachea, but slightly lower water loss in the 2nd and higher generations at 6 L/min (or from the 3rd generation at 30 L/min). Nonetheless, the 1D and 3D predicted water losses exhibit some similar trends, correlating to the surface area by generation. For example, Figure 3.7

(b) shows that the 1D water loss follows the change of surface area through the 4th generation (or the 6th generation depending on minute ventilation). After the 4th (or 6th) generation, as air is close to its saturation point, the water loss rate decreases at a faster rate than the increase of surface area. This results in a decrease of water loss. Water loss drops to zero when the isothermic saturation boundaries (ISB) are reached. The ISBs vary with the paths and flow rates as demonstrated previously by Wu et al. (2014) For peak inspiration at 15 L/min, saturation is reached at the 8th to 9th generation in the upper lobes and the 9th to 12th generations in the lower lobes as predicted by the 1D model. This is consistent with Fig. 7 (d). The water loss rates predicted by the 1D model drops to zero by around the 11th generation for all paths.

3.3.2 1D and 3D comparisons

Unlike the 3D model, the radial profiles of air velocity, temperature and humidity in the 1D model are assumed axisymmetric and their gradients are determined by the parameter θ in Eq. (3.2) such that with the same T_0 and T_R, a greater θ leads to a higher evaporative flux. Even though the correlations in Eq. (3.4) and the parameterization of θ in Eq. (3.5) used by the 1D model are derived empirically by fitting to the 3D CFD data, the 1D model is still not sensitive enough to capture local heat and mass transfer processes in the human airways that depend on local gradients of air velocity, temperature and humidity. This is first evident in the trachea, where the rate of water loss in the 1D model is far higher than for the 3D model. Because the 3D model captures complex flow structures, the gradient of humidity near the walls depends on actual physical processes. For example, the laryngeal jet might increase the evaporative water loss locally if the jet core impinges on the tracheal wall, while the recirculation would decrease the evaporative water loss. However, as θ in the 1D model is determined by *Re* and airway diameter (which are largest in the trachea), θ tends to over-predict the water loss rate in the trachea. The 3D non-axisymmetric distributions of temperatures and water vapor concentrations at

bifurcations also have significant influence on water loss rate, as reflected when studied by lobes and by generations.

3.3.3 Water loss rate by lobes

The use of subject-specific geometry and ventilation distribution is the primary cause of lobar difference in the water loss rates as shown in Figure 3.5. However, if comparing the LUL and LLL or RUL and RLL, two other reasons should be accounted for. First, the upper lobes are more proximal to the trachea compared with other lobes and therefore when air enters the upper lobes, it has traveled less distance than it has traveled when it enters the lower lobes. As a result, the temperature and humidity of air entering the upper lobes are usually lower, causing the upper lobes to be prone to losing more water. Second, the secondary flow formed at the carina on inspiration tends to distribute more cold air to the lower lobes. Hence the lower lobes are prone to greater water loss. For the 1D model, without secondary flow, the shortened path to the upper lobes contributes to the water loss rate difference. For the 3D model, with both of the above effects contributing, the second effect dominates, thus explaining the 1D vs. 3D model differences in the lobar water loss rate. These tendencies can be seen clearly with the comparison between the control case and experimental case in Fig. 6. With the uniform lobar ventilation, the 1D model's upper lobes have considerably higher water loss rates compared with the lower lobes, while in the 3D model, the secondary flow distributes cold air to the lower lobes, preventing significant increases in water loss rates in the upper lobes as those in 1D. In conclusion, the lower lobes tend to have higher water loss rates not only because of the higher ventilation to the lower lobes, but because of the secondary flow at the carina serving to asymmetrically distribute more cold air to the lower lobes as predicted only by the 3D model.

3.3.4 Water loss rate by generation

By eliminating the effect of surface area, Figure 3.7 (c) shows that the trends of 1D and 3D water loss rates are quite different. The elevated water loss rate in 3D CT-based airways as illustrated in Figure 3.3 can be attributed to convection-dominated secondary flows at bifurcations. As shown in Wu et al. (2014), after reaching the bifurcations the air in the center of the lumen is skewed toward the inner wall of the bifurcation, forming secondary flows. The central air is cooler, skewing the radial temperature profile. This skewed profile creates a higher gradient of water vapor concentration along the inner wall and elevates the water loss rate in the vicinity of the bifurcation as illustrated in Figure 3.3, contributing to an increase of the water loss rate as shown in Figure 3.7 (c). However, as air approaches saturation, the water loss rate gradually decreases to zero as shown in Figure 3.7 (d).

As previously described, the 3D splitting mechanism at the bifurcation only exists on inspiration. As a result, the 1D and 3D differences of water loss rate distribution by generation are only reflected in the overall evaporative flux distribution but not the overall condensation flux distribution. During inspiration the average 1D overall evaporative flux decreases with increasing generation, while the 3D evaporative flux increases with generation and then decreases. This resembles the trends of the 1D and 3D water loss rates in Figure 3.7 (c). However, during expiration the average 1D and 3D overall condensation fluxes by generation exhibit similar trends; that is, both decrease almost linearly with generation at 6 L/min, both remain almost constant with generation at 15 L/min, and both increase almost linearly at 30 L/min.

3.3.5 Inter-subject variability

Because water loss rate is proportional to the gradient of water vapor concentration at the airway wall, it depends on a) the local humidity difference between the airway lumen and the ASL; and b) the local velocity gradient, which depends on local airway structure

(e.g. diameter) and regional ventilation. However, as factor (a) contributes little to the inter-subject variability (Wu et al. 2014), the variability in water loss rate between subjects, as reflected in the error bars in Fig. 5, mainly comes from subject-specific airway diameter and regional ventilation. Comparing the regional water loss rates (by every generation in every lobe) for the three subjects with both 1D and 3D models, the maximum differences could vary from 5% to 52% of the average water loss rate in the three subjects. In addition, the presence of airway narrowing/constriction may increase inter-subject variability of water loss rate. Thus, regional water loss rate in diseases lungs is expected to exhibit greater inter-subject (Choi et al. 2013) and intra-subject (Venegas et al. 2005) variations.

3.3.6 Shear stress vs. water loss rate

Previous studies suggest that shear stress acting on airway wall epithelial cells helps the ASL to stay hydrated (Tarran et al. 2005), while severe water loss may contribute to mucociliary dysfunction. Thus, investigations into the correlation of shear stress and evaporative flux will help to provide subject specific patterns of ASL homeostasis (Lin, Tawhai, and Hoffman 2013). The outcomes will likely depend upon two counter effects: stress-related biological (epithelial) effects will stimulate water secretion while thermodynamic effects will stimulate water loss.

The correlation between local mass transfer coefficient and local shear stress was proposed to estimate local evaporative flux. Mathematically, an increase of shear stress correlates with an increase of the mass transfer coefficient h_0. Thus, with $J_{evap} = h_0/\rho(\overline{C_R} - \overline{C_m})$ shear stress correlates with the evaporative flux. With minimum information such as temperature, airway diameter and flow rate, the level of local water loss can be estimated. More importantly, physiologically, the correlation between shear stress and the mass transfer coefficient reveals the inter-relationship between the evaporative flux and shear stress and correlates them everywhere inside the airway. As

both evaporative flux and shear stress serve to affect cellular functions, understanding their inter-relationship helps to study their impact on biologic function.

When correlating evaporative flux and shear stress, we found that there are two ranges. In the first range (most data samples from 6 L/min are inside this region), the shear stress is relatively small, and the mass transfer coefficient increases with shear stress rapidly. That is evaporative flux and possibly water loss rate tend to increase fast with the increase of velocity gradient. However, the second range (most data samples from 30 L/min or at constrictions are inside this region) shows that extremely high velocity gradients will cause extremely high shear stresses but not mass transfer coefficients. In this case, the evaporative flux might be only moderately elevated. Interestingly, the ATP release increases rapidly with shear stress from [0, 0.06] Pa (Tarran et al. 2005). This is inside the region where mass transfer coefficient also increases rapidly with the shear stress, as the first range is roughly corresponding to the [0, 0.1] Pa without nondimensionalization.

3.3.7 Potential application and limitation

For epithelial cells, an increase of shear stress can also trigger ATP release resulting in fluid secretion (Tarran et al. 2005). This may compensate for the velocity gradient-induced water loss. However, the question remains as to whether or not the fluid secretion is sufficient to result in evaporative water loss when undergoing state changes such as rest to exercise or from relaxed to constricted airway smooth muscle. Such state changes would be expected to place the system within different range of the shear stress – mass transfer coefficient relationship. Such questions can be answered with the coupling of epithelial cell models and thermo-fluid CFD described here. That is, via the prediction of evaporation coupled with cellular secretion to predict the ASL depth (Lin, Tawhai, and Hoffman 2013; Warren, Crampin, and Tawhai 2010), hence evaluating the dehydration of ASL directly. This may also provide insightful information to better understand the pathophysiology of diseases such as cystic fibrosis.

The prediction of regional water loss rate could potentially be applied to asthmatic lungs with severe airway constriction. As regional ventilation distribution and airway diameter are statistically different between normal and asthma patients (Choi et al. 2013), the water loss rate distribution for the two groups might be statistically different. Quantitative analysis could be carried out to assess the effect of morphologic changes on airway dehydration in asthma patients. Airway constriction may induce elevated water loss, causing vulnerability to dehydration. This could increase sensitivity to exercise-induced bronchoconstriction in a subset of asthma patients (Weiler et al. 2010).

A limitation of the work presented here lies in the fact that the correlation of shear stress with mass transfer coefficients only emphasizes the effect of velocity gradients; regions near bifurcations may deviate from the correlations established here due to elevated mass transfer induced by secondary flow. Another limitation of this study is that the airway geometrical models are assumed rigid during simulation. The CFD studies with deformable airway were reported in Yin et al. (2013). Its effect on water loss rate is yet to be investigated.

Table 3.1 Case information: Three 3D CT-based airway geometric models are utilized to evaluate inter-subject differences. Their corresponding 1D airway trees are used to evaluate the difference between 3D and 1D models. The 3D and 1D CFD simulations employ subject-specific lobar ventilation, and consider three different minute ventilations (listed in Table 1). The 3D and 1D models are those that are primarily used to address the three objectives of this study. The 3D models extend only as far as the CT image resolution allows. To determine whether the characteristics of water loss rate in the 3D peripheral airways (beyond CT resolution) is consistent with the findings for the 3D CT-based central airway, a 6-path model was designed (including CT-based large airways plus smaller 'generated' airways). To test the impact of different assumptions for flow distribution, the lobar ventilation was altered from subject-specific (the control case) to uniform distribution (the experimental case) in a 3D and a 1D model. These are the final cases listed in the table.

Subject	Geometric Model	Boundary Condition	CFD Model	Minute Ventilation
Major cases				
A	CT-based	Subject-specific lobar ventilation	3D	6, 15 and 30 L/min
B	CT-based	Subject-specific lobar ventilation	3D	6, 15 and 30 L/min
C	CT-based	Subject-specific lobar ventilation	3D	6, 15 and 30 L/min
A	1D tree	Subject-specific lobar ventilation	1D	6, 15 and 30 L/min
B	1D tree	Subject-specific lobar ventilation	1D	6, 15 and 30 L/min
C	1D tree	Subject-specific lobar ventilation	1D	6, 15 and 30 L/min
Test cases				
A	6-path	Subject-specific ventilation	3D	15 L/min
A	CT-based	Uniform lobar ventilation	3D	15 L/min
A	1D tree	Uniform lobar ventilation	1D	15 L/min

Table 3.2 Percent distributions of subject-specific and uniform lobar ventilations: Because the flow distribution to RML is the smallest, the percent distribution to RML for the experimental case (with uniform lobar ventilation) is set essentially to the value for its control counterpart (with subject-specific lobar ventilation).

Subject	LUL	LLL	RUL	RML	RLL
	Subject-specific lobar ventilation				
A	0.148	0.348	0.126	0.059	0.319
B	0.208	0.279	0.186	0.063	0.264
C	0.185	0.281	0.123	0.056	0.355
	Uniform lobar ventilation				
A	0.235	0.235	0.235	0.060	0.235

*LUL, left upper lobe; LLL, left lower lobes; RUL, right upper lobe; RML, right middle lobe; RLL, right lower lobe.

Table 3.3 The overall water loss (mL/min) of the three subjects with three minute ventilations

MV.	Sub.	(a) 1D CT-based central airways	(b) 3D CT-based central airways	(c) 3D upper airways	(d) 1D VF airways	(e) Total water loss based on (a)+(c)+(d)	(f) Total water loss based on (b)+(c)+(d)	[(e)-(f)]/(e): 1D vs. 3D CT-based models (%)
6 L/min	A	3.38E-02	3.86E-02	1.19E-01	3.31E-03	1.56E-01	1.61E-01	-2.98%
	B	2.76E-02	2.02E-02	1.25E-01	4.98E-03	1.58E-01	1.50E-01	4.93%
	C	3.85E-02	3.68E-02	1.15E-01	4.88E-03	1.58E-01	1.57E-01	1.09%
	Avg.	3.33E-02	3.19E-02	1.20E-01	4.39E-03	1.57E-01	1.56E-01	1.01%
15 L/min	A	7.69E-02	7.22E-02	2.68E-01	3.12E-02	3.76E-01	3.71E-01	1.27%
	B	5.85E-02	4.13E-02	2.65E-01	3.53E-02	3.59E-01	3.42E-01	5.04%
	C	7.82E-02	7.02E-02	2.54E-01	3.85E-02	3.71E-01	3.63E-01	2.21%
	Avg.	7.12E-02	6.12E-02	2.62E-01	3.50E-02	3.69E-01	3.59E-01	2.84%
30 L/min	A	1.24E-01	1.15E-01	4.64E-01	1.12E-01	7.00E-01	6.91E-01	1.30%
	B	9.60E-02	7.42E-02	4.35E-01	1.16E-01	6.47E-01	6.25E-01	3.49%
	C	1.19E-01	1.11E-01	4.34E-01	1.26E-01	6.79E-01	6.71E-01	1.19%
	Avg.	1.13E-01	1.00E-01	4.44E-01	1.18E-01	6.75E-01	6.62E-01	1.99%

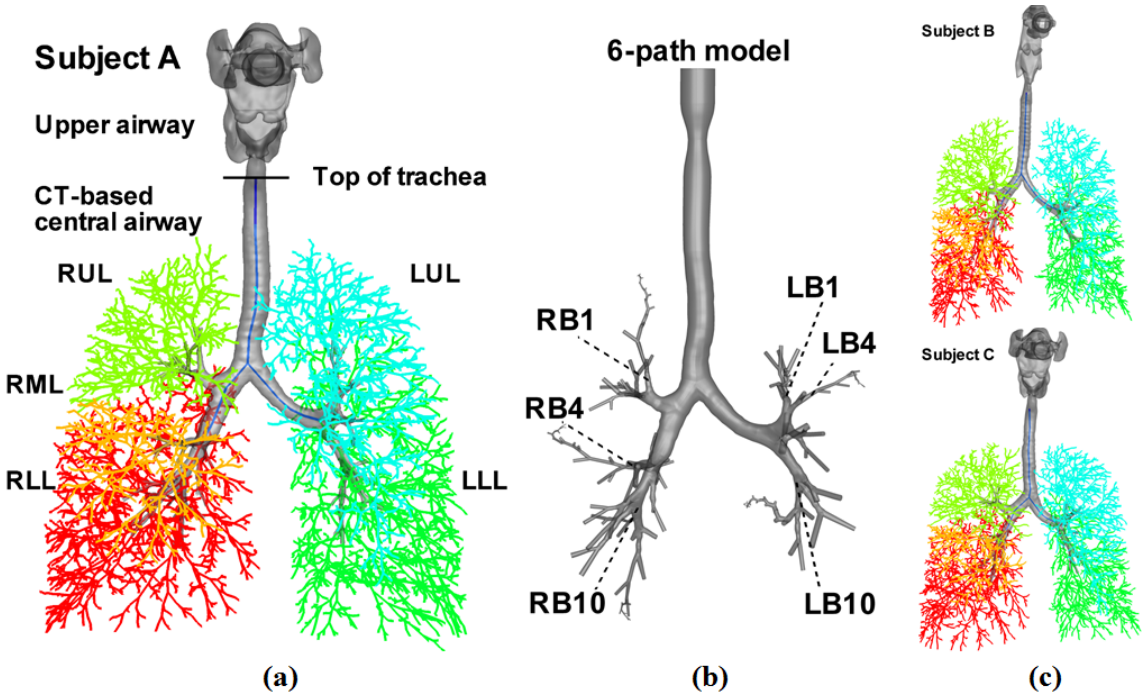

Figure 3.1 3D and 1D airway geometrical models of subject A in (a), and subject B and subject C in (c). LUL, left upper lobe (blue); LLL, left lower lobes (green); RUL, right upper lobe (light green); RML, right middle lobe (orange); RLL, right lower lobe (red). The CT-based models consist of the upper airways (above the top of trachea) and CT-based central airways (below the top of trachea). (b) The 3D 6 path model of subject A, which consists of the vocal cords, the CT-based central airways and, beyond CT resolution, 6 paths of cylindrical VF airways extending up to the 22nd generation. These 6 paths go through the RB1, RB4, RB10, LB1, LB4, and LB10 segmental bronchi as marked, respectively.(Castro et al. 2011)

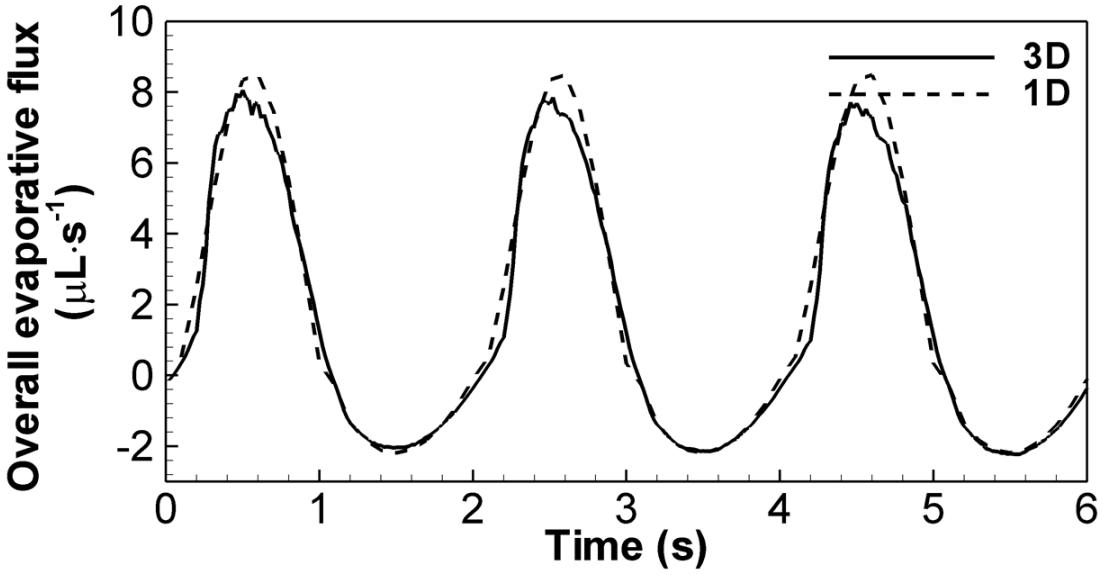

Figure 3.2 The time histories of 1D and 3D overall evaporative fluxes in CT-based central airways of subject C over a period of three cycles at 15 L/min.

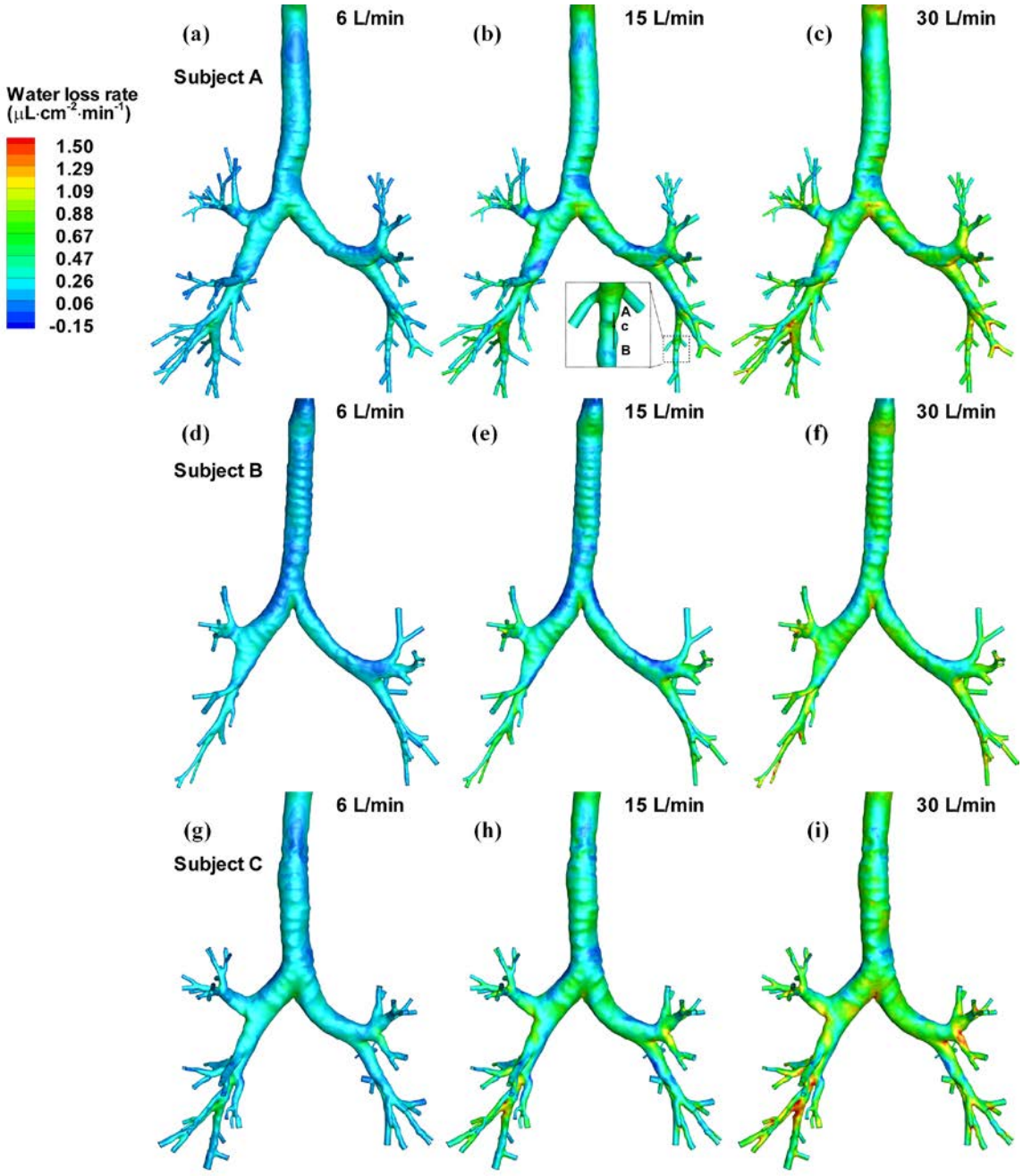

Figure 3.3 Distributions of the water loss rates of three subjects at three minute ventilations. The data along line AB in the insert of (b) are extracted for further analysis in Figure 3.8.

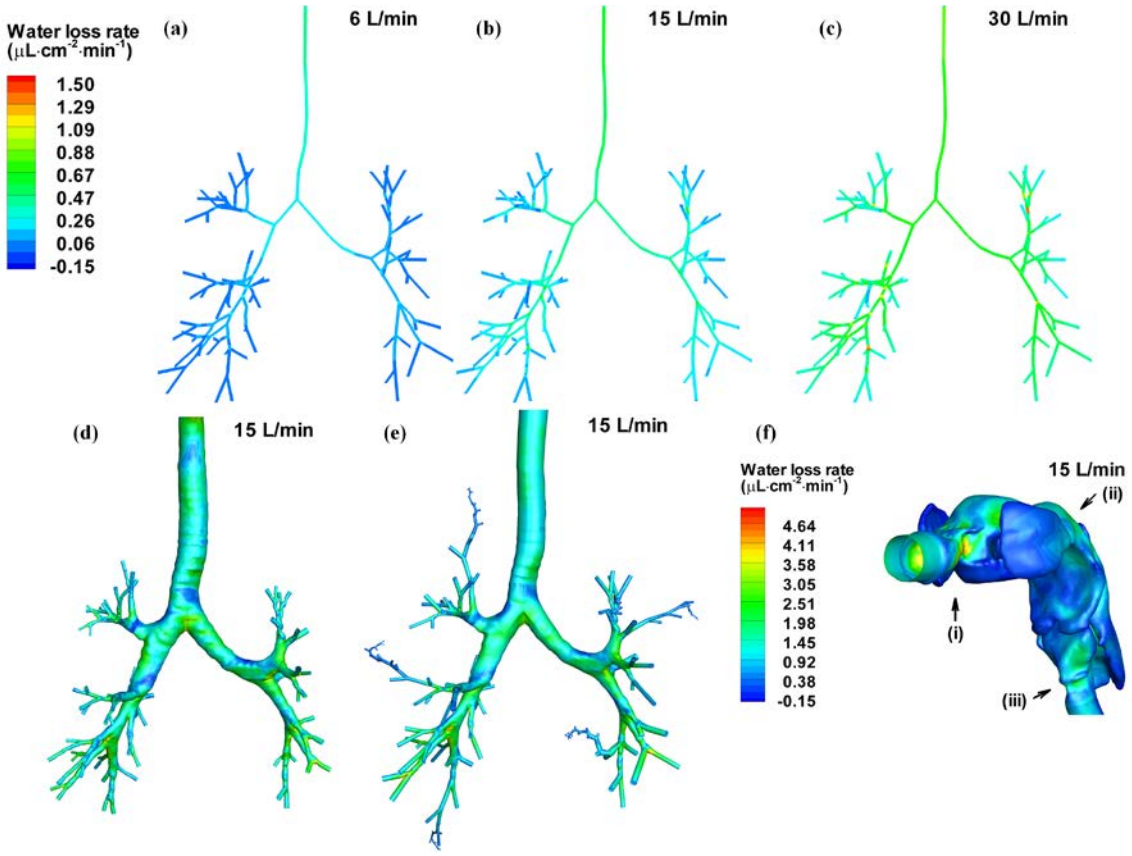

Figure 3.4 Distributions of the water loss rate of subject A in the 1D CT-based central airways at: (a) 6 L/min, (b) 15 L/min and (c) 30 L/min. (b), (d) and (e) compare the distributions of the water loss rate of subject A predicted by the (b) the 1D model, (d) the CT-based model and (e) the 6-path model, respectively. (f) Distribution of water rate in the upper airway of subject A at 15 L/min. (i), (ii) and (iii) mark the locations of high water loss rate.

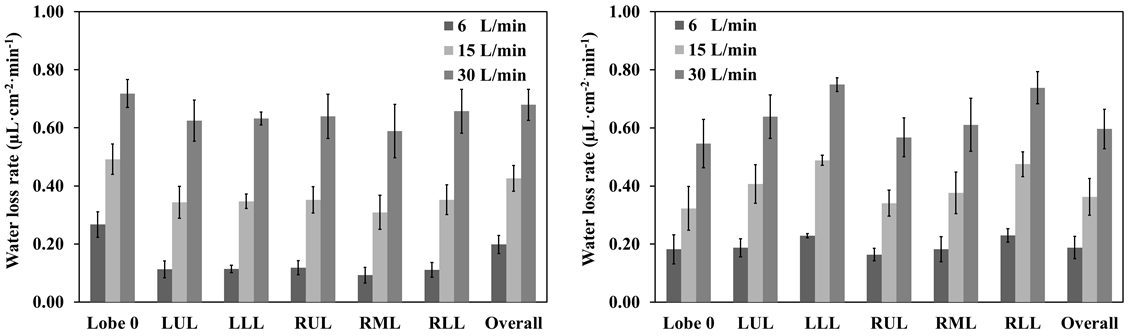

Figure 3.5 The average water loss rates ($\mu L \cdot cm^{-2} \cdot min^{-1}$) of the trachea and primary bronchi (Lobe 0), five lobes, and the CT-based airways (Overall) at three minute ventilations based on: (a) the 1D models and (b) the 3D CT-based models, of threes subjects.

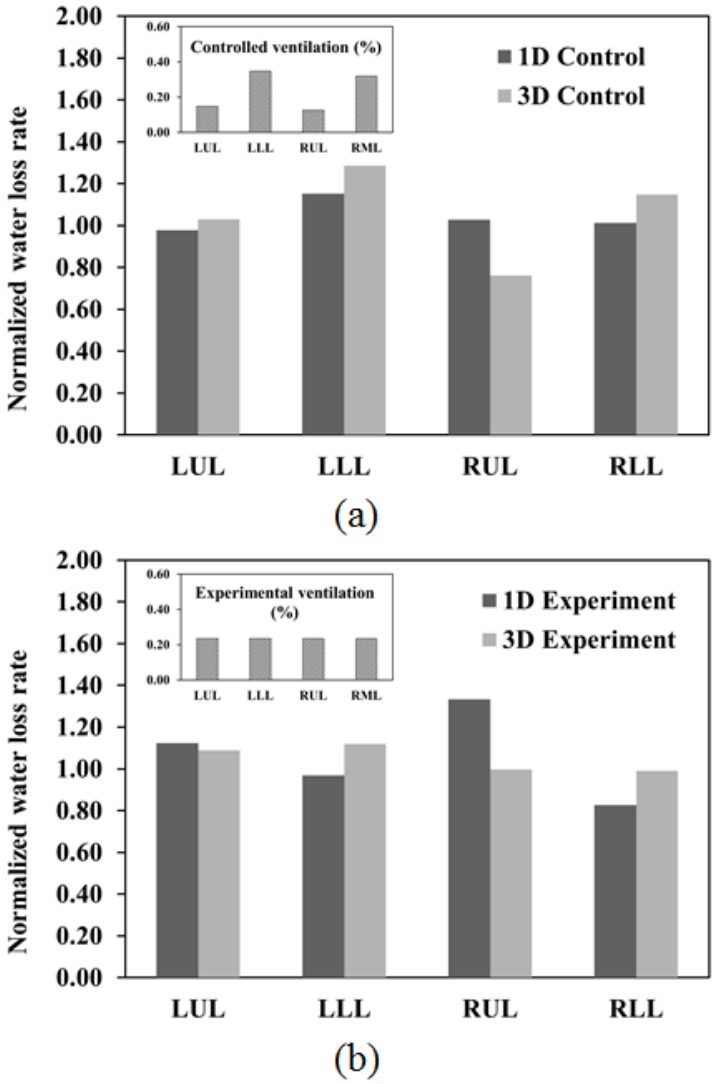

Figure 3.6 Comparison of the normalized lobar water loss rates by the average water loss rate in five lobes predicted by 1D and 3D CT-based models: (a) the control (original) cases with subject-specific lobar ventilation and (b) the experimental cases with uniform lobar ventilation for subject A at 15 L/min. The percent distributions of lobar ventilation for the control and experimental cases are shown in the inserts on the upper left corner.

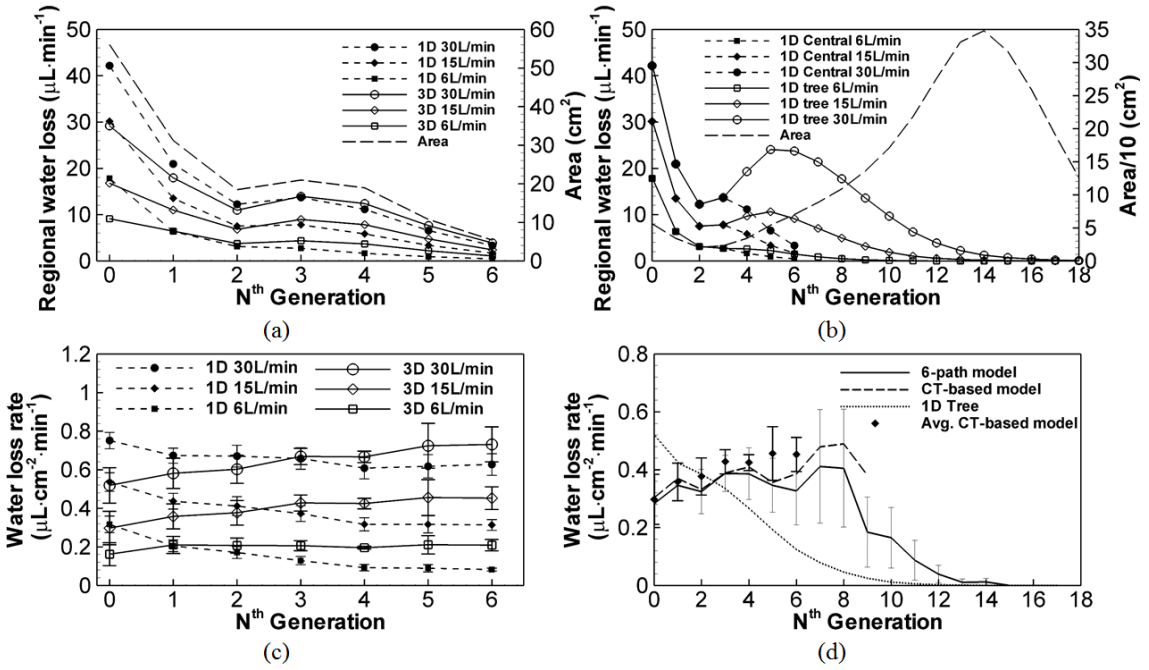

Figure 3.7 (a) The average water loss at the n^{th} generation of 1D and 3D CT-based central airways at the three minute ventilations. The surface area in each generation of the CT-based airway model is also plotted. (b) The average water loss at the n^{th} generation of the entire 1D tree comparing to that of the 1D CT-based central airway model (see "1D central" in the legend). The surface area in each generation of the 1D tree is plotted. (c) The average water loss rate of all three subjects at the n^{th} generation of 1D and 3D in the CT-based central airways at the three minute ventilations. (d) The water loss rates of subject A predicted by the 6-path model, the CT-based model and the 1D tree model, comparing to the average water loss rate of the three CT-based models at the n^{th} generation. The error bars of both 1D and 3D data in (c) and 3D CT-based model data in (d) show the standard deviation of the three subjects in a given generation. The error bars of the 6-path model data in (d) show the standard deviation of the water loss rates of the airway branches in a given generation.

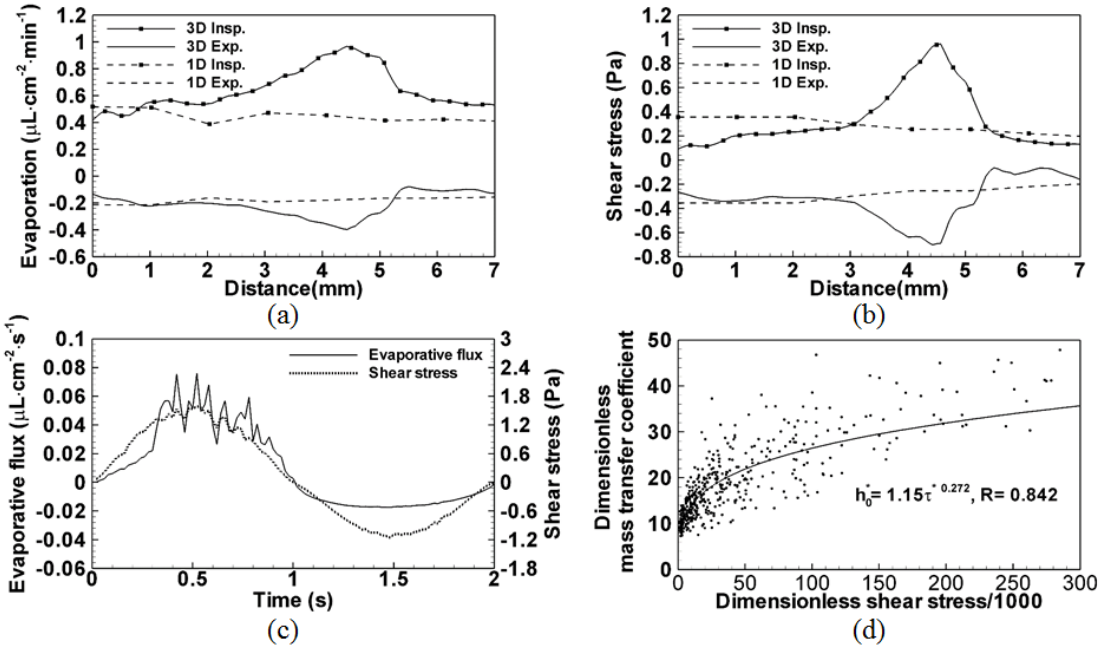

Figure 3.8 (a) Distributions of the overall evaporation during inspiration and the overall condensation during expiration along line AB in the insert of Fig. 3 (b). The 1D evaporation and condensation at the same location are also plotted. (b) Distributions of the average shear stress during inspiration and the average shear stress during expiration along line AB. The 1D shear stresses during inspiration and expiration are also plotted. (c) Time histories of shear stress and evaporative flux at point c in the insert of Fig. 3(b). Their distributions resemble the imposed sinusoidal wave-form. (d) The correlation between non-dimensional local mass transfer coefficient ($h_0{}^*$) and non-dimensional local shear stress (τ^*). Data points are extracted from the three subjects at peak inspiration and peak expiration of the three minute ventilation.

CHAPTER 4

EPITHELIAL CELL MODEL

In this chapter, an ion-channel conductance model is developed to couple the previously developed fluid secretion model and ATP model to capture the mechanical forces induced fluid secretion. In the *result* section, the model is tested and validated with multiple experimental data sets.

4.1 Methods

4.1.1 An overview of the model

Figure 4.1 shows the schematic view of both normal (NL) and CF epithelial cells. The cell model reacting to mechanical forces are summarized into eight basic processes (Zuo 2007):

1. Mechanical forces trigger ATP release.
2. ATP metabolizes into adenosine diphosphate (ADP), adenosine monophosphate (AMP), adenosine (ADO) and inosine (INO).
3. ATP binds to receptor purinoceptor 2 ($P2Y_2$) and triggers phosphatidylinositol 4,5-bisphosphate (PIP_2) metabolites into inositol trisphosphate (IP_3) and diglyceride (DAG). IP_3 activates intracellular calcium release. Intracellular Calcium activates CaCC channel to increase Cl^- secretion.
4. ADO binds to receptor adenosine A_{2b} and increases cyclic adenosine monophosphate (cAMP), which subsequently activates CFTR channel and increases Cl^- secretion.
5. An increase of DAG concentration activates enzyme protein kinase C (PKC), which then activates CFTR channel.
6. CFTR channel inhibits ENaC channel, decreasing Na^+ absorption. However, there exists contradictory evidence that CFTR fail to inhibit ENaC.(Nagel et al. 2005)

7. The depletion of PIP_2 inhibits ENaC channel, decreasing Na^+ absorption.
8. As ion channels change extracellular ion concentrations, osmotic gradients drive water flux through the apical cell membrane. That is, an increase of Cl^- secretion increases PCL depth, whereas an increase of Na^+ absorption decreases PCL depth.

Thus, we present three models performing the aforementioned processes: (a) an ATP model (processes 1 and 2), (b) an ion-channel conductance model (processes 3 to 7), (c) a fluid secretion model (FSM) (processes 8). The differences between NL and CF epithelia cells are that steps 4, 5 and 6 in Figure 4.1 (b) involving CFTR channels are dysfunctional in CF cells due to mutations in the CFTR gene. This chapter first briefly discusses the ATP model and FSM, and then introduces the method to construct the ion-channel conductance model.

4.1.2 The ATP model

The ATP model was developed and validated by Zuo et al. (2008) (see Figure 4.2 (a)). The extracellular ATP is released by cyclic shear stress, compressive stress and cilia strain. In this study, all three types of forces are tested separately. We assume that the concentrations of ATP released due to different types of stress in airways are additive (Herschlag et al. 2013), of which every type is modeled as follows.

First, Button et al. (2013) reported that cilia strain can trigger the ATP release J_{ATP_CS}. As no better single function can describe the relationship between the mucus viscosity (% LMA) and [ATP], interpolation between measurement data is used as shown in Fig. 2 (b). During simulation, the [ATP] release due to the cilia strain is assumed constant. For NL epithelial cells, the mucus is close to 0.15 % LMA, the [ATP] in PCL is 4.2 nM. For CF epithelial cells the mucus is close to 0.3 % LMA, the [ATP] in PCL is 44.2 nM.(Button et al. 2013) In the model, the base level of [ATP] is 1.79 nM. Without any other inputs, if the cilia strain is considered, the [ATP] is 4.25 nM for NL cells; the [ATP] is 44.5 nM for CF cells. In this study, unless otherwise noted, the cell model does not

account for the effect of cilia strain. Second, Button, Picher, and Boucher (2007) found that ATP is released by cyclic compressive pressure (CCP) J_{ATP_CCP} as shown in Figure 4.2 (c). The release of ATP could be described by an algebraic equation $J_{ATP\_CCS} = P_{max}\Delta P/(K_p + \Delta P)$, where ΔP is the average change in CCP, K_p and P_{max} is fitted to match the curve. Third, Tarran et al. (2005) found that ATP is released by cyclic shear stress J_{ATP_CSS} as shown in Figure 4.2 (d). As no better single function can describe the relationship between [ATP] and cyclic shear stress, interpolation of measurement data is used. Finally, the total ATP release $J_{ATP} = J_{ATP\_CS} + J_{ATP\_CCP} + J_{ATP\_CSS}$ is added to the overall ATP change in the PCL predicted by the ATP metabolism model, where a set of ODE equations are solved (Zuo 2007).

4.1.3 Fluid secretion model

The FSM was developed, extensively tested and validated by Warren, Crampin, and Tawhai (2010). As shown in Fig. 1, this model includes three apical membrane channels: CaCC, ENaC and CFTR, and two basolateral membrane channels: basolateral chloride channel (BCC) and Calcium-activated potassium channel (CaKC). It also includes a Na-K-2Cl cotransporter and an ion pump sodium-potassium adenosine triphosphatase (Na^+/K^+-ATPase) on the basolateral sides. Figure 4.3 shows the 33% hypotonic challenge by Okada et al. (2006) The cell swell after hypotonic solution is added. As the Ca^{2+} activation is not included in the FSM, it is compared with experimental data with suppressed Ca^{2+} activation.

4.1.4 Ion-channel conductance model

Although PCL depth regulation by the three apical channels has been extensively investigated (Button, Picher, and Boucher 2007; Herschlag et al. 2013; Tarran et al. 2005; Tarran et al. 2006; Zuo 2007), the underlying complex biochemical reactions have not yet been fully developed. Zuo (2007) developed the model using functions of sodium ion and chloride ion permeability to connect the ATP model and an ion/water transport model

(similar to FSM). Here instead of lumping the five regulatory pathways in the processes 3 to 7 into two ion permeability functions, we propose to lump the 5 regulatory pathways into three ion-channel conductance functions with ATP and ADO as variables. In this way, it bypasses solving the actual biochemical reactions inside each regulatory pathway, while each regulatory pathway is independently descried and fully accounted. As illustrated in the schematic view of Figure 4.1, it can be deduced the dependence of pathways on various variables that the conductance $G_{CaCC} = f(ATP)$, $G_{ENaC} = f(ATP, ADO)$, $G_{CFTR} = f(ATP, ADO)$ for NL cells. For CF cells, the conductance G_{CaCC} is the same as in NL cells, $G_{ENaC} = f(ATP)$, $G_{CFTR} = 0$. Thus, we proposed the following method to construct these functions.

First, databases such as shown in Figure 4.4 (a) are created. It is found that with different combinations of G_{CaCC}, G_{ENaC}, G_{CFTR} the FSM gives different PCL depth regardless of the biological range. For example, G_{CaCC} = 1.26 pSμm^{-2}, G_{ENaC} in the range of [6.5, 9.5] pSμm^{-2} and G_{CFTR} in the range of [0, 50] pSμm^{-2} give PCL depth ranging from 4.55 to 21.5 μm as shown in Figure 4.4(a). Similar to Fig. 4 (a), as $G_{CFTR} = 0$ pSμm^{-2}, the database between different combinations of G_{ENaC} and G_{CaCC} can be generated for CF cells. For NL cells, once the $G_{CaCC} = f(ATP)$ is created from CF cells, the database between different combinations of G_{CFTR} and G_{ENaC} can be generated.

Second, several sets of experimental data are selected as shown in Table 4.1 and Table 4.2. With the experimental values, such as Data Set 2 in Table 4.2, PCL = 7.9 μm, we can isolate a region in the data base where PCL depth satisfies this value with a deviation of a percentage, e.g. 7.9 ± (5%×7.9) μm as shown in Figure 4.4(b). The selection of the percentage is initially set at 5%, which can be increased up to 20% as needed. Table 4.1 and Table 4.2 show the percentage deviation for the selected range for ENaC.

Third, with the satisfied region for each data set, we create the functions based on two criteria:

- G_{CaCC} must increase with [ATP] increase; G_{ENaC} must decrease with [ATP] and [ADO] increase; G_{CFTR} must increase with [ATP] and [ADO] increase.
- Each function must be bounded with the minimum and maximum boundaries set by experimental data.

With these two criteria, we first choose the linear functions for G_{CaCC} i.e. $G_{CaCC} = a_1$ [ATP] + c_1. Then select the range for G_{ENaC} for CF cell, e.g. G_{CaCC}= 1.26 pSμm^{-2}, with 5% of deviation, G_{ENaC} is in the range of [21, 27.5] pSμm^{-2} as shown in Table 4.1. With the upper and lower limits of G_{ENaC} set for each data set, linear functions i.e. $G_{ENaC} = a_3$ [ATP] + b_3 [ADO] + c_3 are chosen to approximate data between the limits. Similarly for NL cells, as G_{CaCC} is known, linear functions $G_{CFTR} = a_2$ [ATP] + b_2 [ADO] + c_2 are first chosen. Then, select the range for G_{ENaC} for NL cell, as shown in Figure 4.4 (a) The sample data base of PCL depth with different combination of G_{ENaC} and G_{CFTR}. (b) The sample regions satisfy the experimental data with a deviation of 5%, 10% and 15%. The range of G_{ENaC} is determined at G_{CFTR} = 33.1 pSμm^{-2} (see the solid horizontal line). (b), e.g. G_{CFTR} = 33.1 pSμm^{-2}, with 10% of deviation, G_{ENaC} is in the range of [8.7, 10.3] pSμm^{-2}. Finally, linear functions of $G_{ENaC} = a_4$ [ATP] + b_4 [ADO] + c_4 are constructed.

Finally, two other factors should also be taken into considerations. First, there exists contradictory evidence that ENaC might not be inhibited by CFTR channel, so the assumption is that the decrease of ENaC due to [ADO] increase is limited. Second, in the testing data sets, some channels are inhibited or some receptors are blocked as shown in Table 4.4 and Table 4.5. In this case, the corresponding the simulation conditions as shown in Table 4.3 are made to mimic the effects of drugs.

With the information provided in Table 4.1 and Table 4.2, the functions created for the channels are as follows:

The CaCC channel for both NL and CF cells:

$$G_{CaCC} = \begin{cases} 0.7[ATP] & 0 \le [ATP] \le 63.7.2 \\ 3.17e^{-03}[ATP] + 44.4 & 63.7 < [ATP] \le 80529 \\ 300 & [ATP] \ge 80529 \end{cases} \quad (4.1)$$

The ENaC channel for CF cells:

$$G_{ENaC} = \begin{cases} -0.234[ATP] + 22.0 & 0 \le [ATP] \le 63.7 \\ -5.96e^{-05}[ATP] + 7.10 & 63.7 < [ATP] \le 80529 \\ 2.3 & [ATP] \ge 80529 \end{cases} \quad (4.2)$$

The CFTR channel for NL cells:

$$G_{CFTR} = \begin{cases} 0.21[A_1] & 0 \le [A_1] \le 509.4 \\ 4.31e^{-05}[A_1] + 107.3 & 509.4 < [A_1] \le 295434 \\ 120 & [A_1] \ge 295434 \end{cases} \quad (4.3)$$

$$([A_1] = [ATP] + [ADO])$$

The ENaC channel for NL cells:

$$G_{ENaC} = \begin{cases} -0.0045[A_2] + 10.3 & 0 \le [A_2] \le 509.4 \\ -7.34e^{-05}[A_2] + 8.04 & 509.4 < [A_2] \le 80974.7 \\ 2.1 & [A_2] \ge 80974.7 \end{cases} \quad (4.4)$$

$$([A_2] = [ATP] + [ADO]^*, [\text{ADO}] * = \text{ minimum } ([\text{ADO}], 445.7))$$

For the functions of each channel, there are three different ranges as explained below. The first range corresponds to [ATP] in [0, 63.7] nM. 63.7 nM is close to the maximum level of [ATP] release under CCP of 120 cmH_2O. In this range the channels are very sensitive to [ATP] change as reflected in the experimental data. Under this ATP release, PCL depth change is 11.1 ± 3.6 μm in additional to NL under the base level of 7.9 ± 0.9 μm. As a result, we assume that at this point, PCL depth has reached close to the maximum under normal respiratory conditions. The second range corresponds to [ATP] in [63.7, 80529] nM. 80529 nM corresponds to the level of [ATP] 600s after 300 μM ATP addition. During this range PCL depth would reach the recorded maximum of around 19.0 ± 1.9 μm, which is used to set the maximum values for the third range of the channels. As the assumption for ENaC channel that the inhibition from CFTR is limited, the increase of [ADO] has no effect in the second and third ranges. As observed in the experiment with

trypsin and 300 μM ATP in Tarran et al. (2006) as shown in Table 4, PCL depth is initially very high and begins to drop within 60 min, which means that the conductance of ENaC channels are initially tightly inhibited and then return to normal state, i.e. G_{ENaC} increasing from 2.1 pSμm^{-2} (corresponding to the third range) to around 9.5 pSμm^{-2} (corresponding to the base level in the first range). This is consistent with [ATP] rapidly decreasing and contradicted with [ADO] gradually increasing. However, as shown in Table 4 of Tarran et al. (2005), with ATP catalyzed by apyrase, an increase of [ADO] also increases PCL depth, indicating that the ADO might regulate the ENaC channel in the first range but not in the third range. As the objective of this study is to capture the steady state PCL, the time response of each channel is not considered. Table 4.3 lists all the drugs and the brief descriptions of the functions in the experiments and the conditions prescribed in the cell simulations.

4.2 Results

4.2.1 Normal cell simulations

Figure 4.5(a) shows the time histories of PCL depths for NL cells from measurements and model predictions with and without 20 cmH_2O CCP. Figure 4.5(b) shows the same comparison but with the NL cells added with 8-SPT and bumetanide. As there is no time response mechanism in the cell model, the simulations usually drop to steady state conditions faster than the experiments. However, the steady state values agree with experiment results very well. As in the experiment, CCP increases PCL depth and addition of both 8-SPT and bumetanide yields the similar CF-like PCL depth level. Comparing the addition of 8-SPT and bumetanide, both substances weaken the ENaC inhibition resulting in high Na^+ absorption rate; but 8-SPT lowers only CFTR Cl^- secretion rate not CaCC. And because bumetanide lowers Cl^- secretion rates on both channels, addition of 8-SPT results in slightly higher PCL depth than bumetanide in the cell model.

In addition, Table 4.4 shows two additional groups of test cases for NL cells with PCL depth change corresponding to different drugs or/and mechanical forces. The first set focuses on the Cl^- secretion pathway. In these six experiments, additional ATP release is triggered by shear stress. With apyrase added to solution, ATP is metabolized into ADO at a faster rate, so [ADO] increases, which the Cl^- secretion decreases in CaCC is compensated by Cl^- secretion increase in CFTR, so the PCL reaches almost a similar depth as control. However, with addition of 8-SPT instead, CFTR Cl^- secretion decreases without any compensation, so PCL depth decreases almost by half. With both drugs added, overall Cl^- secretion becomes very low, so PCL depth decrease to an almost CF-like level. Then, the experiment is switched to the channel inhibitors, as the [ATP] and [ADO] remain normal, CFTR or both channels are inhibited, PCL depth is either decreased by half or to a CF-like level.

The second set focuses on the Na^+ absorption pathway. First, nystatin is added to the cells under normal condition (no force or additives). It maximizes the Na^+ absorption and reduces PCL depth to even below the CF-like condition. Then, the trypsin or aprotinin is added with either 300 μM ATP or ADO. Aprotinin does not affect NL cells, as NL cells already have tightly inhibited ENaC. With 300 μM ADO added, it is gradually metabolized without much change to the [ATP]. As a result, trypsin with ADO results in both increased CFTR Cl^- secretion and ENaC Na^+ absorption. Overall it exhibits an elevated PCL depth that slowly decreases from 10 min to 60 min. Compared with adding trypsin, PCL depth is greater with aprotinin added on the next set, as ENaC is unaffected while CFTR Cl secretion increases. With 300 μM ATP added, it triggers a spike of Cl^- secretion from both CaCC and CFTR that instantly raises PCL depth to the maximum. As ATP is quickly catalyzed into other metabolites, [ADO] gradually increases, which returns to the conditions similar to those in which ADO is added. The difference between adding trypsin or aprotinin is that adding trypsin activates ENaC, and then PCL depth drops much quickly from 10 min to 60 min. In summary, with both Cl^- secretion and Na^+ absorption are tested

under various experimental conditions, the overall agreement between experimental data and model simulations is very good.

4.2.2 Cystic fibrosis cell simulations

Next, we consider the cell model predictions for CF cells. Figure 4.6(a) shows the time histories of PCL depths for CF cells from measurements and model predictions with and without 20 cmH_2O CCP. Figure 4.6(b) shows the CF cells added with apyrase and bumetanide. Essentially, both experiment and simulation show that addition of bumetanide and apyrase into CF cells has no effect on the steady state values. As for CF cells at the base level, [ATP] is already very low, either further decrease of [ATP] by apyrase or decrease of Cl^- secretion by bumetanide cannot produce any observable effect. However, as shown in the first data set in Table 4.5, with additional [ATP] released under CCP, when adding apyrase or bumetanide, PCL depth is significantly reduced from the one only with CCP, i.e. 11.9±3.4 μm by experiment (or 9.17 μm by cell model prediction). Adding bumetanide might result in higher PCL depth than adding apyrase. This is because apyrase decreases [ATP], which weakens both Cl^- secretion and ENaC inhibition; while bumetanide only decreases Cl^- secretion and the [ATP] is unaffected, so ENaC inhibition is unaffected.

The other two groups of test cases for CF cells are shown in Table 4.5, in which similar to the NL cells, the Cl^- secretion pathway and Na^+ absorption pathway are tested respectively. First, in the Cl^- secretion pathway, adding 8-SPT or CFTR inhibitor has no effect on the CF cells due to the blockage of the pathway. Adding apyrase and CaCC inhibitor reduces PCL depth close to the CF base level, which is 3.9 ± 0.8 μm by experiment and 4.08 μm by cell model prediction. Then, the same tests for Na^+ absorption pathway were performed for CF cells as those for NL cells. In CF cells, adding trypsin has no effect, as the CF cells are already at the maximum Na^+ absorption rate. Adding ADO should have no effect on CF cells. But with aprotinin, ENaC activity is inhibited, so PCL

depth is slightly elevated as compared to those with trypsin added. With ATP added, similar to NL cells, the CF cells experience a rapid raise in PCL depth. And with aprotinin inhibiting ENaC, PCL depth drops slower than the one with trypsin added. Thus, the CF cells also show same behaviors as those observed in experiment.

4.2.3 PCL depth vs. mechanical forces

Button et al. (2013) reported the relationship between the change of PCL depth and the change of [ATP] under CCP in NL cells. Figure 4.7(a) overlays the experimental data with those predicted by both NL and CF cell models. In the test, the increase in ATP release is triggered by increasing CCP as the approach used in Button et al. (2013)'s experiment. It is worth noting that using increasing CSS to increase ATP release would produce the same results shown in Figure 4.7(a). The change of PCL depth of NL cells has an almost linear increase with the change of ATP. On the other hand, the change of PCL depth in the CF cells is quite slow initially for the first 40 nM [ATP] increase and then increases rapidly in the range from the 40 to 60 nM. 60 nM is close to the maximum ATP release that can be triggered by CCP. Although CSS can trigger greater ATP release than this limit, but as the ion-channel conductance model enters the second range, change of PCL depth reaches plateau. Figure 4.7 (b) and (c) show that the absolute PCL depth increases with mechanical forces. NL cells respond rapidly to CCP from 0 to 20 cmH_2O, while CF cells respond gradually to CCP from 0 to 100 cmH_2O. The NL cells respond to CSS steadily from 0.0 to 0.6 $dyne/cm^2$, the CF cells respond slowly to CSS from 0.0 to 0.5 $dyne/cm^2$ and then rapidly from 0.5 to 0.6 $dyne/cm^2$. The maximum increases of PCL depth by ATP release for NL and CF cells are about 15.7 and 14.2 μm, respectively.

As Button et al. (2013) also reported the change of PCL depth with % LMA in the NL cells and the range of [ATP] release at each % LMA level as shown in Figure 4.2 (b), Figures 4.8 (a) and (b) show the model predictions that reproduce their experiment. The range of [ATP] release at each mucus viscosity level measured by Button et al. (2013) is

used to predict the range of PCL depth changes presented as upper and lower limits as shown in Figures 4.8 (a) and (b) for NL and CF cells. Figures 4.8 (c) and (d) also show the increase of the absolute PCL depth with the % LMA. The predicted change of PCL depth agrees with experimental measurements for NL cells. Comparing to NL cells, CF cells do not have enough PCL depth change at low mucus viscosity, but have greater PCL depth change at high mucus viscosity. Nonetheless, the ATP release triggered by cilia strain is modeled as a constant in the cell model as mentioned in the Method section, corresponding to the regular cilia strain found in the NL or CF cells. Thus, PCL depth with response to cilia strain for NL cells is 7.92 μm comparing to 7.68 μm at base level, and for CF cells is 6.35 μm comparing to 4.08 μm at the base level.

4.2.4 PCL depth vs. evaporative flux

Figures 4.9 (a) and (b) show the relationship between the evaporative flux with PCL depth from zero to maximum ATP release for both NL and CF cells. On each curve, the ATP release from mechanical forces is constant, so the conductance of CaCC, CFTR and ENaC are constant as well. PCL depth increases with decreasing evaporative flux. When the evaporative flux condensates on the cells, some of the condensation is absorbed by the cell and some of it goes to the PCL. However, when the condensation flux is large enough to reach the cell's absorption limit, PCL depth will increase infinitely. The red curves marked in both figures show the maximum condensation flux that the cells can absorb and reach steady state at same time, which is called the maximum absorption line. As the ATP release increases, the Cl^- secretion is higher while Na^+ absorption is lower, the cells are more opt to secrete not absorb water. As a result, the absolute value of the maximum condensation flux decreases with increasing ATP release. Two other lines are marked in both figures. One is the optimum PCL depth line, which is at the intersection between the zero evaporative flux line and the zero ATP release curve for the NL cells. The other is the CF-like PCL depth line, which is at the intersection between the zero evaporative flux line

and the zero ATP release curve for the CF cells. Figure 9 (c plots the evaporative flux against the amount of ATP release for these curves. The optimum PCL depth curves show the amount of ATP release needed in order to balance the evaporative flux, and the maximum ATP release that can balance evaporative flux around 0.03 μm/s. The CF-like PCL depth curve shows that if the evaporative flux is greater than 0.12 μm/s, even with the largest ATP release it cannot prevent PCL depth drop below CF-like level.

4.3 Discussion

The construction of ion-channel conduction model mimics the idea of reverse engineering. This approach serves well for the objective of the study: to couple it with a thermo-fluid CFD solver for study of PCL depth change, as the detailed biochemistry reactions within the cells either happen on disparate time scales or remain unclear. Overall, the cell model performs very well for both NL and CF cells, being in good agreement with experimental data. Thus, the proposed ion-channel conductance model captures the trends of theoretical behaviors of the ion channels.

Although there is certain flexibility in choosing the data range for each channel, the proposed channel functions serve the purpose of predicting PCL depth in response to mechanical forces. Moreover, as these functions must satisfy some constrains found in the experimental data, they are expected to predict biological behaviors observed in experiment. For example, the ENaC for NL cells under breathing conditions (i.e. ATP release within 100 nM) ranges from 8 to 10 $pS\mu m^{-2}$, the ENaC channels for CF cells could be from 6 to 20 $pS\mu m^{-2}$. This is consistent with the fact that the ENaC channel is strictly regulated in NL cells, but not in CF cells.

As cell experiments might have unavoidable uncertainties, the agreement of experiment data with model simulation may not necessarily reflect more accurate prediction. For example, even for the NL cell base level, PCL depth could vary from various experiments: Button et al. (2013) measured 7.4 ±0.3 μm, while Tarran et al. (2005)

measured 8.0 ± 1.0 μm. For most of PCL depth measurements the standard error provided by existing experimental studies varies roughly from 10% to 20%. In this study, in both calibration process and testing process, if the standard error is not provided by the original experiment data, we assume an error of 10% of the value. However, any deviation within 20% of the value is considered acceptable as long as the model prediction exhibits the same trend with experimental measurement.

Comparing the NL and CF cells, their ATP releases based on mechanical forces are completely the same, but their responses to the inputs like CCP, CSS and evaporative flux are quite different. For NL cells, we found steady increase of PCL depth with ATP release agreeing with experimental measurement, while for CF cells we found an exponential-like increase of PCL depth with ATP release. As a result, PCL depth-mechanical forces profiles in NL and CF cells are all quite different as shown in Figure 4.7 and Figure 4.8. This is mainly due to the difference in ENaC between NL and CF cells. As shown in the calibration in Table 4.1 and Table 4.2, for PCL depth to reach an optimum depth of 7.0 μm to 8.0 μm, the ENaC has to be less than 10 $pS\mu m^{-2}$, for which CF cells need around 40 to 50 nM ATP release. However, with zero ATP release, ENaC is usually around 20 to 30 $pS\mu m^{-2}$. As there is no data to support or against otherwise, linear data fitting was used to construct the ENaC conductance model. For CF cells, from 0 to 50 nM ATP release, ENaC decreases from 20 to 10 $pS\mu m^{-2}$, while the Na^+ absorption remains much stronger than Cl^- secretion in this range. Consequently, CF cells exhibit very slow increase of PCL depth. However, once ENaC is properly inhibited at 8 to 10 $pS\mu m^{-2}$ range such as in NL cells, PCL depth increases rapidly. Thus, according to the numerical analysis, CF cells could be insensitive to relatively low ATP release (and thus small mechanical forces) because the ATP release is not enough to provide enough inhibition on the ENaC.

The other difference between NL and CF cell models lies in their responses to evaporative flux. The curves in Figure 4.9 (a) for NL cells are more compact than those of CF cells in Figure 4.9 (b), which is also reflected in Figure 4.9 (c) as the slopes of CF

curves are much steeper. For example, each point on the optimum PCL curves shows the amount evaporative flux that the cell could balance with the given amount of ATP release while maintaining optimum PCL depth. So steeper slope means that ATP release triggered by mechanical forces are more effective on CF cells in terms of balancing evaporative flux in PCL depth regulation. In NL cells, the increase in ATP release results in little increase in the evaporative flux that it could balance. However, from 60 nM to maximum, ATP release curves in NL and CF are almost the same, indicating that with ATP release greater than 60 nM, not only evaporative flux becomes the only determinant of PCL depth, but also NL and CF cell models predict almost the same magnitude of PCL depth. Thus, the evaporative flux is the dominant factor influencing PCL depth, especially in NL cells.

The limitation of this model is two-fold. First, as the time mechanism is not considered in the ion channel conduction model. The time response depends entirely on ATP model and FSM model. Generally, the time response of cell model follows the trend observed in the experiments, but there exists some deviations of magnitude in prediction from the measurements. However, the deviation in time response is acceptable as the steady state PCL is not affected. Second, the construction of ion-channel conduction model is based on the existing available experimental data, which might not provide the full spectrum of the ATP release vs PCL depth relationship. For example, the first range is determined by [ATP] = 63.7 nM, corresponding to maximum CCP based on the available data (Button et al. 2013). However, ATP release by CSS goes beyond this upper limit for the first range. Nonetheless, the method of constructing ion-conduction channel functions works for a larger data set. It could potentially be used for a variety of steady state channel-regulatory problems for epithelial cells. For future work, the time mechanism could be added to the ion-conduction channel model, so that the cell model could capture the transient behavior. The % LMA could be a function of PCL depth, hence cilia strain could be included in the model as a function of PCL depth.

Table 4.1 The experimental data used to calibrate CaCC and ENaC channels in CF cells.

Data Set[a]	Conditions	Parameters[b]	PCL depth[c]	CaCC Value	%	ENaC Range
1	Base with apyrase	[ATP] = 0 nM	3.7 µm	0	6	[27.5,30]
2	Base	[ATP] = 1.2 ± 0.2 nM; ([ATP] = 1.8 nM)	3.9 ± 0.8 µm	1.26	5	[21,27.5]
3	0.5 dynes/cm^2 cyclic shear stress	[ATP] = 41.3 ± 8.3 nM; ([ATP] = 49.9 nM)	8.0 ± 1.4 µm	34.9	8	[8.7, 9.9]
4	20 cmH_20 cyclic compressive force	[ATP] = 54.0 ± 8.8 nM; ([ATP] = 57.2 nM)	11.9 ± 3.9 µm	40.04	5	[7.3,7.6]
5	Trypsin with 300 µM ATP	[ATP] = 300 µM; ([ATP] = 80529 nM)	19.0 ± 1.9 µm (t = 600s)	300	10	[1,2.3]

a. 1, 3:Tarran et al. (2005); 2, 4: Button, Picher, and Boucher (2007); 5: Tarran et al. (2006)

b. The values inside parenthesis are the actual value predicted by the ATP model

c. PCL depth uses the steady state values (more than 24 hours) unless otherwise noted.

Table 4.2 The experimental data used to calibrate CFTR and ENaC channels in NL cells.

Data Set[a]	Conditions	Parameters	PCL Depth[b]	CFTR Value	%	ENaC Range
1	Base with 8-SPT	[ATP] = 1.8 nM; [ADO] = 0 nM	3.7 μm	0.38	20	[11.5,30]
2	Base	[ATP] = 1.8 nM; [ADO] = 155.5 nM	7.9±0.9 μm	33.1	10	[8.7,10.3]
3	0.5 dynes/cm^2 cyclic shear stress	[ATP] = 49.9 nM; [ADO] = 370.5 nM	13.2±1.1 μm	88.5	5	[8.3,8.6]
4	20 cmH_2O cyclic compressive forces	[ATP] = 57.2 nM; [ADO] = 409.5 nM	13.2±1.7 μm	98.3	5	[8.1,8.3]
5	Aprotinin with 300 μM ADO	[ATP] = 1.8 nM; [ADO] = 295433 nM	14.1+1.9 μm (t = 600 s)	120	-	8.28*
6	Aprotinin with 300 μM ATP	[ATP] = 80529 nM; [ADO] = 6613 nM	18.5+2.2 μm (t = 600 s)	107.5*	5	[2,2.1]

a. 1, 3:Tarran et al. (2005); 2, 4: Button, Picher, and Boucher (2007); 5, 6: Tarran et al. (2006)

b. The values inside parenthesis are the actual value predicted by the ATP model

c. PCL depth uses the steady state values (more than 24 hours) unless otherwise noted.

Table 4.3 Drug information

Drugs	Description	Simulation Conditions
LMA	Low-melting point agarose, with different (%) concentration mimics mucus viscosity	0.15% for NL cells, 0.3 % For CF cells
Apyrase	An enzyme that catalyzes ATP into AMP rapidly	ATP*0.05 , ADO*1.5
Bumetanide	An inhibitor of Cl secretion (affect both CaCC and CFTR)	The Cl^- secretion is only 0.1% of the normal values
8-SPT	8 (p-sulfophenyl) theophylline; an ADO receptor antagonist	Only 0.1% of ADO binds to A_{2b} receptor and raises the cAMP level
Nystatin	An ionophore that significantly increases Na absorption rate through membrane, bypassing ENaC	G_{ENaC} = 40 pSμm^{-2}; a large conductance to mimic the permeabilized membrane
Aprotinin	ENaC inhibiting protein, decrease Na absorption	No effect to NL cells; G_{ENaC}*coeff., coeff. less than 1.0
Trypsin	ENaC activating protein, increase Na absorption	No effect to CF cells; G_{ENaC}*coeff., coeff. greater than 1.0
DIDS	4,4 -diisothiocyanostilbene-2,2 -disulfonic acid; CaCC antagonist	G_{CaCC} conductance is only 0.1% of the normal values
$CFTR_{inh172}$	CFTR antagonist	G_{CFTR} conductance is only 0.1% of the normal values

Table 4.4 Test cases used to assess the prediction of NL cell response by the current cell model.

Data Set	Experiment Condition	Simulation Condition	Exp. Data	Prediction
(1) Tarran et al. (2005)	(a) 0.5 dynes/cm^2 cyclic shear stress	NL (control)	16.3±1.7	13.53
	(a) + apyrase	ATP*0.05, ADO*1.5	15.5±2.7	13.06
	(a) + 8-SPT	ADO*0.001	7.5±1.0	7.69
	(a) + apyrase+8-SPT	ATP*0.001; ADO*0.001	4.6±0.7	4.69
	(a) + CFTR_inh172	G_{CFTR}*0.001	8.6±1.2	9.13
	(a) + DIDS + CFTR_inh172	G_{CaCC}*0.001; G_{CFTR}* 0.001	5.5±1.4	4.44
(2) Tarran et al. (2006)	Nystatin	G_{ENaC} = 40	3.7±0.1	3.98
	(a) Trypsin with 300 µM ADO (10 min)	G_{ENaC}*1.3	8.6±0.8	9.02
	(a) (60 min)	G_{ENaC}*1.3	8.4±1.0	8.03
	(b) Aprotinin with 300 µM ADO (10 min)	NL	14.1±1.9	11.19
	(b) (60 min)	NL	11.6±1.4	12.84
	(c) Trypsin with 300 µM ATP (10 min)	G_{ENaC}*2.3	16.7±0.8	17.84
	(c) (60 min)	G_{ENaC}*2.3	10.5±1.0	9.34
	(d) Aprotinin with 300 µM ATP (10 min)	NL	18.5±2.2	18.80
	(d) (60 min)	NL	17.2±1.3	18.43

Table 4.5 Test cases used to assess the prediction of CF cell response by the current cell model.

Data Set	Experiment Condition	Simulation Condition	Exp. Data	Model Sim.
(1) Button, Picher, and Boucher (2007)	(a) 20 cmH2O compressive pressure+ apyrase	ATP*0.05	4.8±0.2	4.12
	(a) + bumetanide	G_{CaCC}*0.001	5.8±0.7	4.41
(2) Tarran et al. (2005)	(a) 0.5 dynes/cm2 cyclic shear stress	NL (control)	8.2±0.9	7.13
	(a) + apyrase	ATP *0.05	4.7±1.0	4.11
	(a) + 8-SPT	NL	7.1±0.7	7.13
	(a) + CFTR_inh172	NL same as (a)	9.3±1.7	7.13
	(a) + DIDS + CFTR_inh172	G_{CaCC}*0.001	4.1±0.1	4.31
(3) Tarran et al. (2006)	Nystatin	G_{ENaC}=30	3.7±0.15	3.84
	(a) Trypsin with 300 µM ADO (10 min)	NL	5.5±0.8	4.11
	(a) (60 min)	NL	3.7±1.0	4.08
	(b) Aprotinin with 300 µM ADO (10 min)	G_{ENaC}*0.1	7.1±1.3	6.17
	(b) (60 min)	G_{ENaC}*0.1	6.4±1.3	5.93
	(c) Trypsin with 300 µM ATP (10 min)	NL	19±1.9	17.83
	(c) (60 min)	NL	4.5±0.4	5.81
	(d) Aprotinin with 300 µM ATP (10 min)	G_{ENaC}*0.85	18.2±1.7	18.33
	(d) (60 min)	G_{ENaC}*0.85	12.2±2.3	9.91

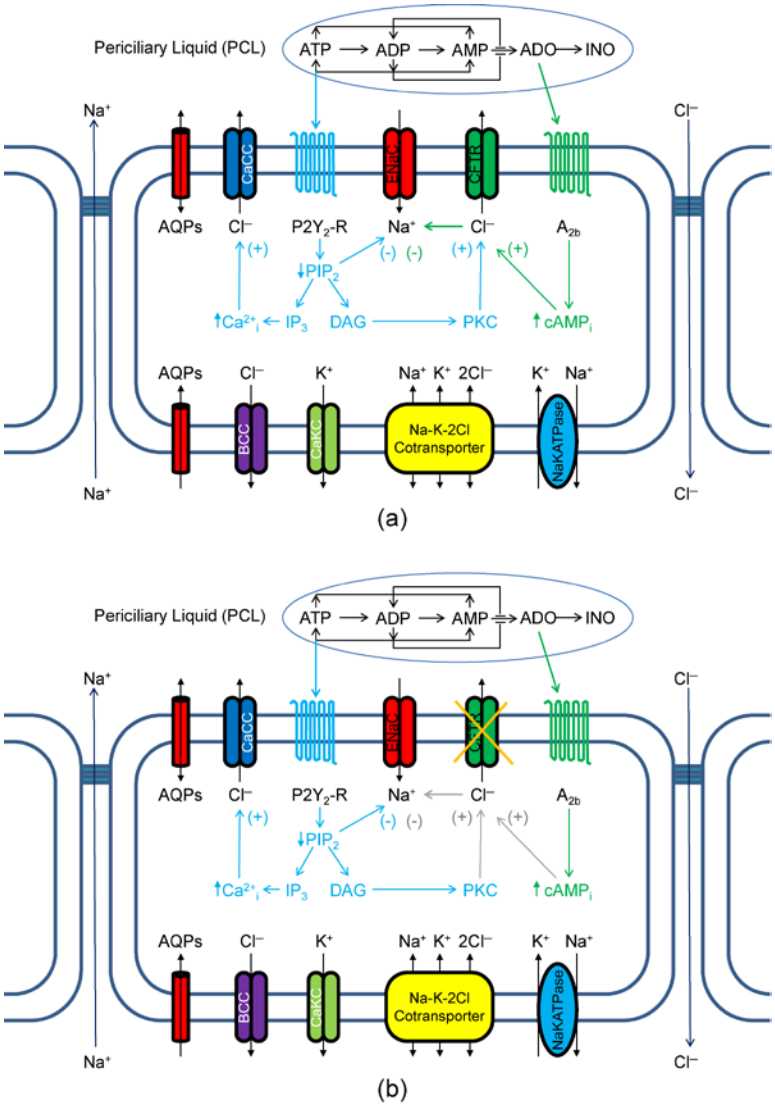

Figure 4.1 The schematic view of the ATP and ADO regulated ion channels for the (a) normal cell and (b) CF cell (Zuo 2007).

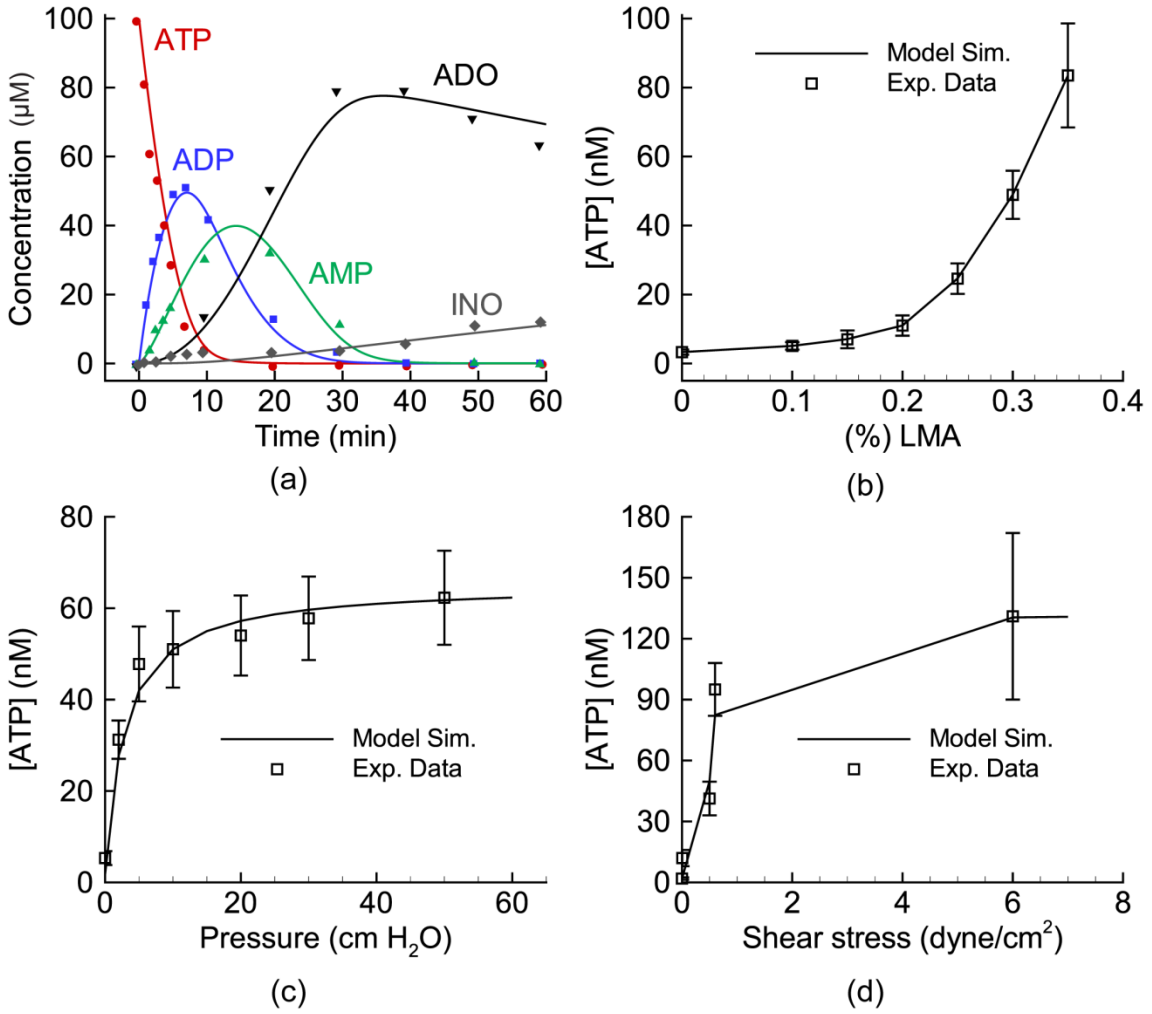

Figure 4.2 (a) The time response of the ATP model with 100 μM [ATP] addition, as in Zuo et al. (2008). (b) The ATP released due to cilial strain with different mucus viscosity (% LMA), as in Button et al. (2013). (c) The ATP released due to cyclic compressive pressure, as in Button, Picher, and Boucher (2007). (d) The ATP released due to cyclic shear stress, as in Tarran et al. (2005).

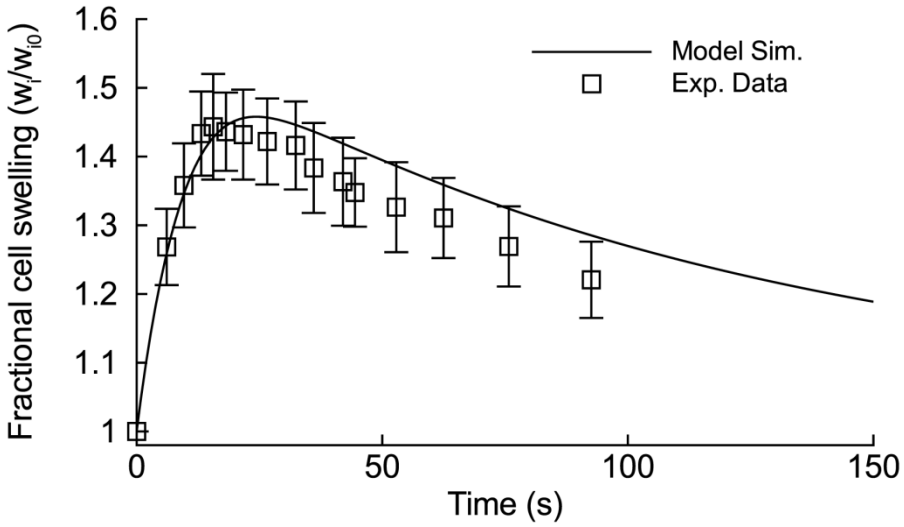

Figure 4.3 The time response of the fluid secretion model from Warren, Crampin, and Tawhai (2010) to 33% hypotonic challenge comparing with experimental data from Okada et al. (2006)

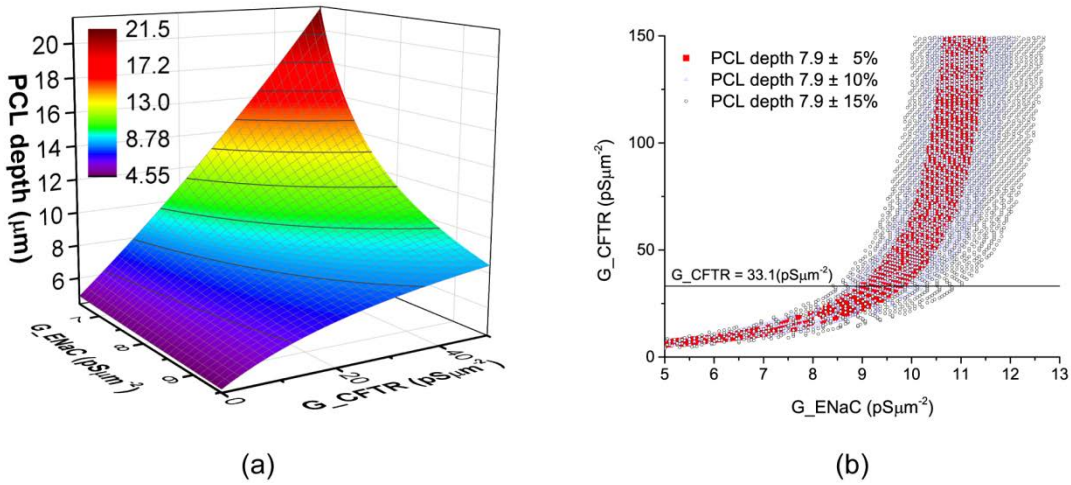

Figure 4.4 (a) The sample data base of PCL depth with different combination of G_{ENaC} and G_{CFTR}. (b) The sample regions satisfy the experimental data with a deviation of 5%, 10% and 15%. The range of G_{ENaC} is determined at G_{CFTR} = 33.1 pSμm^{-2} (see the solid horizontal line).

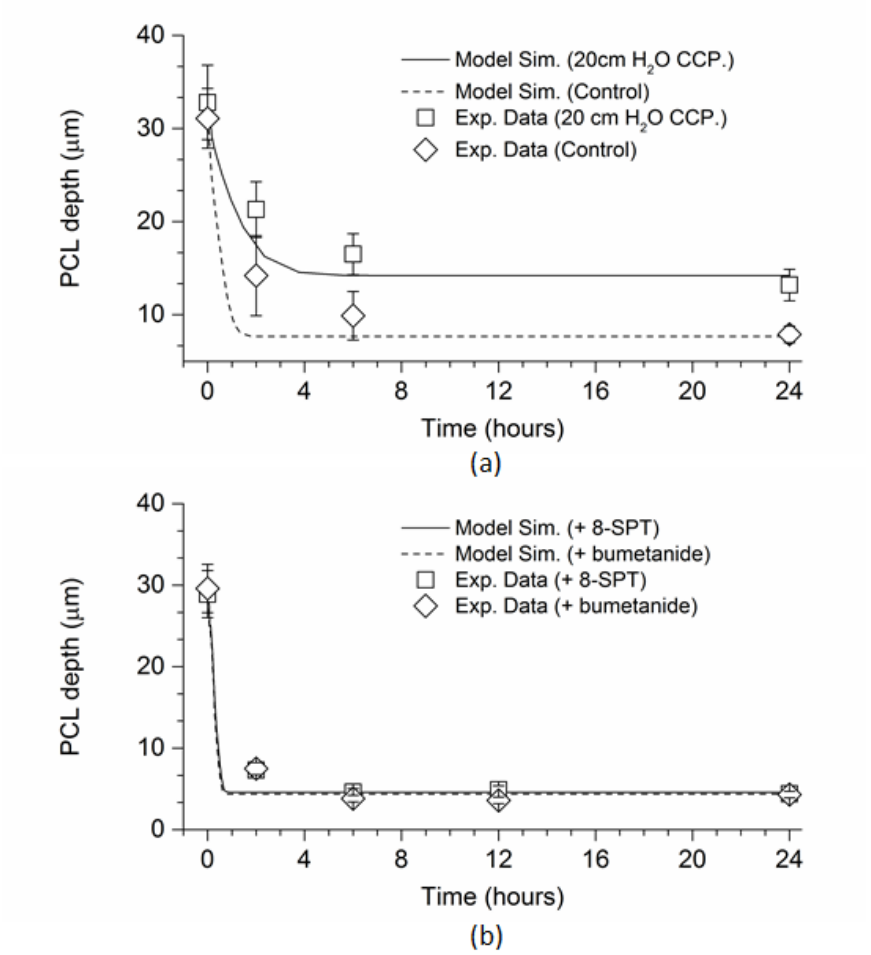

Figure 4.5 (a) The time histories of predicted NL cell responses to addition of 30 µl of PBS with and without 20 cmH_2O compressive pressure in comparison with the experimental data of Button, Picher, and Boucher (2007). (b) The time histories of predicted NL cell responses to addition of 30 µl of PBS with 8-SPT in comparison with the experimental data of Tarran et al. (2005) and to addition of bumetanide in comparison with the experimental data of Tarran et al. (2006).

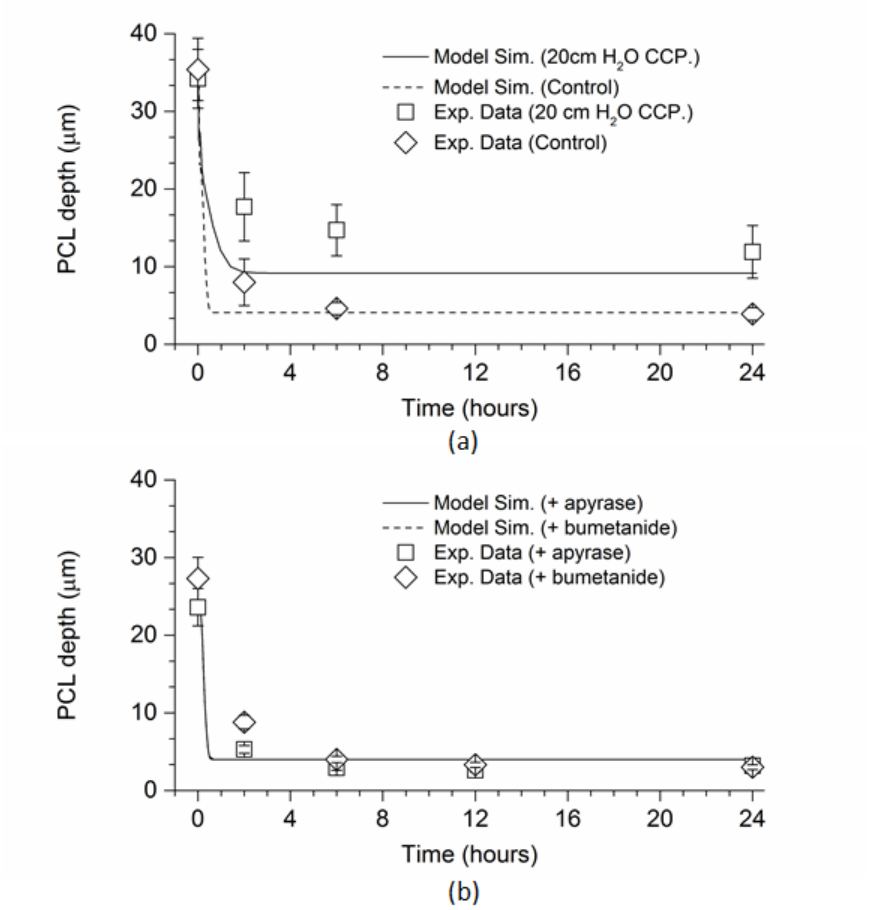

Figure 4.6 (a) The time histories of predicted CF cell responses to addition of 30 μl of PBS with and without 20 cmH_2O compressive pressure in comparison with the experimental data of Button, Picher, and Boucher (2007). (b) The time histories of predicted CF cell responses to addition of apyrase in comparison with the experimental data of Tarran et al. (2005) and to addition of bumetanide in comparison with the experimental data of Tarran et al. (2006).

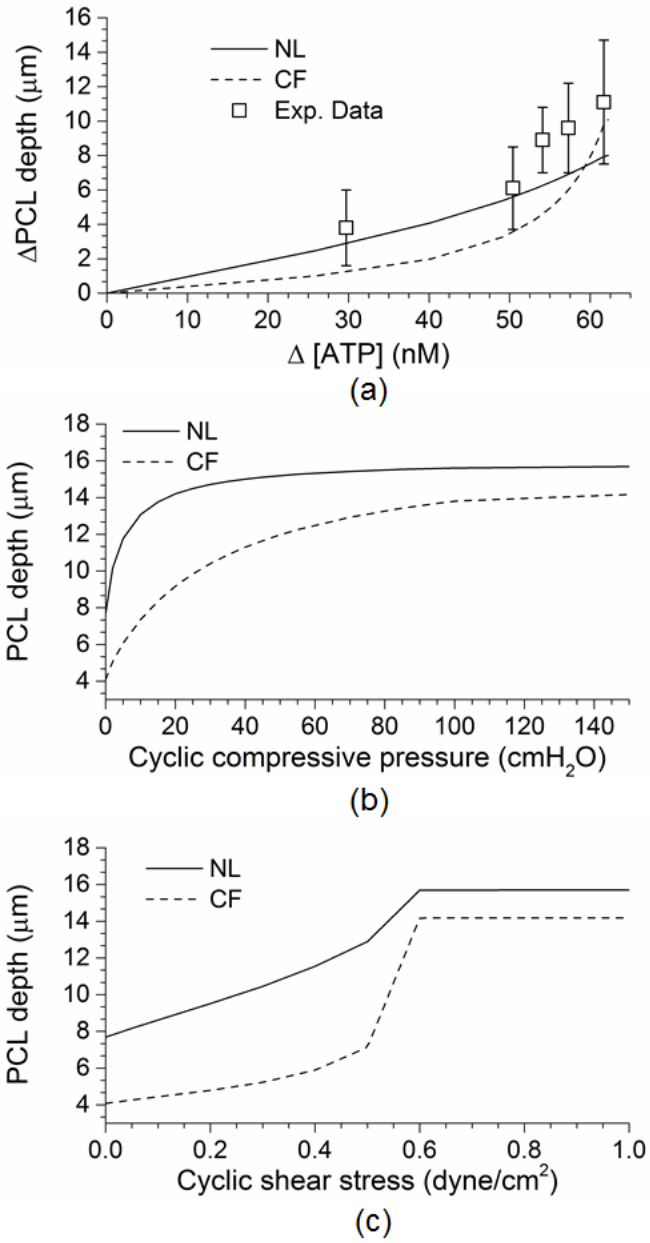

Figure 4.7 (a) The relationship between the increase of [ATP] triggered by increasing cyclic compressive pressure and the increase of PCL depth for CF and NL cells comparing with experimental data of Button et al. (2013). (b) The relationship between the absolute PCL depth and CCP in NL and CF cells. (c) The relationship between the absolute PCL depth and CSS in NL and CF cells.

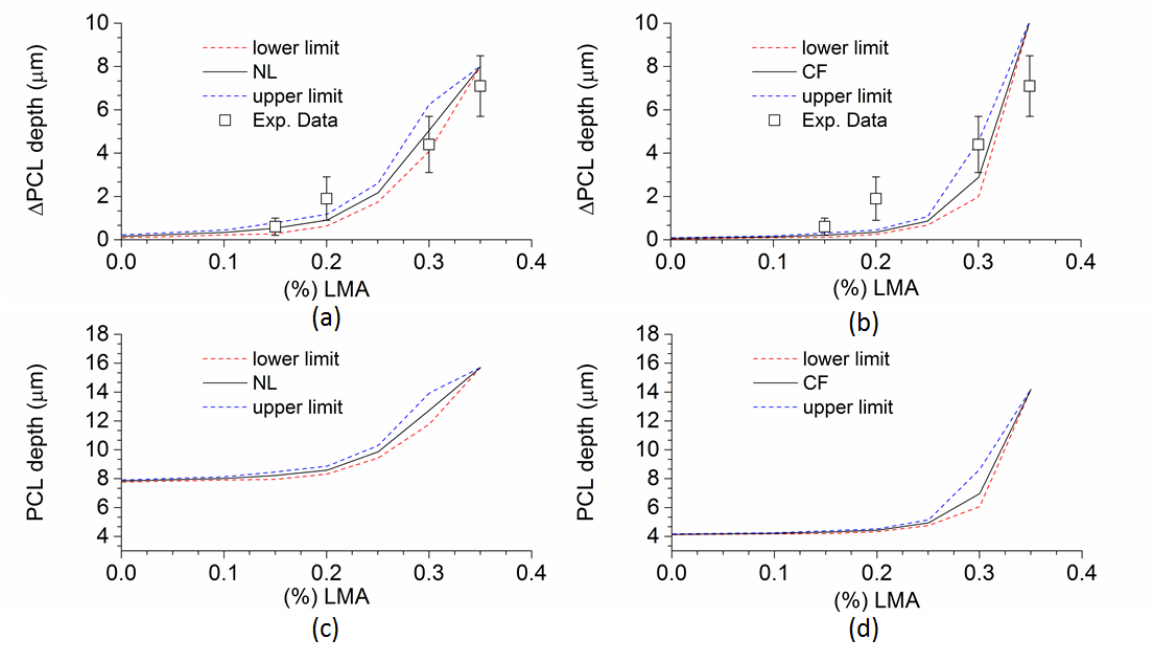

Figure 4.8 The relationship between the increase of mucus viscosity and the increase of PCL depth NL cells comparing with experimental data from Button et al. (2013) in (a) NL cells and (b) CF cells. Then, the relationship between the mucus viscosity and absolute PCL depth in (c) NL cells and (d) CF cells. The upper and lower limit corresponding to the upper and lower limits of ATP release at each LMA concentration.

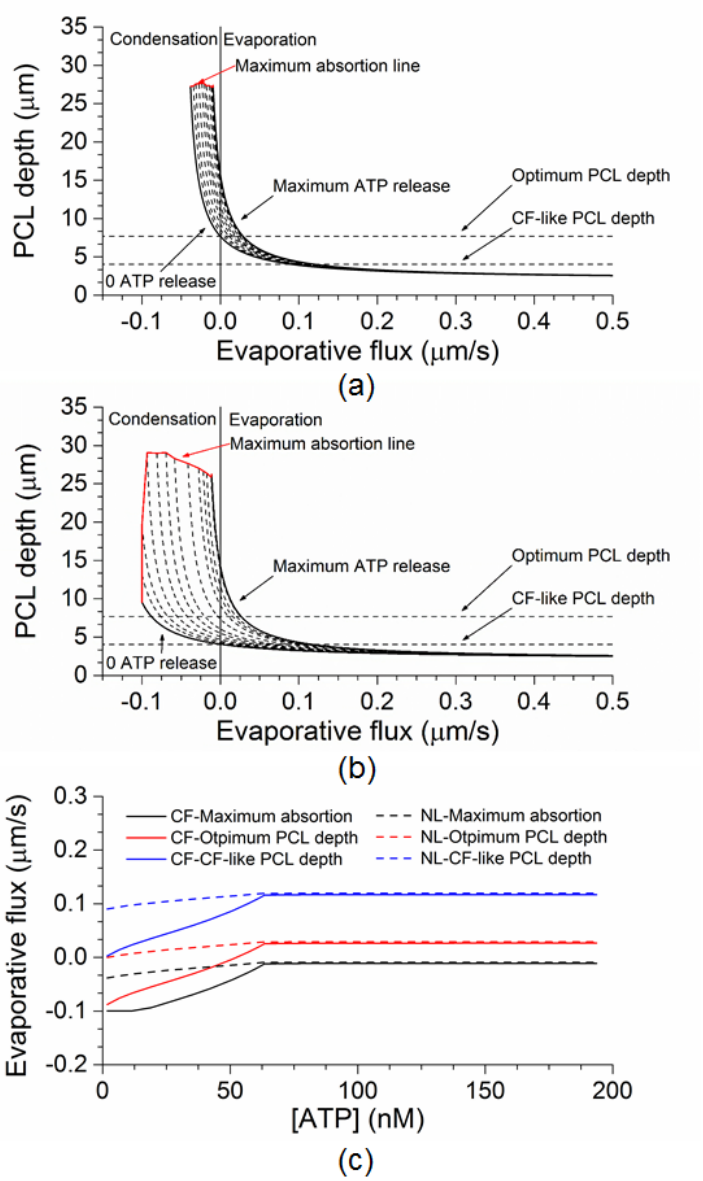

Figure 4.9 The relationship between evaporative flux and PCL depth with ATP release from 0 to maximum under breathing condition for (a) NL cells and (b) CF cells. Six curves are extracted from (a) and (b) corresponding to the maximum absorption line, optimum PCL depth and CF-like PCL depth are plotted in (c), where evaporative flux is plotted against the amount of ATP release.

CHAPTER 5

PERICILIARY LIQUID DEPTH PREDICTION

In previous chapters, a thermo-fluid CFD model and an epithelial cell model have been separately developed and validated. In this chapter, the thermo-fluid CFD model which creates a realistic airway environment is integrated with epithelial cell model, whose responses to mechanical forces are consistent with the experimental measurements by Button, Picher, and Boucher (2007) and Button et al. (2013) and Tarran et al. (2005). The integrated model provides a better picture of PCL depth regulation in both NL and CF patients.

5.1 Method

5.1.1 Geometry modeling

3 NL Subjects and 3 CF subjects were selected for this study. The average age, BMI, PFT results, and lobar ventilation distributions of the selected NL subjects are similar to those of a NL group. As a result, they could be considered as representatives for the NL group. Likewise, the selected CF subjects are considered as representatives for a CF group. With MDCT images at TLC of these subjects, the 1D skeletons are generated, following the entire 1D trees generated with the volume filling method (Tawhai et al. 2004). For 3D geometries, the segments of cylinders are generated based on the CT-based 1D skeleton and then the surfaces of cylinders are fit to the CT image surfaces. For 3D branches beyond the CT-image, they are modeled as cylinders that have consistent diameters and orientations with the 1D tree. Medium size meshes are used (see the mesh sensitivity test presented in Chapter 2). Near the airway wall regions the CFD mesh is refined to better capture the gradient-based variables, such as evaporative flux and shear stress. The methods for the generation of 1D and 3D geometries as well as the meshes for 3D

geometries are similar to the 6-path model used in Chapter 3 (see Chapter 3 for more detail).

5.1.2 Simulation procedures and parameters

For each case, velocity boundary condition is first determined by image registration technique (Yin et al. 2010). The lobar ventilations for the 6 subjects are shown in Table 1. The average lobar ventilation for NL and CF subjects are computed. The P values shows only the RUL are statistically different for the two groups, though the statistical analysis is not rigorous as it is based on the three subjects in each group. The flow rate distribution in the 1D tree is also determined during the image registration process (Yin et al. 2010). 1D CFD is simulated to get the quasi-steady state temperature and humidity distributions. As in Chapter 2, 1D solutions are provided to 3D models as boundary and initial conditions (See Figure 2.2 for more detail). In addition, in this study 1D solutions are also used to determine the 3D ending branches. As 3D models cannot solve the entire airway tree, the 3D ending branches are those where air temperature (predicted by 1D) reaches 35.5 °C and 100% RH at peak inspiration. This method is better than using distances or generation criteria, just like ISBs that vary in different paths depending on factors such as ventilations, diameters, as shown in Figure 2.5. Using generation or distances causes imbalance between different regions. For example, some regions might contain air that reaches 36 °C, while other regions might terminate at where air only reaches 34 °C. This will cause an unfair comparison between different lobes in regards to water loss rate. With all the information provided by 1D solutions, the 3D thermos-fluid CFD is solved as in Chapter 2. Then, the average evaporative flux J_{evap}, cyclic shear stress change ΔCSS, cyclic compressive pressure change ΔCCP during respiration are predicted at every boundary node. Based on the three inputs at each boundary node, different combinations of information could be passed to the cell model, which is distributed at every boundary node: PCLa with only J_{evap};

PCLb with J_{evap} and ΔCSS; PCLc with J_{evap} and ΔCPP; PCLd with J_{evap} , ΔCCP and ΔCSS; and PCLe with J_{evap} , ΔCCP, ΔCSS and cilia strain.

Sinusoidal waveforms of temperature and humidity are provided at the inlet during inspiration which resembles breathing in room air (T = 26.7 °C and 34.7 % RH) at oral cavity. Velocity boundary provided at the inlet with synthetic turbulent perturbation is the same one as used in the 6-path model case in Chapter 3. To investigate PCL depth for both CF and NL under their regular breathing condition (Browning, D'Alonzo, and Tobin 1990) for CF, the respiratory rate is 10.1 L/min minute ventilation, 2.4 s period with 0.97 s inspiratory period. For NL, the respiratory rate is 6.56 L/min minute ventilation, 3.75 s period with 1.54 s inspiratory period. In addition to the 6 subjects simulated at their regular breathing condition, two controlled simulations were performed: the pseudo NL case, which the subject NL01 was simulated at CF conditions (including respiratory rate and cell model); and the pseudo CF case, which the subject CF01 was simulated at NL conditions. The controlled simulations are designed to study whether the structural differences between NL and CF would influence PCL depth distribution.

As the 3D ending branch is determined by the temperature boundaries at 35.5 °C for both CF and NL. For CF subjects, the minute ventilation is higher, so their ending branches go further down into the 9^{th} or 10^{th} generation, while the NL ending branches are generally at the 7^{th} or 8^{th} generation. Figure 5.1 shows the diameter distributions in each subjects with the order of generations, as well as the average diameters in each generation for NL vs those in CF. As shown in Figure 5.1, the CF subjects have greater average airway diameters than NL subjects from the 4^{th} generation.

5.1.3 The deformable airway test

The deformable airway test compares the effect of deformation on PCL depth change in a NL subject at 15 L/min minute ventilation with 2 s period. One rigid case and one deformable case are simulated. The deformable case changes from FRC to around 60%

vital capacity and from end expiration to end inspiration. The rigid case uses the lung size at the end inspiration. Room air condition (T = 26.7 °C and 34.7 % RH) is provided at oral cavity. Other simulation parameters for fluid were set up as in Yin et al. (2013) and simulation parameters for thermodynamic were set up as in Chapter 2. Same NL subject and mesh were employed as in Yin et al. (2013).

5.2 Result

5.2.1 PCL depth distribution

Figure 5.2 shows PCLe depth distributions for all the CF and NL subjects under their regular breathing conditions. The general trend for CF and NL does not exhibit significant differences. PCL depth generally increases as it goes deeper into the airways. PCL depth is generally lower at the inner surfaces of bifurcations and higher at the outer surfaces of bifurcations, which resembles the water loss rate distributions shown in Chapter 3. To better quantify the regional differences between PCL depths in CF and NL, the values are studied by generation and by lobe as in Chapter 3 for the regional evaporative water loss.

5.2.2 PCL depth distribution by lobes

Figure 5.3 shows the average ΔCSS, ΔCCP and water loss rate in every lobes. As the CF breathing condition has much higher minute ventilation, all three variables are higher in CF in each lobe. The standard deviation at RUL is large in CF, which coincides with low P-value in Table 5.1. The individual effect of these three variables is evaluated in Figure 5.4. Figure 5.4 (a) shows that if only water loss rate is accounted, PCL depth in each lobe remains mostly at 3 μm in CF and 5 μm in NL. With these amounts of water loss rate, Figure 5.4 (b) shows PCL depth when ΔCSS alone is accounted, which the average PCL depth has increased to 5.5 to 6.0 range in CF with an average increase of about 64 %. In NL, the average PCL depth has increased to 6.0 to 7.0 range in NL, with about 27%

increase. Figure 5.4(c) shows PCL depth when ΔCCP alone is accounted, which the average PCL depth has about 5.8 % increase in CF, and 3.0 % increase in NL. Figure 5.4 (d) shows PCL depth that when ΔCSS and ΔCCP are both accounted, PCL depth has an additional 1.2 % increase in CF and 0.37 % increase in NL comparing to PCL depth with only ΔCSS. In Figure 5.4 (e), when CS is added, in CF cells the average increase is 6.1 % and in NL cells the average increase is 0.31 %. Overall, CSS is responsible for 84% of PCL depth increase in CF and 97% of PCL depth increase in NL. Comparing each lobe, both CF and NL have the highest PCL depth on the upper lobes, which is the exact opposite of water loss rate distribution in Figure 5.3 (a), which is further discussed in *Discussion* section.

5.2.3 PCL depth distribution by generation

Similar to Figure 5.3 and Figure 5.4, Figure 5.5 shows the water loss rate, ΔCSS and ΔCCP by generation and Figure 5.6 shows the resulting PCL depths with different inputs. The results show that the water loss rate first increases then decreases, which is consistent with PCLa that slightly decreases and then increases with generation, especially in NL. PCLa shows without any force inputs most of PCL depth in NL stays at 5 to 5.5 μm range in all generations and PCL depth in CF is most at 3.5 μm. ΔCCP and ΔCSS generally increase with generation in both CF and NL. In NL, PCLb, PCLd and PCLe increase with generation from around 5.7 to 7.2 μm, while PCLc increases from 5.0 to 5.7 μm. In CF, both PCLb and PCLd increase from 5.0 to 5.5 μm, while PCLc increases from 3.5 to 3.7 μm. PCLe increases from 5.4 to 6.15 μm. For NL cells, the shear stress is the only dominant force, while for CF cells the cilia strain also contributes to the increase of PCL depth. Generally speaking, the increase of PCL depth with generation is attributable to the increase of ΔCSS with generation and the water loss rate decreases from the 3rd generation.

5.2.4 Pseudo normal vs. average NL

Figure 5.7 shows the subject CF01 with NL conditions (pseudo NL) comparing with average NL cases. The water loss rate, ΔCSS and ΔCCP of the pseudo NL are smaller than those of the NL subjects in almost every lobe. For PCLe depth, the pseudo NL has higher PCL depth than average NL subjects. As the average diameters are greater from 4^{th} to 7^{th} generation, the water loss rate also drops from 4^{th} generation to below NL average. Consistently, both ΔCCP and ΔCSS are mostly below normal average, especially from the 4^{th} to 7^{th} generation. PCLe shows almost completely the same average depth up to 5^{th} generation and only slightly higher in 6^{th} and 7^{th} generation. Thus, if this CF subject has the same respiratory rate and NL cell functions, it will exhibit exactly the same or slightly greater PCL depth distribution as other NL subjects.

5.2.5 Pseudo CF vs. average CF

Figure 5.8 shows the subject NL01 with CF conditions (pseudo CF) comparing with average CF cases. The water loss rate, ΔCSS and ΔCCP of the pseudo CF are greater than the NL subjects in almost every lobe. As a result, PCLe depth for this pseudo CF is lower than the average value of the CF subjects. Same as in each generation, PCLe depth is lower in the pseudo NL case, particularly in the 4^{th} to 7^{th} generation. Although the ΔCSS and ΔCCP are much greater from the 4^{th} to 7^{th} generation in pseudo NL, the water loss rate is also higher in these generations. Thus, this NL subjects has the same respiratory rate and CF cell functions, it will exhibit much lower PCL depth distribution than other CF subjects.

5.2.6 Deformable airway vs. rigid airway

Figure 5.9 shows the deformable case vs rigid case at 15 L/min. The four cases show that the ΔCCP values are much greater in deformable cases than those in rigid case. The difference between ΔCCP in deformable and rigid cases increases with the minute ventilation or wherever the constricted airway presents. For example, one particular constricted airway presents at the 7^{th} generation in RLL, and its ΔCCP in deformable cases

are much higher than the corresponding rigid cases. The ΔCSS is also higher in deformable cases. However, the water loss rate did not change significantly between the rigid and deformable cases. The trends of these three variables in the rigid and deformable cases are also similar. As a result, the distributions of PCLe depth are almost the same for the rigid and deformable cases. In particular, PCLe depth generally follows the opposite trends of water loss rate. In Figure 5.10, the distributions of PCLe depth are predicted using CF cells to compare with those using NL cells. PCL depth predicted by CF cells are generally a little lower than predicted by NL cells. But little difference is observed between the rigid and deformable case.

5.3 Discussion

5.3.1 Dominant factors in PCL homeostasis

PCLe depth distribution is mostly determined by the local water loss. As shown from the results, PCLe depth distributions mostly exhibit opposite trends of water loss rate distributions. For example, the lower lobes are most vulnerable to water loss, so PCL depths predicted in lower lobes are much lower in both NL and CF. When flow rate increases, though water loss rate, ΔCSS and ΔCCP all increases, PCLe depth is likely to decrease. In other words, the change of PCLe depth is more sensitive to the change of water loss rate than the change of mechanical forces. In the three types of mechanical forces, shear stress is the dominant factor, as most of the airways have ΔCSS consistent with the sensitive range of ATP releases in response to ΔCSS. However, ΔCCP in airways is far below the sensitive range, which does not help to raise PCL depth level. The cilia strain is more effective in CF than in NL. However, all the result shows that fluid secretion triggered by mechanical forces cannot balance the water loss, as PCL depth are mostly below the optimum depth. This suggests that there might exist other mechanisms involved in fluid replenishment.

5.3.2 The differences between NL and CF

Both PCL depths in NL and CF almost reach 6 to 7 μm. However, the reasons that they reach this level are different. PCL regulation via mechanical forces is more effective in restoring water losses in CF than in NL, as they increase PCL depth in CF twice as much as they do in NL. In NL subjects, as the minute ventilation is smaller, PCL depth decreases less, but water secretion triggered by mechanical forces is also less. On the contrary, in CF subjects as the minute ventilation is greater, PCL depth is very low, but water secretion triggered by mechanical forces is also greater. As a result, both PCL depths in NL and CF reach almost the same level.

The structural difference between NL and CF subjects is that NL subjects have narrower airway diameters in 4^{th} to 7^{th} generation. As comparing the pseudo NL with average NL, average NL loss more water from 4^{th} to 7^{th} generation, with greater diameter the pseudo NL has higher PCL depth in these generations. As comparing the pseudo CF with average CF, the pseudo CF loses more water from 4^{th} to 7^{th} generation, though mechanical forces are higher and the CF cell model is more sensitive to mechanical forces, it does not help restore PCL depth as the average CF subjects. However, with narrower airway diameters air saturation could be much faster, which might suggest less water loss in the downstream in NL than that in CF. So the greater airway diameters in CF could potentially cause more cold air to propagate downstream. But it causes less regional water loss, and with the regulation of mechanical forces PCL can almost maintain at optimal depth. If their diameters are smaller, the airway water loss rate might exceed the maximum fluid secretion rate that the mechanical forces can provide, then PCL depth cannot keep at close-to-optimum depth, such as the pseudo CF case. For NL airways, the smaller diameter elevates water loss rate, but meanwhile the respiratory rate is low for NL subjects, so the resulting evaporative water loss is mild enough that PCL depth can still remain at close to optimum. This suggests that the greater diameter for CF might help decreasing water loss rate, keep PCL depth at close-to-optimum level.

5.3.3 Effect of airway deformation

The results of deformable versus rigid cases have shown that the deformation might have little effect on PCL depth. Theoretically deformation could enhance the mass and heat transfer in radial directions, but it works the same way for both inspiration and expiration, the water loss might not change much from the rigid case. Or it is possible that the deformation in this study (corresponding to a tidal volume of 500 ml) is not large enough to show a significant difference. However, the change of mechanical forces is quite different for the rigid and deformable cases, especially inside constricted airways. However, the differences of mechanical forces do not result in PCLe depth differences, because almost everywhere the ΔCSS is large enough to trigger the maximum ATP release that the cell model could provide, at which the CF cell works almost like NL cell. Therefore, the test results show little differences in PCLe depth, because the deformation might be too small to result in significant differences in water loss rate and the mechanical forces for all cases have almost reached maximum ATP release to cause any difference, which is the same case for CF cells.

5.5.4 Limitation

The change of shear stress and the change of compressive pressure force are predicted at the interface between ASL and lumen. However, the shear stress acts on the ASL and lumen interface might not be at the same magnitude as the shear stress acts on the epithelial cells, namely, the mucus layer and PCL layer might act as buffers, such as Button et al. (2012)'s spring models of the mucus layer and PCL layer, the actual pressure force acts on the cell only a portion of the pressure from airflow. As indicated in this study the cell has different responses to the different levels of forces, the buffering effect from the ASL layer might affect PCL depth prediction.

The other limitation is that PCL in the airways is independently predicted at every boundary nodes, in which the fluxes to adjacent cells are not available. For future study,

PCL could be solved as an integral layer inside the airways involving fluxes from/to epithelial cell, mucus layer and adjacent areas. This will be especially useful to evaluate the potential bifurcation dehydration, as whether the relatively high PCL depth in the outer surface of a bifurcation can balance the relatively low PCL depth in the inner surface of a bifurcation. Also other sources such as gland secretion, hormone regulation, and cilia beating could also affect the regional PCL depth, with which it might lead to a more complex but realistic model.

Table 5.1 Lobar ventilation distributions for 6 subjects.

Sub.	LUL	LLL	RUL	RML	RLL
	CF				
CF01	0.227	0.269	0.173	0.047	0.285
CF02	0.237	0.318	0.196	0.046	0.203
CF03	0.195	0.265	0.169	0.060	0.311
Avg.	0.220	0.284	0.179	0.051	0.266
	NL				
NL01	0.185	0.288	0.151	0.078	0.297
NL02	0.200	0.292	0.163	0.056	0.290
NL03	0.193	0.290	0.150	0.069	0.299
Avg	0.192	0.290	0.155	0.068	0.295
P value	0.160	0.749	0.034	0.158	0.432

*LUL, left upper lobe; LLL, left lower lobes; RUL, right upper lobe; RML, right middle lobe; RLL, right lower lobe.

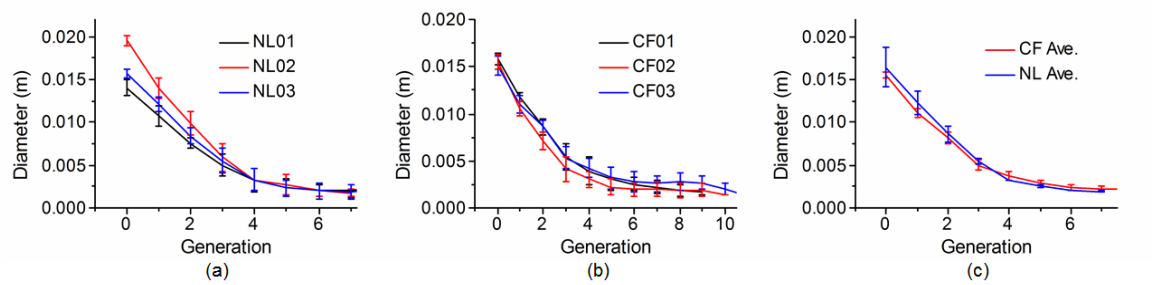

Figure 5.1 The average diameters and standard deviations for (a) 3 NL subjects and (b) 3 CF subjects in each generation. (c) The average diameters for NL and CF subjects in each generation.

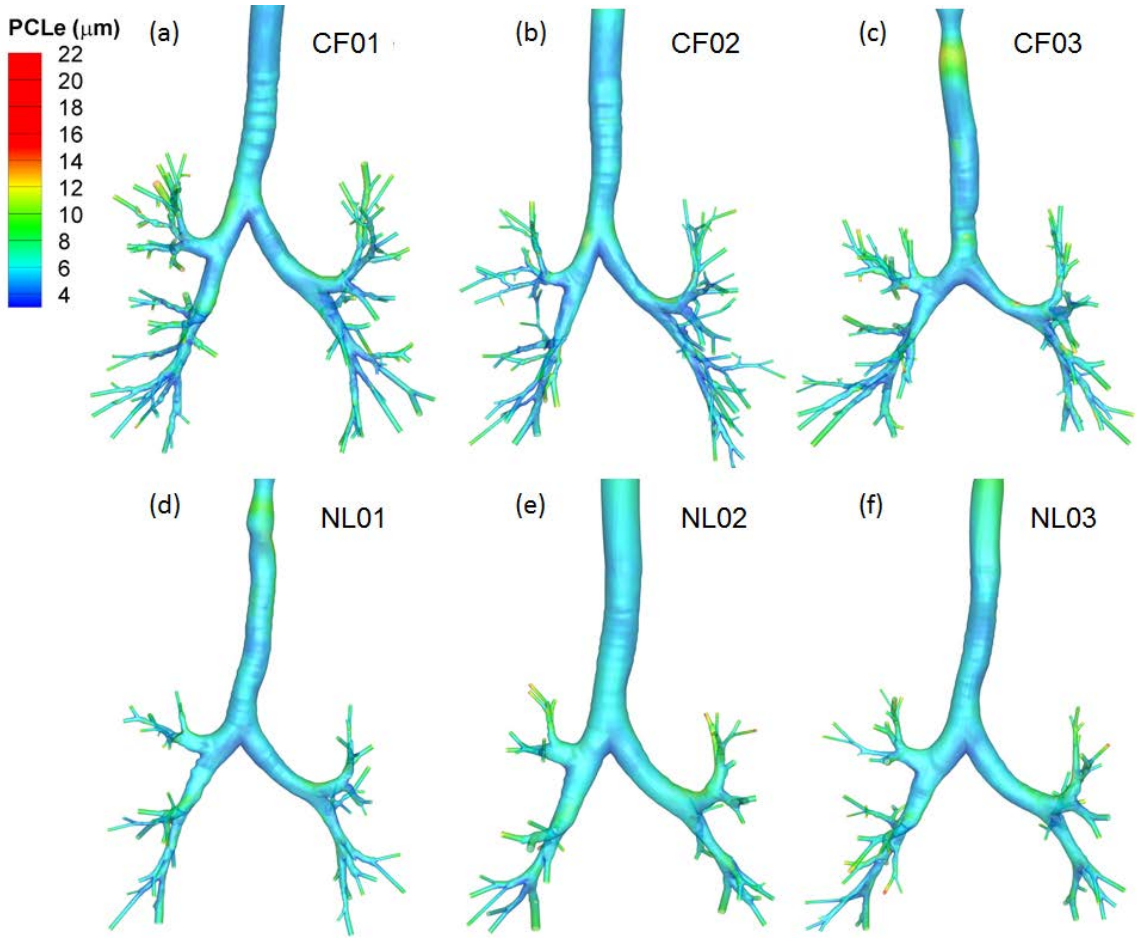

Figure 5.2 The PCLe depth distributions for 3 NL and 3 CF subjects.

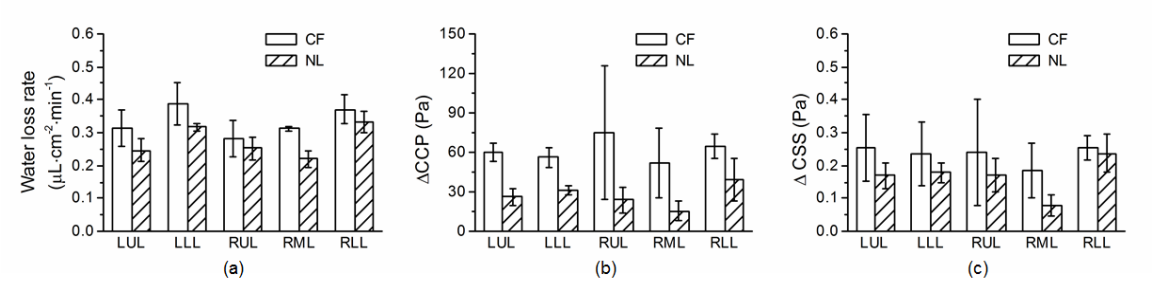

Figure 5.3 The NL vs. CF: (a) water loss rate, (b) CCP change and (c) CSS change in each lobe.

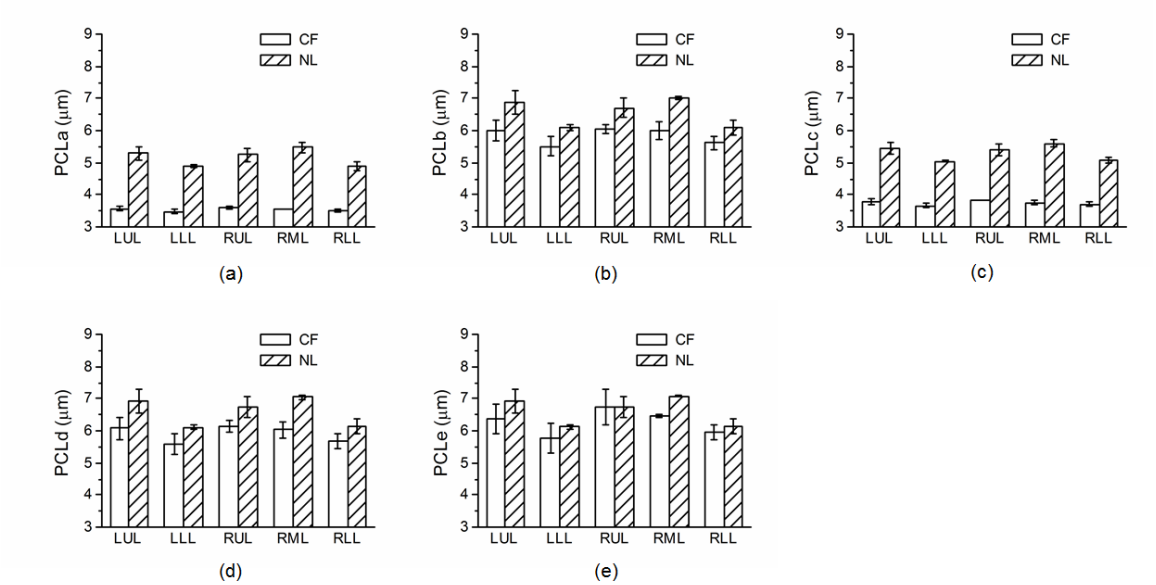

Figure 5.4 The NL vs CF: average (a) PCLa, (b) PCLb, (c) PCLc, (d) PCLd, and (e) PCLe depths in each lobe.

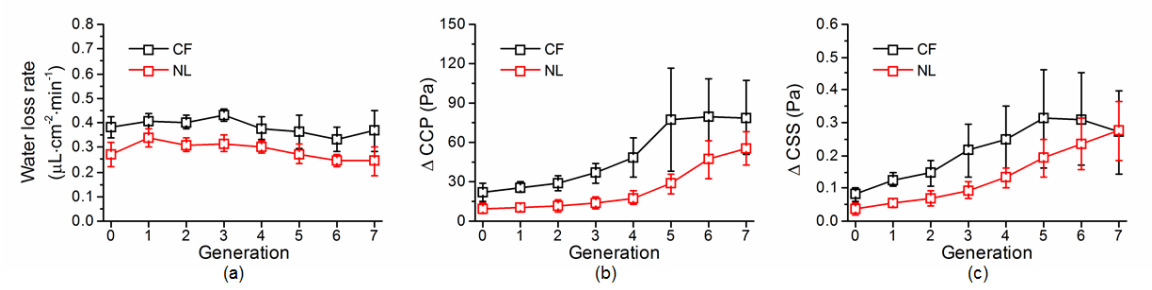

Figure 5.5 The NL vs. CF: (a) water loss rate, (b) CCP change and (c) CSS change in each generation.

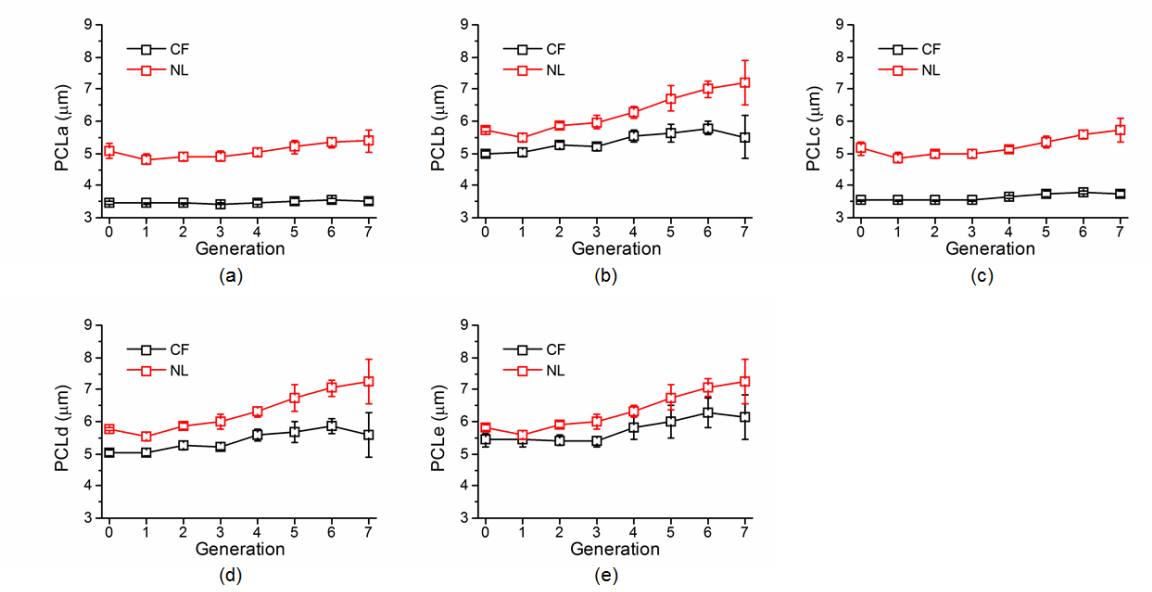

Figure 5.6 The NL vs CF: average (a) PCLa, (b) PCLb, (c) PCLc, (d) PCLd, and (e) PCLe depths in each generation.

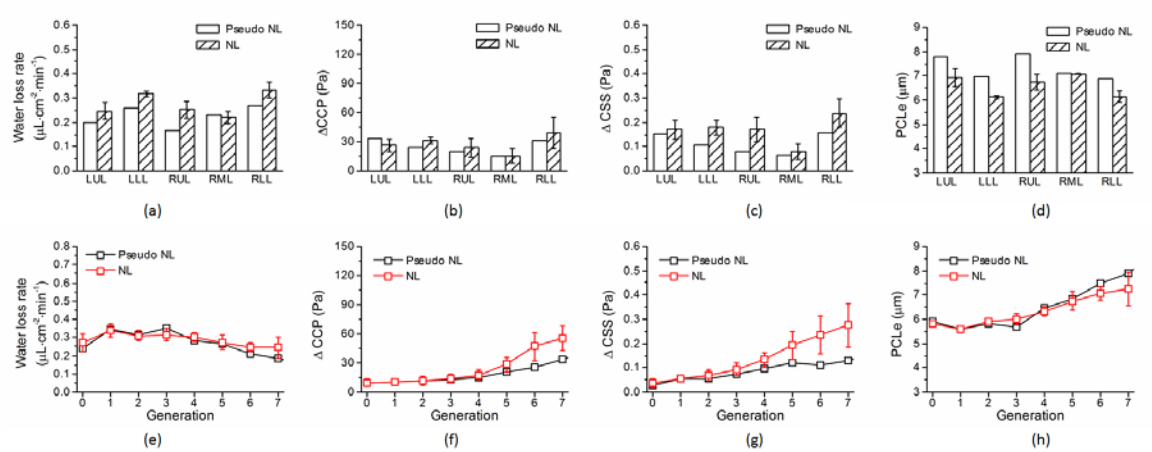

Figure 5.7 The pseudo NL vs NL: (a) and (e) water loss rate, (b) and (f) CCP change, (c) and (g) CSS change, (d) and (h) PCLe distributions in each lobe and in each generation, respectively.

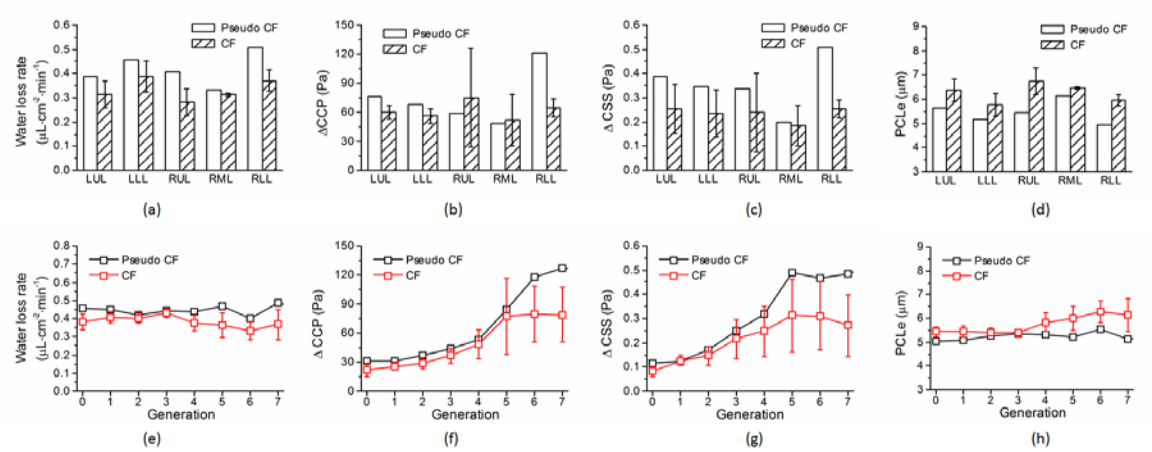

Figure 5.8 The Pseudo CF vs CF in (a) and (e) water loss rate, (b) and (f) CCP change, (c) and (g) CSS change, (d) and (h) PCLe distributions in each lobe and in each generation respectively.

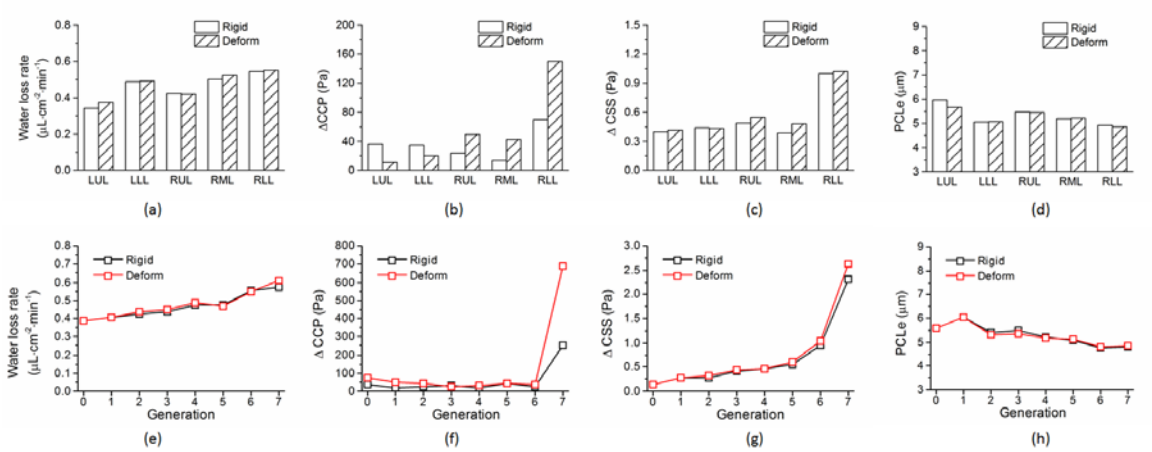

Figure 5.9 The rigid vs deform case at 15 L/min in (a) and (e) water loss rate, (b) and (f) CCP change, (c) and (g) CSS change, (d) and (h) PCLe distributions in each lobe and in each generation respectively.

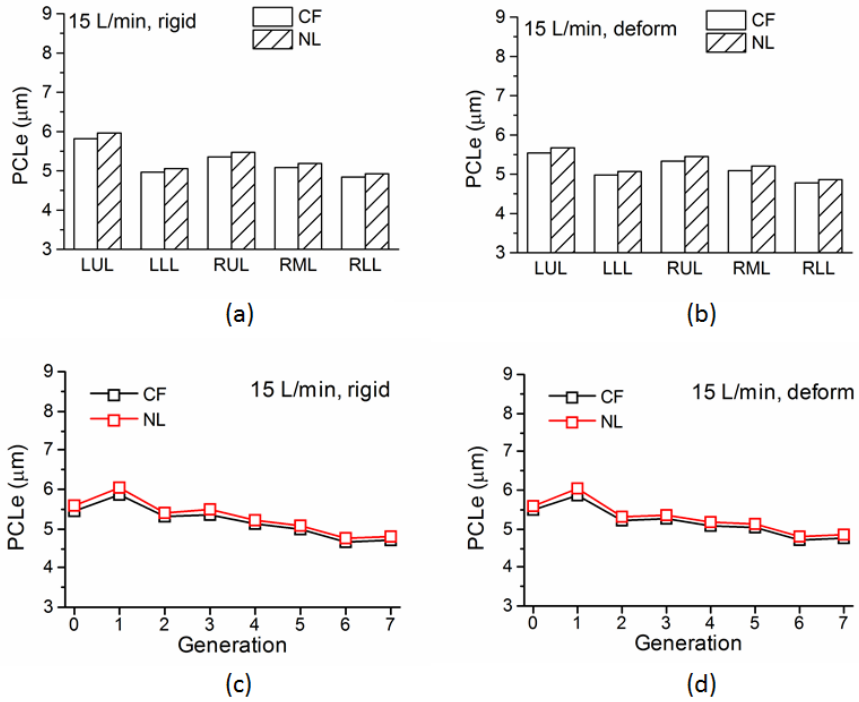

Figure 5.10 PCLe depth predicted with NL vs CF cells in (a) and (c) 15 L/min rigid case and (b) and (d) 15 L/min deform case in each lobe and each generation respectively.

CHAPTER 6

SUMMARY AND FUTURE WORK

6.1 Summary

In Chapter 2, we developed a thermo-fluid CFD model to predict the distributions of temperature and humidity in a 3D subject-specific human airway with a realistic airway wall boundary condition. In Chapter 3, we investigated the water loss in 3D subject-specific human airway models and found that the water loss rate is elevated due to secondary flows at bifurcations which only exist in 3D. In Chapter 4, we developed an ion-channel conductance model that connects the existing ATP model and the fluid secretion model. The epithelial cell model successfully predicted PCL depth under various conditions measured in experiments. In Chapter 5, the cell model is coupled with the thermo-fluid CFD model to study PCL depth regulation in response to mechanical forces and evaporative water loss in normal and CF human airways. In summary, we found that the evaporative water loss is the dominant factor affecting the PCL depth, while ATP release triggered by cyclic shear stress is the primary mechanism to restore evaporative water loss. Comparing with normal subjects, mechanical forces play a greater role in regulating the PCL depth in CF subjects. The greater diameters in CF subjects from 4^{th} to 7^{th} generation might help CF subjects decreasing water loss rate and maintaining PCL depth similar to NL PCL level in these generations. Generally under regular breathing conditions, PCL depths in both normal and CF subjects are at 6 to 7 μm range, which is slightly lower than optimum PCL depth of 7.68 μm. This suggests that besides fluid secretion regulated by mechanical forces, other mechanisms that have not been accounted for in our integrated model might be involved in PCL depth rehydration.

6.2 Future work

As the limitations mentioned at the end of each previous chapter, several future works could be done to improve PCL depth prediction:

1. More experimental data could be obtained to calibrate the ion-channel conductance model. Especially, inside the airways, the change of cyclic shear stress is usually from 0.0 to 6.0 dyne/cm^2, which the ATP release could be from [0, 130] nM (Tarran et al. 2005). However, the change of PCL depth corresponding to the ATP release within [63.7, 130] nM is unclear. So currently under regular breathing conditions, PCL depth reaches maximum when ATP release is greater than 63.7 nM for both CF and normal cells, which corresponds to the shear stress of around 0.5 dyne/cm^2. This shear stress could be easily achieved as shown from the CFD results in Chapter 5. This could be the reason that normal and CF airways, as well as rigid and deformable airways, exhibit a wide range of mechanical forces, yet the predicted PCL depths do not vary as much.
2. PCL could be solved as a single layer lining the entire airway. We have found that the highest PCL depth is at the outer surfaces of bifurcations due to little evaporative water loss. The lowest PCL depth is located at the inner surfaces of bifurcations due to elevated evaporative water loss. Modeling a PCL layer could answer the question whether excessive PCL could recover excessive water loss within adjacent areas.
3. The force-buffering effects from the ASL layer could be added between the integration of the thermo-fluid CFD model and the epithelial cell model. As the shear stress and compressive pressure acting at the interface of ASL and lumen might be greater than the forces acting on the epithelial cells, namely, the mucus layer and PCL layers could act as buffering layers. The spring models of mucus layer and PCL layer from Button et al. (2012) could be considered as the buffering model for pressure forces. However, the buffering model for shear stress is yet to be proposed.

REFERENCES

Bell, S. C., M. J. Saunders, J. S. Elborn, and D. J. Shale. 1996. “Resting Energy Expenditure and Oxygen Cost of Breathing in Patients with Cystic Fibrosis.” *Thorax* 51 (2): 126–31.

Boucher, R. C. 2002. “An Overview of the Pathogenesis of Cystic Fibrosis Lung Disease.” *Advanced Drug Delivery Reviews*, Current concepts on the Pathophysiology and Drug Development in Cystic Fibrosis, 54 (11): 1359–71. doi:10.1016/S0169-409X(02)00144-8.

Boucher, Richard C. 2007. “Airway Surface Dehydration in Cystic Fibrosis: Pathogenesis and Therapy.” *Annual Review of Medicine* 58: 157–70. doi:10.1146/annurev.med.58.071905.105316.

Browning, I. B., G. E. D’Alonzo, and M. J. Tobin. 1990. “Importance of Respiratory Rate as an Indicator of Respiratory Dysfunction in Patients with Cystic Fibrosis.” *Chest* 97 (6): 1317–21.

Burki, N K. 1984. “Ventilatory Effects of Doxapram in Conscious Human Subjects.” *Chest* 85 (5): 600–604. doi:10.1378/chest.85.5.600.

Button, Brian, Li-Heng Cai, Camille Ehre, Mehmet Kesimer, David B. Hill, John K. Sheehan, Richard C. Boucher, and Michael Rubinstein. 2012. “A Periciliary Brush Promotes the Lung Health by Separating the Mucus Layer from Airway Epithelia.” *Science* 337 (6097): 937–41. doi:10.1126/science.1223012.

Button, Brian, Seiko F. Okada, Charles Brandon Frederick, William R. Thelin, and Richard C. Boucher. 2013. “Mechanosensitive ATP Release Maintains Proper Mucus Hydration of Airways.” *Science Signaling* 6 (279): ra46. doi:10.1126/scisignal.2003755.

Button, Brian, Maryse Picher, and Richard C Boucher. 2007. “Differential Effects of Cyclic and Constant Stress on ATP Release and Mucociliary Transport by Human Airway Epithelia.” *The Journal of Physiology* 580 (Pt. 2): 577–92. doi:10.1113/jphysiol.2006.126086.

Castro, Mario, Sean B. Fain, Eric A. Hoffman, David S. Gierada, Serpil C. Erzurum, and Sally Wenzel. 2011. “Lung Imaging in Asthmatic Patients: The Picture Is Clearer.” *Journal of Allergy and Clinical Immunology* 128 (3): 467–78. doi:10.1016/j.jaci.2011.04.051.

Choi, Sanghun, Eric A Hoffman, Sally E Wenzel, Merryn H Tawhai, Youbing Yin, Mario Castro, and Ching-Long Lin. 2013. “Registration-Based Assessment of Regional Lung Function via Volumetric CT Images of Normal Subjects vs. Severe Asthmatics.” *Journal of Applied Physiology* 115 (5): 730–42. doi:10.1152/japplphysiol.00113.2013.

Daviskas, E, I Gonda, and S D Anderson. 1990. “Mathematical Modeling of Heat and Water Transport in Human Respiratory Tract.” *Journal of Applied Physiology (Bethesda, Md.: 1985)* 69 (1): 362–72.

Daviskas, E, I Gonda, and S D Anderson. 1990. 1991. “Local Airway Heat and Water Vapour Losses.” *Respiration Physiology* 84 (1): 115–32.

Feng, Y., C. Kleinstreuer, and A. Rostami. 2015. “Evaporation and Condensation of Multicomponent Electronic Cigarette Droplets and Conventional Cigarette Smoke Particles in an Idealized G3–G6 Triple Bifurcating Unit.” *Journal of Aerosol Science* 80 (February): 58–74. doi:10.1016/j.jaerosci.2014.11.002.

Ferron, G.A., B. Haider, and W.G. Kreyling. 1988. “Inhalation of Salt Aerosol Particles—i. Estimation of the Temperature and Relative Humidity of the Air in the Human Upper Airways.” *Journal of Aerosol Science* 19 (3): 343–63. doi:10.1016/0021-8502(88)90274-1.

Finlay, Warren H. 2001. *The Mechanics of Inhaled Pharmaceutical Aerosols: An Introduction*. Academic Press.

Finlay, W. H., and K. W. Stapleton. 1995. “The Effect on Regional Lung Deposition of Coupled Heat and Mass Transfer between Hygroscopic Droplets and Their Surrounding Phase.” *Journal of Aerosol Science* 26 (4): 655–70. doi:10.1016/0021-8502(94)00132-I.

Freund, Beau J., and Andrew J. Young. 1995. *Environmental Influence on Body Fluid Balance during Exercise: Cold Exposure*. Technical. US Army Research Institute of Environmental Medicine Natick, Massachusetts.

Hamilton, Gavin. 1998. “Investigations of the Thermal Properties of Human and Animal Tissues.” PhD, University of Glasgow.

Hanna, L. M., and P. W. Scherer. 1986. “Regional Control of Local Airway Heat and Water Vapor Losses.” *Journal of Applied Physiology* 61 (2): 624–32.

Hasan, Ashfaq. 2010. *Understanding Mechanical Ventilation: A Practical Handbook*. Springer.

Herschlag, Gregory, Guilherme J. M. Garcia, Brian Button, Robert Tarran, Brandon Lindley, Benjamin Reinhardt, Timothy C. Elston, and M. Gregory Forest. 2013. “A Mechanochemical Model for Auto-Regulation of Lung Airway Surface Layer Volume.” *Journal of Theoretical Biology* 325 (May): 42–51. doi:10.1016/j.jtbi.2013.01.023.

Ingenito, E P, J Solway, E R McFadden Jr, B M Pichurko, E G Cravalho, and J M Drazen. 1986. “Finite Difference Analysis of Respiratory Heat Transfer.” *Journal of Applied Physiology (Bethesda, Md.: 1985)* 61 (6): 2252–59.

Jahani, Nariman, Youbing Yin, Eric A. Hoffman, and Ching-Long Lin. 2014. “Assessment of Regional Non-Linear Tissue Deformation and Air Volume Change of Human Lungs via Image Registration.” *Journal of Biomechanics*. Accessed March 29. doi:10.1016/j.jbiomech.2014.02.040.

Javaheri, Emadeddin, Farzin M. Shemirani, Marine Pichelin, Ira M. Katz, Georges Caillibotte, Reinhard Vehring, and Warren H. Finlay. 2013. “Deposition Modeling of Hygroscopic Saline Aerosols in the Human Respiratory Tract: Comparison between Air and Helium–oxygen as Carrier Gases.” *Journal of Aerosol Science* 64 (October): 81–93. doi:10.1016/j.jaerosci.2013.04.010.

Kays, W. M, and M. E Crawford. 1993. *Convective Heat and Mass Transfer*. New York: McGraw-Hill.

Kim, Jong Won, Jinxiang Xi, and Xiuhua A. Si. 2013. "Dynamic Growth and Deposition of Hygroscopic Aerosols in the Nasal Airway of a 5-Year-Old Child." *International Journal for Numerical Methods in Biomedical Engineering* 29 (1): 17–39. doi:10.1002/cnm.2490.

Knowles, Michael R., and Richard C. Boucher. 2002. "Mucus Clearance as a Primary Innate Defense Mechanism for Mammalian Airways." *Journal of Clinical Investigation* 109 (5): 571–77. doi:10.1172/JCI15217.

Lin, Ching-Long, Haegyun Lee, Taehun Lee, and Larry J. Weber. 2005. "A Level Set Characteristic Galerkin Finite Element Method for Free Surface Flows." *International Journal for Numerical Methods in Fluids* 49 (5): 521–47. doi:10.1002/fld.1006.

Lin, Ching-Long, Merryn H Tawhai, and Eric A Hoffman. 2013. "Multiscale Image-Based Modeling and Simulation of Gas Flow and Particle Transport in the Human Lungs." *Wiley Interdisciplinary Reviews. Systems Biology and Medicine* 5 (5): 643–55. doi:10.1002/wsbm.1234.

Lin, Ching-Long, Merryn H Tawhai, Geoffrey McLennan, and Eric A Hoffman. 2007. "Characteristics of the Turbulent Laryngeal Jet and Its Effect on Airflow in the Human Intra-Thoracic Airways." *Respiratory Physiology & Neurobiology* 157 (2-3): 295–309. doi:10.1016/j.resp.2007.02.006.

Lin, Ching-long, M.H. Tawhai, G. McLennan, and E.A. Hoffman. 2009. "Computational Fluid Dynamics." *IEEE Engineering in Medicine and Biology Magazine* 28 (3): 25–33. doi:10.1109/MEMB.2009.932480.

MacIntyre, Neil. 2011. *Respiratory Care: Principles and Practice*. Jones & Bartlett Learning.

Martonen, Ted B., Jacky A. Rosati, and Kristin K. Isaacs. 2013. "Modeling Deposition of Inhaled Particles." In *Aerosols Handbook: Measurement, Dosimetry, and Health Effects*, edited by Lev S. Ruzer and Naomi H. Harley, 113–55. CRC Press.

McFadden, E. R., B. M. Pichurko, H. F. Bowman, E. Ingenito, S. Burns, N. Dowling, and J. Solway. 1985. "Thermal Mapping of the Airways in Humans." *Journal of Applied Physiology* 58 (2): 564–70.

Morvay, Zoran, and Dušan Gvozdenac. 2008. *Applied Industrial Energy and Environmental Management*. John Wiley & Sons.

Nagel, G., P. Barbry, H. Chabot, E. Brochiero, K. Hartung, and R. Grygorczyk. 2005. "CFTR Fails to Inhibit the Epithelial Sodium Channel ENaC Expressed in Xenopus Laevis Oocytes." *The Journal of Physiology* 564 (Pt 3): 671–82. doi:10.1113/jphysiol.2004.079046.

Nellis, Gregory, and Sanford Klein. 2009. *Heat Transfer*. Cambridge University Press.

Okada, Seiko F., Robert A. Nicholas, Silvia M. Kreda, Eduardo R. Lazarowski, and Richard C. Boucher. 2006. “Physiological Regulation of ATP Release at the Apical Surface of Human Airway Epithelia.” *The Journal of Biological Chemistry* 281 (32): 22992–2. doi:10.1074/jbc.M603019200.

Primiano, F. P., G. M. Saidel, F. W. Montague, K. L. Kruse, C. G. Green, and J. G. Horowitz. 1988. “Water Vapour and Temperature Dynamics in the Upper Airways of Normal and CF Subjects.” *European Respiratory Journal* 1 (5): 407–14.

Shinjiro Miyawaki, Merryn H. Tawhai, Eric A. Hoffman, and Ching-Long Lin. 2014. “A Numerical Study Of Correlation Between Aerosol Deposition And Airway Skeleton Of Severe Asthmatics.” In *D52. GAS EXCHANGE IN STEADY STATE, ALTITUDE, AND EXERCISE*, A6281–A6281. American Thoracic Society International Conference Abstracts. American Thoracic Society.

Tabka, Zouhair, Abdellaziz Ben Jebria, and Hervé Guénard. 1987. “Effect of Breathing Dry Warm Air on Respiratory Water Loss at Rest and during Exercise.” *Respiration Physiology* 67 (2): 115–25.

Tarran, Robert, Brian Button, Maryse Picher, Anthony M Paradiso, Carla M Ribeiro, Eduardo R Lazarowski, Liqun Zhang, et al. 2005. “Normal and Cystic Fibrosis Airway Surface Liquid Homeostasis. The Effects of Phasic Shear Stress and Viral Infections.” *The Journal of Biological Chemistry* 280 (42): 35751–59. doi:10.1074/jbc.M505832200.

Tarran, Robert, Laura Trout, Scott H. Donaldson, and Richard C. Boucher. 2006. “Soluble Mediators, Not Cilia, Determine Airway Surface Liquid Volume in Normal and Cystic Fibrosis Superficial Airway Epithelia.” *The Journal of General Physiology* 127 (5): 591–604. doi:10.1085/jgp.200509468.

Tawhai, Merryn H., and Peter J. Hunter. 2004. “Modeling Water Vapor and Heat Transfer in the Normal and the Intubated Airways.” *Annals of Biomedical Engineering* 32 (4): 609–22.

Tawhai, Merryn H., Peter Hunter, Juerg Tschirren, Joseph Reinhardt, Geoffrey McLennan, and Eric A. Hoffman. 2004. “CT-Based Geometry Analysis and Finite Element Models of the Human and Ovine Bronchial Tree.” *Journal of Applied Physiology* 97 (6): 2310–21.

Tsu, Maria E., Albert L. Babb, David D. Ralph, and Michael P. Hlastala. 1988. “Dynamics of Heat, Water, and Soluble Gas Exchange in the Human Airways: 1. A Model Study.” *Annals of Biomedical Engineering* 16 (6): 547–71.

Venegas, Jose G., Tilo Winkler, Guido Musch, Marcos F. Vidal Melo, Dominick Layfield, Nora Tgavalekos, Alan J. Fischman, Ronald J. Callahan, Giacomo Bellani, and R. Scott Harris. 2005. “Self-Organized Patchiness in Asthma as a Prelude to Catastrophic Shifts.” *Nature* 434 (7034): 777–82. doi:10.1038/nature03490.

Vreman, A. W. 2004. “An Eddy-Viscosity Subgrid-Scale Model for Turbulent Shear Flow: Algebraic Theory and Applications.” *Physics of Fluids* 16: 3670.

Warren, N. J., E. J. Crampin, and M. H. Tawhai. 2010. “The Role of Airway Epithelium in Replenishment of Evaporated Airway Surface Liquid from the Human Conducting Airways.” *Annals of Biomedical Engineering* 38 (12): 3535–49.

Weibel, Ewald R. 1963. *Morphometry of the Human Lung*. Academic Press.

Weiler, John M., Sandra D. Anderson, Christopher Randolph, Sergio Bonini, Timothy J. Craig, David S. Pearlman, Kenneth W. Rundell, et al. 2010. "Pathogenesis, Prevalence, Diagnosis, and Management of Exercise-Induced Bronchoconstriction: A Practice Parameter." *Annals of Allergy, Asthma & Immunology* 105 (6): S1–47. doi:10.1016/j.anai.2010.09.021.

Widdicombe, JH. 2002. "Regulation of the Depth and Composition of Airway Surface Liquid." *Journal of Anatomy* 201 (4): 313–18. doi:10.1046/j.1469-7580.2002.00098.x.

Wu, Dan, Shinjiro Miyawaki, Merryn H. Tawhai, Eric A. Hoffman, David A. Stoltz, and Ching-Long Lin. 2015. "A Numerical Study of Water Loss Rate Distribution in MDCT-Based Human Airway Models." *Accpeted to Annals of Biomedical Engineering*.

Wu, Dan, Merryn H. Tawhai, Eric A. Hoffman, and Ching-Long Lin. 2014. "A Numerical Study of Heat and Water Vapor Transfer in MDCT-Based Human Airway Models." *Annals of Biomedical Engineering* 42 (10): 2117–31. doi:10.1007/s10439-014-1074-9.

Yin, Youbing, Jiwoong Choi, Eric A. Hoffman, Merryn H. Tawhai, and Ching-Long Lin. 2010. "Simulation of Pulmonary Air Flow with a Subject-Specific Boundary Condition." *Journal of Biomechanics* 43 (11): 2159–63.

Yin, Youbing, Jiwoong Choi, Eric A. Hoffman, Merryn H. Tawhai, and Ching-Long Lin. 2013. "A Multiscale MDCT Image-Based Breathing Lung Model with Time-Varying Regional Ventilation." *Journal of Computational Physics*, Multi-scale Modeling and Simulation of Biological Systems, 244 (July): 168–92. doi:10.1016/j.jcp.2012.12.007.

Zhang, Z., and C. Kleinstreuer. 2003. "Species Heat and Mass Transfer in a Human Upper Airway Model." *International Journal of Heat and Mass Transfer* 46 (25): 4755–68.

Zuo, Peiying. 2007. "Modeling the Airway Surface Liquid Regulation in Human Lungs." PhD, University of North Carolina at Chapel Hill.

Zuo, Peiying, Maryse Picher, Seiko F. Okada, Eduardo R. Lazarowski, Brian Button, Richard C. Boucher, and Timothy C. Elston. 2008. "Mathematical Model of Nucleotide Regulation on Airway Epithelia. Implications for Airway Homeostasis." *The Journal of Biological Chemistry* 283 (39): 26805–19. doi:10.1074/jbc.M801516200.